INFORMATION TO USERS

This manuscript has been reproduced from the microfilm master. UMI films the text directly from the original or copy submitted. Thus, some thesis and dissertation copies are in typewriter face, while others may be from any type of computer printer.

The quality of this reproduction is dependent upon the quality of the copy submitted. Broken or indistinct print, colored or poor quality illustrations and photographs, print bleedthrough, substandard margins, and improper alignment can adversely affect reproduction.

In the unlikely event that the author did not send UMI a complete manuscript and there are missing pages, these will be noted. Also, if unauthorized copyright material had to be removed, a note will indicate the deletion.

Oversize materials (e.g., maps, drawings, charts) are reproduced by sectioning the original, beginning at the upper left-hand corner and continuing from left to right in equal sections with small overlaps. Each original is also photographed in one exposure and is included in reduced form at the back of the book.

Photographs included in the original manuscript have been reproduced xerographically in this copy. Higher quality 6" x 9" black and white photographic prints are available for any photographs or illustrations appearing in this copy for an additional charge. Contact UMI directly to order.

UMI

University of Alberta

Study of Mixing Phenomena in a Dual Fuel Diesel Engine Air Intake Manifold

by

Oleg Zastavniouk ©

A thesis submitted to the Faculty of Graduate Studies and Research in partial fulfillment

of the requirements for the degree of Master of Science

Department of Mechanical Engineering

Edmonton, Alberta

Fall 1997

Canada

University of Alberta

Library Release Form

Name of Author: Oleg Zastavniouk
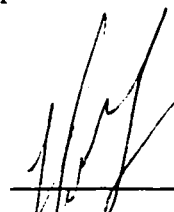
Title of Thesis: Study of Mixing Phenomena in a Dual Fuel Diesel Engine Air Intake Manifold

Degree: Master of Science

Year this Degree Granted: 1997

Permission is hereby granted to the University of Alberta Library to reproduce single copies of this thesis and to lend or sell such copies for private, scholarly, or scientific research purposes only.

The author reserves all other publication and other rights in association with the copyright in the thesis, and except as hereinbefore provided, neither the thesis nor any substantial portion thereof may be printed or otherwise reproduced in any material form whatever without the author's prior written permission.

/Zastavniuk/

802 Erin Place
Edmonton, Alberta, Canada
T5T 1M6

July 29, 1997

University of Alberta

Faculty of Graduate Studies and Research
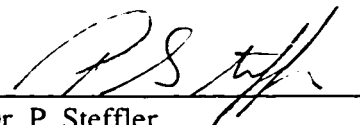
The undersigned certify that they have read, and recommended to the Faculty of Graduate Studies and Research for acceptance, a thesis entitled Study of Mixing Phenomena in a Dual Fuel Diesel Engine Air Intake Manifold submitted by Oleg Zastavniouk in partial fulfillment of the requirements for the degree of Master Science.

Dr. M.D. Checkel   24 July /97

Dr. D.J. Wilson

Dr. P. Steffler

"Its strange but true; for truth is always strange; - stranger than fiction," Byron

"To know that we know what we know, and that we do not know what we do not know, that is true knowledge," (quoting Confucius)

"Nature, to be commanded, must be obeyed," Francis Bacon

Abstract

Natural gas has emerged as an alternative to gasoline and diesel as the primary transportation fuels. Existing diesel engines can fairly readily be converted to dual-fuel operation, ideally giving a substantial emission reduction. Metering the natural gas fuel and mixing it with the combustion air are two of the critical functions in achieving a successful dual-fuel engine with low emissions.

By placing a fuel injector at each cylinder air-intake port, it is possible to accurately control the flow of fuel to each cylinder but it does have the disadvantage that the fuel and air do not have as much time to mix and form a homogeneous charge. High emissions of unburnt natural gas under some operating conditions show that mixing can be problematic.

An extensive literature survey show that very little has been published describing transient sonic jets mixing into confined, turbulent cross flows. A laboratory model, incorporating circular duct section and injection system hardware, has been developed to investigate mixing phenomena of turbulent gaseous jets in an enclosed environment similar to an engine air-intake manifold. The concentration field in compressible subsonic jets of natural gas and air has been studied using a Fast Flame Ionization Detector (FFID) technique.

Acknowledgments

Table of Contents

List of Tables

List of Figures

List of Symbols, Nomenclature, and Abbreviation

ϕ	volume equivalence ratio of freestream to jet fluid
ρ_{mix}	density of gas-air mixture, (kg / m^3)
ρ_{gas}	density of gas in mixture, (kg / m^3)
ρ_j	density of the jet fluid (kg / m^3)
ρ_∞	density of the freestream fluid (kg / m^3)
A	area of test duct cross-section, (m^2)
A_p	the assigned area for measuring point, (m^2)
A_{tube}	area of the injector nozzle, (m^2)
$\overline{C}$	the time average value of local concentration, (%)
C_0	minimum value of measured concentration, (%)
C_i	measured point data (instantaneous value) concentration, (%)
C_f	maximum value of measured concentration, (%)
CNG	compressed natural gas
CO	carbon monoxide
d	jet orifice diameter, m
D	diameter of the test duct, m
DAS	data acquisition system
F	function of the injection pressure, $2.42d\left(\dfrac{U_j}{d}\right)^{0.5}$
FFID	Fast Flame Ionization Detector
HC	hydrocarbons - organic compound
HSV	Servojet High Speed Solenoid Valve
JICF	Jets in Cross-flow
k	constant in time-constant fit equations
l	global characteristics jet length, (m)
L	penetration length of the jet tip, (mm)

$\dot{m}_{air}$	mass flow rate of freestream, (kg/s)
$\dot{m}_{gas}$	mass flow rate of injected gas, (kg/s)
$\dot{m}_j$	mass flow of jet fluid, $\rho_j U_j d^2 \dfrac{\pi}{4}$, (kg/s)
$\dot{m}_{gs}$	total gas mass flux in a given duct cross section, (kg/s)
$\dot{m}_{gp}$	total gas mass flux per injection in a given duct cross section, (kg/inj)
mf_{gs}	gas mass flux in a given measurement point, (kg/s)
mf_{gp}	gas mass flux per one gas injection in a given measurement point, (kg/ing)
M	Mach number
MW	molar weight
n	the total number of points taken during the time interval
ΔP	differential pressure in Pitot tube measurements, (kPa)
P_{bar}	barometric pressure in experiments, (kPa)
r^2	square of vortex spacing
R	ratio of the jet to cross-flow velocity, U_j / U_∞
Re	Reynolds number
Re_l	far-field Reynolds number
Sc	Schmidt number
Δt	the time step, (0.5 ms)
t_{pulse}	pulse width of injection, (ms)
T	time interval for $T_{90\%} - T_{10\%}$, (ms)
Tc	time constant parameter, (ms)
Ti	the time period of injection, (ms)
$\overline{U}$	the mean value of flow velocity at measuring point, (m/s)
U_j	jet velocity, averaged across nozzle exit, (m/s)
U_∞	freestream time-averaged velocity, (m/s)
w_y	jet width for the plane view, (mm)
w_z	jet width for the side view, (mm)

x	downstream distance, (mm)
x_p	penetration depth of wall jet, (mm)
x_s	penetration distance of upstream ground vortex, (mm)
x/d < 20	near-field zone
x/d > 20	far-field zone
X	mole fraction of jet gas in the mixture
y	far-downstream penetration, (mm)
y_p	maximum radial extent of wall jet, (mm)

1. Introduction

This thesis is an exploratory study of techniques to quantitatively analyze the mixture formation of air and natural gas in the air intake manifold of dual-fuel diesel engines. The focus of the present research was to measure the variation in the mixture composition at the time the gas-air stream enters the engine air-intake valve. A literature survey by the author found no published results on pulsed, variable density gas injection into cross-flows in a confined volume. Mixing processes have been studied by many techniques including Laser Raman Spectroscopy, Schlieren photography and various direct sampling methods [1, 2, 3]. Most of these techniques require a special research laboratory environment and could not be applied to real diesel engine conditions. However, fast-response hydrocarbon probes have been developed with the capability to sample mixtures in engine manifold conditions. This study employs such a fast-response hydrocarbon probe to measure mixture formation for steady and pulsed gas jets in a laboratory intake manifold model with steady air flow.

1.1. Natural Gas as an Alternative Fuel

The major reason for this study of gaseous jet mixing is the use of compressed natural gas (CNG) as an alternative vehicular fuel in dual-fuel engines. Increasingly strict emission standards applied to automotive diesel engines have prompted an interest in alternative fuels such as natural gas. Dual-fuel engines have well-established advantages over diesel fuel engines, which include lower carbon monoxide (CO) emissions, lower reactive (non-methane) hydrocarbon (HC) emissions, reduced emissions of oxides of nitrogen (NOx), and practically zero particulate emissions [4]. Natural gas composition varies but it is generally composed of 85 - 99% methane with the remainder made up of other hydrocarbons and inert gases. Average CNG properties compared with diesel fuel are reported in Table 1-1.

1

Table 1-1. Comparison of physical properties of natural gas and diesel fuel.

PROPERTIES	NATURAL GAS	DIESEL FUEL
Phase at ambient temperature and pressure	gas	liquid
Average composition (Northwestern Utilities)	92% CH_4, 3% C_2H_6, 4% N_2, 0.8% CO_2, 0.2% inert gases	long chain hydrocarbons $C_nH_{1.8n}$
Sulfur content (% mass)	N/A	0.24
Molecular weight	about 17.1	226
Specific gravity (@ 15°C, 1 bar)	0.00079	0.845
Stoichiometric air-fuel ratio (A/F on mass basis)	15.7	14.5 - 16.0
Vapor flammability limits (@ STP conditions)	5.3% - 15%	0.6% - 6.5%
Autoignition temperature (@ 1 bar)	650°C	204 - 260°C
Stoichiometric flame temperature (@ STP conditions)	1875°C	2054°C
Lower heating value: mass basis (MJ/kg) volume basis (MJ/l)	45.3 6.8[1]	43.2 36.5
Price[2] (cents/liter equiv.)	28.5	32.7

[1] in storage conditions @ 15°C, 220 bar.

[2] on energy equivalent comparison (Edmonton Transit Prices from August 1993).

1.2. Dual Fuel Engine Technology

Existing diesel engines can fairly readily be converted to dual-fuel operation, making possible the substitution of low-cost natural gas for higher-cost diesel fuels, as well as substantial, cost-effective reduction in pollutant emissions.

In the dual-fuel system, a charge of mixture of gaseous fuel and air is compressed rapidly to high temperatures and pressures, then ignited by the injection of a small quantity of diesel fuel just before the end of compression stroke. The major advantage of

this system is the ability to burn very lean air-fuel mixtures with high efficiency. This is due to the reliable, high energy ignition source provided by the pilot fuel, and to the rapid combustion of the natural gas/air charge. The use of extremely lean mixture and the rapid combustion allow dual-fuel engines to use high diesel compression ratios without destructive knock. Nonetheless, knock poses an important limit on dual-fuel engine power output, and care must be taken to avoid excessively rich gas/air mixtures.

Liquid fuel injection is a well-developed technology, whereas high pressure, (e.g., 0.3 MPa), subsonic, transient gas fuel injection is not. In addition, the conversion of liquid-fueled diesel engines to natural gas diesel operation results in a number of unique design problems. For example, there are differences between liquid and gaseous fuel-air mixing; differences in autoignition delay times; and differences in flame propagation. A thorough understanding of gas-air mixture formation is very important for designing the natural gas injection system.

1.3. Methods of Injection of Natural Gas

Metering the natural gas fuel and mixing it with combustion air are two of the critical functions of the gas injection system in dual-fuel engines. A number of approaches are possible, and the choice of approach has a major effect on the emissions and fuel-efficiency of the dual-fuel engine. The most common approach is to meter the natural gas into the intake air charge at a single point upstream of the air intake manifold. The actual metering and mixing of the fuel may be accomplished using either a mechanical gaseous fuel mixer (carburetor), or an electronically controlled gaseous fuel metering system, as shown in Figure 1-1. This approach strives to achieve a homogeneous mixture of air and fuel before the air stream splits in the intake manifold. As discussed by Klimstra [5], failure to achieve a homogeneous mixture at this point can cause significant cylinder-to-cylinder variations in air-fuel ratio. This increases emissions and the possibility of knock phenomena.

A dual-fuel engine designer using electronic gas injection equipment has three options. The first option is to use gaseous fuel injectors to mix the fuel with the intake air

3

A) Gas Mixer / Carburetor Injection   B) Single Point Injection
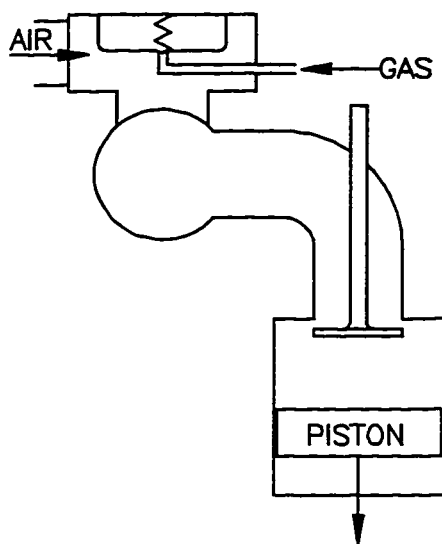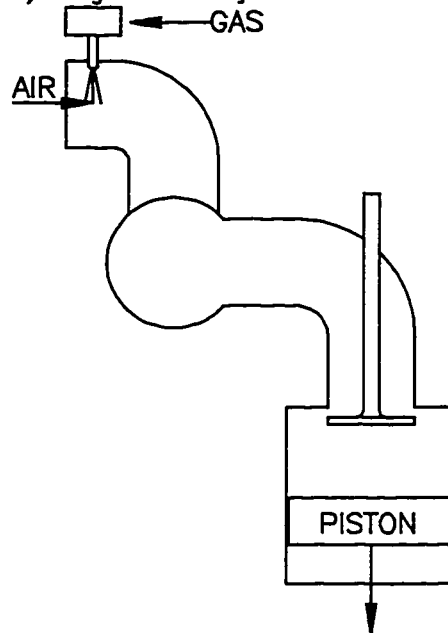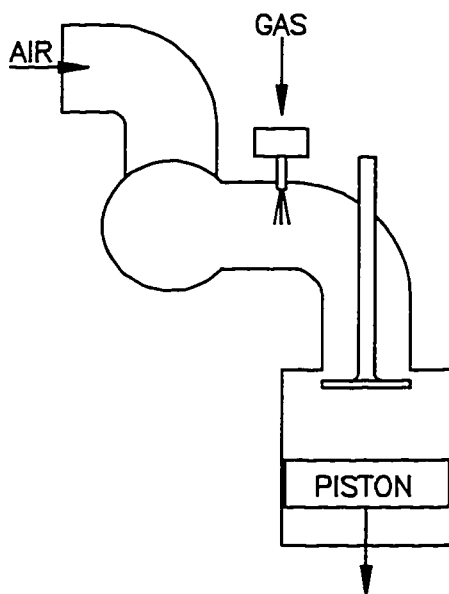
C) Multi-point Injection   D) Direct Injection
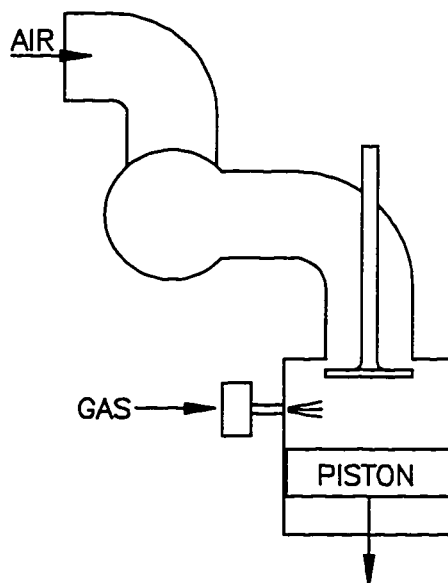
Figure 1-1. Different methods of gas injection used in dual-mode engines.

4

in the manifold at one location, (single-point injection). In this case, fuel is injected in a single location much like a gas mixer/carburetor. Single point electronic injection offers the advantage of more precise control of the amount of gaseous fuel entering the intake charge of the engine as well as economy of using a minimum number of injectors.

The second option is to inject the fuel into the air in front of each cylinder intake port, (multi-point injection). This system uses one or more fuel injectors for each cylinder intake port of an engine and allows the designer to remove the fuel supply from the air supply section of the intake manifold. The third option is to inject the gaseous fuel directly into each combustion chamber (direct injection). In the latter case, it is necessary to provide considerable turbulence during the compression stroke to achieve adequate air-fuel mixing. A high-turbulence, high-swirl combustion chamber is desirable for this type of injection. Figure 1-1 demonstrates the schematics of these methods.

Present dual-fuel engine designs sometimes produce excessive HC and CO exhaust emissions. There are a number of reasons. Under normal combustion conditions, HC emissions are due primarily to unburned mixture forced into crevice volumes during compression. Another source of high HC emissions in dual-fuel engines, using a premixed air-fuel charge, is over-scavenging of the cylinder, resulting in unburned mixture blowing through the chamber and out the exhaust. In addition, under light-load conditions, air-fuel mixtures in the cylinder may be too lean to burn efficiently. This results in high concentrations of unreacted or partially reacted fuel in the exhaust. Karim [6] has studied this condition extensively. As the air-fuel ratio approaches the lean flammability limit, the flame front initiated by the combustion of the diesel pilot no longer propagates through the entire combustion chamber, but is limited to the volume immediately surrounding the pilot fuel. The fuel in the remaining charge does not burn, but continues to undergo pre-flame reactions until it is exhausted from the cylinder. Among the major products produced by the preflame reactions are CO and formaldehyde (HCHO). Concentrations of these species in the exhaust increase dramatically as mixture strength decreases past a critical air-fuel ratio.

These problems of the dual-fuel engines can be partially controlled by fuel injection design. The most advantageous design is multi-point injection design where the gas fuel mixes with only part of the incoming airflow, consequently reducing cylinder to

cylinder variation. In addition, by using a timed sequential fuel injection system, it is possible to control the fuel injection timing so that the gas injection begins when the intake valve is opened and exhaust valve is already closed. As a result, there are less scavenging loss and there is a possibility of stratification in cylinder. However, this system does have the disadvantage that the fuel and air do not have as much time to mix and to form a homogeneous charge in the intake manifold. Nevertheless, since the air and the gas flow directly into the cylinder, with the turbulence induced by jet injection and by the intake valve, rapid mixing is possible. As such, there is a strong incentive to study and to understand the jet injection process in the air intake manifold combined with turbulent mixing phenomena.

1.4. Overview of Research

To solve existing problems, a considerable amount of information on mixing phenomena of turbulent jets is required. Chapter 2 introduces the physics of gas jet interactions, reviews results from studies of related problems and summarizes information gained from them for the current research.

Chapter 3 discusses the development of an experimental gas injection model and describes the Fast Flame Ionization Detector (FFID) technique and instrumentation used to study gas mixing in this investigation. It also introduces methods chosen for data collection and analysis, and evaluates potential errors associated with this type of analysis.

Chapter 4 shows the results from preliminary experiments on interaction of continuous jets of gas and air in a crossflow confined environment, and discusses the suitability of this technique for pulsed injection experiments.

Chapter 5 presents and reviews results from the study of turbulent pulsed jets in a crossflow environment.

The application section of the thesis, Chapter 6, discusses the experimental data from using different geometries of gas injector and the conclusions developed from this.

Chapter 7, the final chapter of the thesis, reviews what has been learned and makes some recommendations for future research.

2. Literature Survey and Background

2.1. Jet Mixing Application

Metering and mixing of natural gas with intake air are the major problems for dual-mode diesel engine designers. The problems experienced with natural gas mixing become particularly evident when faced with the strict emissions standards that are in force now throughout most of the world.

In vehicle fuel systems, rapid changes in the fuel demand as well as variation in the gas composition can cause large deviations from the optimum equivalence ratio. An additional complication is associated with the pulsating gas and air flow rates within this system. These problems can be partially solved by choosing the sequential multi-point gas injection system which utilizes separate fuel injectors at each cylinder intake port of the engine. In this system the natural gas, at several atmospheres supply pressure, passes through choked flow gas injectors which meter the gas to each respective intake port. In the dual fuel mode the actual metering and fuel delivery are accomplished with the use of Servojet High Speed Solenoid Valves (HSV) injectors activated by an on-board engine control computer.

The required injection quantity of natural gas and injection timing is calculated prior to each cylinder intake stroke based on a map of fuel requirements and the injector's fuel delivery characteristics. To build this map the engineer has to know how rapidly injected gas mixes with the air stream in the intake manifold and the final composition of mixture just before it is entering the intake valve. These characteristics of mixing process can be affected by many factors, such as injector geometry, injection pressure, pulse duration, intake manifold geometry, etc.. To develop the proper injection system, all these factors have to be accounted for and their effects have to be evaluated. The present study concentrates on detailed features associated with the axisymmetric jet in crossflow, features that can be enhanced by proper geometrical and timing modification to aid the process of jet mixing in the air-intake manifold.

The processes of injection and mixing find wide application throughout engineering and science. Engineering design requirements in this field often result in flow problems that are very complex from an analysis point of view. The combinations

of flow rate, nozzle geometry, and thermophysical properties of fluids of practical interest are usually such as to produce turbulent flow, which enhances the process of mixture formation. Experimental and analytical studies of injection and mixing in turbulent flow go back many years, and the literature in the field is very rich. Good overviews on turbulent jets' behavior can be found in works by Abramovich (7), Rajaratnam (9), Brodkey (8), and Bradshaw (10) or in fluid mechanics reference texts such as Pai (11). The rate of work in this area, however, is not diminished; indeed it seems to be accelerating due to numerous practical applications of jets.

2.2. Classification of Jets

The present study is an example of actual engineering application of jet mixing phenomena in the design of gas injection systems. The correct approach to this study would be to classify the problem of gas injection into the diesel engine air-intake manifold by using all available information on the subject. The process of collecting this information involved a thorough literature survey from which an interesting conclusion has been drawn. The fact is that no ready-to-use complete jet classification system is available in the literature. Due to the complex nature of jets, it is quite difficult to envelop all possible variations of geometries and fluid conditions of jets in one system. Nevertheless, the attempt to construct such a system has been made by the author, and results are presented in Table 2-1.

The jet classification system was developed by carefully sorting out major characteristic parameters from existing literature descriptions of jets. There are a few parameters that can be considered important. These include: the phase of jet flow and surrounding flow, flow physical properties, presence and configuration of confining walls, flow direction of interacting fluids and regimes of flows. All these parameters will be discussed in the following paragraphs.

At first, a jet can be classified by its transience factor (steady or non-steady flow), and by physical and geometric properties of the jet flow only. Obviously, to make a complete picture, one has to know about physical and geometric properties of the surrounding fluid as well. Moreover, to predict development of mixing proceses and the jet's behavior at all, the designer must know about the nature of jet interaction with its

8

surrounding. Therefore, all of these factors were included in the list of major characteristics.

Table 2-1. The jet classification system.

Fluid phase combination	solid spray	liquid spray	one phase		two phase		multiphase
			liq.-liq.	gas.-gas.	liq. -gas.	gas. -liq.	
JET FLOW							
Transient factor	steady <———————————————————> non-steady						
Compressibility factor	M < 1			M ≈ 1		M > 1	
Jet regime	laminar (Re < 2300)				turbulent (Re > 2300)		
Jet condition	axial non-swirling				swirling		
Jet direction	radial		directional		impinging on another jet	impinging on the wall	
Jet shape	plane		rectangular	square		oval	circular
Jet relative density	buoyant			neutral		dense	
SURROUNDING FLOW							
Transient factor	steady <———————————————————> non-steady						
Compressibility factor	M < 1			M ≈ 1		M > 1	
Flow regime	laminar (Re < 2300)				turbulent (Re > 2300)		
Flow condition	nonswirling				swirling		
Flow curvature	straight			single curved		multi-curved	
Flow direction	parallel flow		crossflow		oblique flow		opposite flow
WALL CONFIGURATION							
Free jets	confined environment				open environment		
Wall jets		non-impinging		impinging			

Finally, jet behavior becomes quite different, compared to the open environment case, if it is confined in some type of enclosure. Surrounding walls can affect jet flow by direct impingement and by controlling entrainment flows. That is the last descriptive parameter in the system.

According to the newly developed classification system, the specific case of gas injection into an air-intake manifold is highly complex in nature. The features that characterize this problem are as follows: crossflow turbulent jets interaction; variable density flows; impingement of pulsed gaseous jet on the opposite wall; confined, smooth, curved duct environment. Evidently, to proceed further with analysis, a thorough study on behavior and physical characteristics of turbulent jets in crossflow has to be done. The next section presents a short review of this study.

2.3. Steady Turbulent Gas Jets in Crossflow

2.3.1. Background of jets in crossflow

The study of jets in crossflow (JICF) has received considerable attention because it is the major problem for many practical situations. For each case of research on JICF there may be a different emphasis in the flowfield investigation. Within the context of this study it will be important to discuss the essential ideas, to specify the points that would help to understand the mixing phenomena due to jet interaction and, if possible, to relate this to a case of gas injection into an air-intake manifold.

It has a long been recognized that a jet exhausting normal to a crossflow generates a complex flowfield with several distinguishing futures. The rather complex interaction between the two flows produces the deflection of the jet in the free stream direction. The jet boundaries spread as a result of entrainment in much the same way as occurs with a jet issuing into still air. The mixing can be considered occurring in two zones: the near-field and the far-field. The near-field extends downstream from the point of jet discharge to a point where the vertical concentration across each cross section is uniform. Once vertical mixing has been established in the near-field, the mixing is essentially proceeds in two directions: radial and longitudinal. The region downstream from this point is called the far-field zone.

10

Table 2-2. Summary of experimental investigations of round turbulent JICF.

Author (ref.)	D jet [mm]	Incident angle	Jet velocity profile	Ambient velocity [m/s]	Velocity ratio	Measured parameters
Callaghan & Ruggeri (12)	6.3, 9.5 12.7	90	orifice	-	-	penetration parameters
Keffer & Baines (13)	9.5	90	pipe	1.5	4, 6, 8	velocity, turbulence intensity , entrainment
Platten & Keffer (14)	6.3	15, 30 45, 90	pipe	1.6	4, 6, 8	jet trajectory, entrainment
Thompson (15)	25.4	90	nozzle	12.2	2, 4, 8, 12 16, 20	wall static pressures, turbulence intensity
Kamotani & Greber (16)	6.3	90	pipe	6 - 9	2.8 – 8.5	velocity and temperature distributions
Chassaing et al. (17)	40	90	pipe	3.4	2.37, 3.95 6.35	velocity distributions
Fearn & Weston (18)	101.6	90	orifice	30.4	53.3	velocity and vorticity
Moussa & Trischka (19)	23.6	90	pipe	8.5	3.48	velocity and vorticity
Campbell & Schetz (20)	1.58	40, 90	orifice	-	9, 29	jet trajectory, velocity and temperature distributions
Fric & Roshko (21)	38	90	nozzle	1.5, 3, 4.5	2, 4, 6 8, 10	velocity and vorticity
Birch et al. (22)	2.7	90	orifice	-	-	structure and concentration decay of jet
Crabb et al. (23)	25.4	90	pipe	12	1.15, 2.3	velocity distributions
Pratte & Baines (24)	6.3, 9.5 12.7	90	orifice	3, 3.8 12	5, 15 25, 35	jet trajectory, velocity profiles

Far downstream of the pipe outlet, the deflected jet is dominated by a counter-rotating vortex pair that seems to originate at the jet exit. In the near-field zone, the jet structure consists of ring-like vortices which become distorted with the streamwise distance. Details of entrainment and interaction between these flow elements are not fully understood. This has led to numerous experimental and numerical studies with the aim of gaining an insight into this complex flow. A guide to previous experimental work is provided in Table 2-2 which shows that, although the range of parameters covered is large, there is still a lack of detailed information, especially on the process of mixing.

2.3.2. General description of JICF

There have been many studies done in an effort to characterize the structure of the steady turbulent JICF. Properties of the JICF that received early attention were determinations of the jet's trajectory and geometry. The path of the jet associated with the locus of maximum velocity, and the path of maximum vorticity projected to the symmetry plan were defined as major geometrical characteristics. The jet path and jet induced flows depend mainly on the ratio of the momentum flux across the jet orifice to the momentum flux of the crossflow over an equal area. It is conventional to define an effective velocity ratio R as the square root of the momentum flux ratio (18).

$$R = \left(\rho_j U_j^2 / \rho_\infty U_\infty^2 \right)^{\frac{1}{2}}$$ (2.1)

where U_j - jet velocity, averaged across d, m/s

 d   - jet orifice diameter, m

 U_∞ - freestream time-average velocity, m/s

 ρ_j - density of the jet fluid, kg / m^3

 ρ_∞ - density of the freestream fluid, kg / m^3.

If $\rho_j = \rho_\infty$ and speed U_j is a constant across the jet orifice then the above equation can be written simply as the ratio of the jet to crossflow velocity:

$$R = U_j / U_\infty$$ (2.2)

12

The main characteristics of the flow for the case of a 90-degree, unconfined injection were presented in the work by Abramovich (7). In this study, the experimental observations have shown that due to the stagnation pressure exerted by the free stream, the circular jet becomes deflected, and the flow spreads laterally into an oval shape. At the same time, the crossflow shears the jet fluid downstream along the lateral edges to form a kidney shaped cross-section. At increasing distances along the jet path this shearing folds the downstream face over itself to form a vortex pair which dominates the flow. The whole structure of jet discharge in crossflow can be divided into three regions, Figure 2-1.
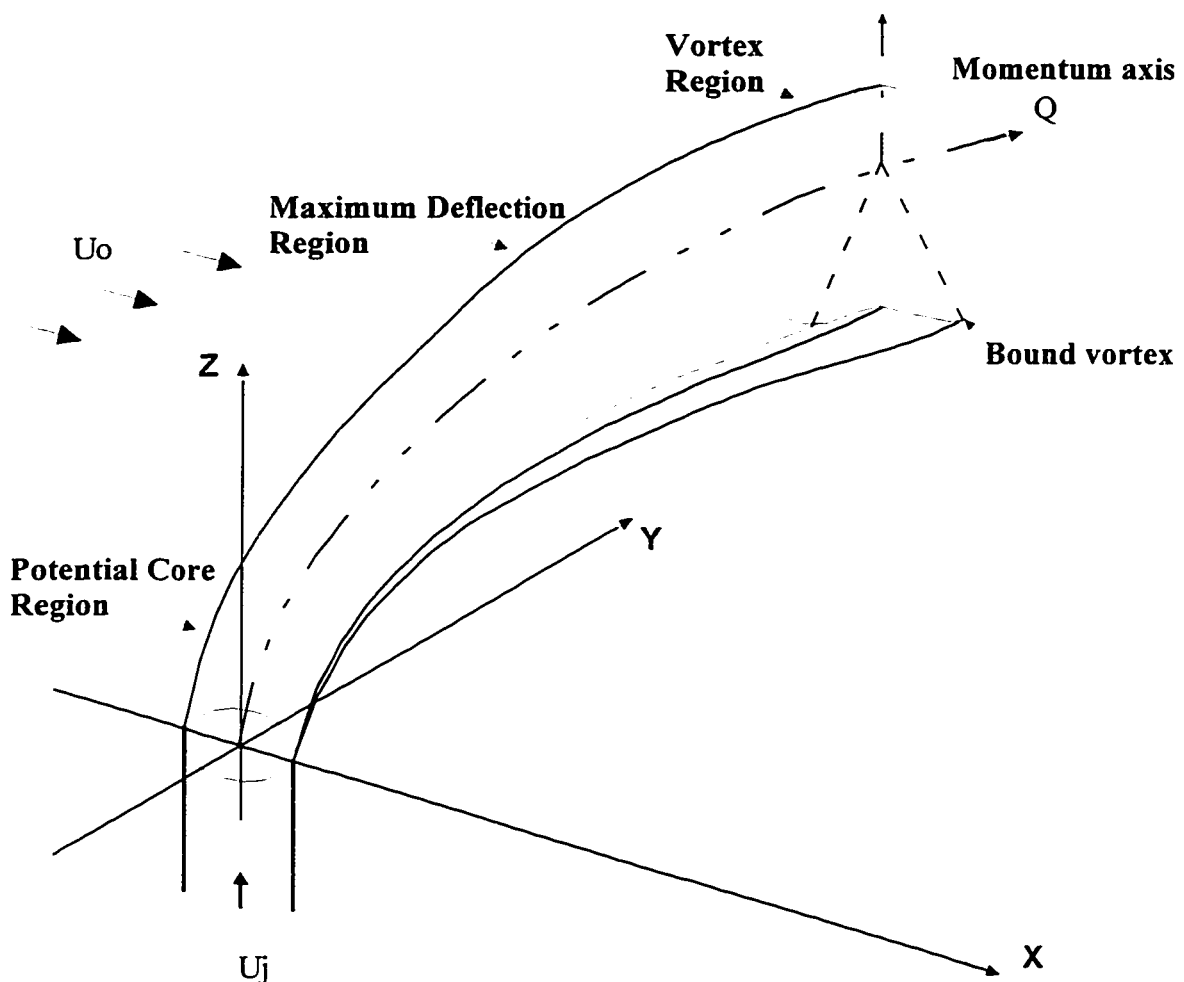
Figure 2-1. General flowfield description of a round jet in cross-flow (19).

13

As the jet is acted upon by the free stream, there is a central region of relatively shear free flow of undiminished total pressure, which decreases steadily in size and eventually disappears. This region is generally known as the **potential core region**. As the jet extends further into crossflow, the outer boundaries of the jet increasingly interact with the free stream fluid. In the work conducted by Keffer and Baines (13), it was suggested that for effective velocity ratio R $\geq$ 4, the end of the core region is located directly over the center of the jet, and for R < 4, this point is pushed downwind. Pratte and Baines (24), in their research, have found that the length of the potential core varies mainly with the velocity ratio R. Usually, very little deflection of the jet can be observed in this zone.

From the end of the potential core zone, the jet suffers a large deflection in a certain length that is known as the **region of the maximum deflection**. The characteristics of this zone are very important when considering jet geometry, velocity distribution, and profiles of concentration field. In this region, the pair of counter-rotating vortices along with components of a secondary vortex system, grow in size while maintaining their angular velocity. This is because the outer layers of the jet lose their momentum through the entrainment of free stream fluid into the potential core region. During the progression of the jet through the zone of maximum deflection, the total flow rate of the jet increases while the value of velocity decreases.

The remaining portion of the deflected jet is referred as the **vortex region**, where the vortices continue to grow in size but their angular velocity decreases. The jet's direction and jet velocities in this zone are approaching those parameters of the free-stream. The process of mixing in the vortex zone starts to be influenced by the turbulence of the ambient fluid.

2.3.3. Vortical structure of JICF

Compared to other free shear flows, the JICF displays considerably more intricacy ranging from jet-like behavior in the near-field to a counter-rotating vortex pair in the far- field and including the issue of curvature as the flow progresses downstream. A deeper study of the flow structure in the near-field of an axisymmetric turbulent jet in a uniform cross-flow has been conducted by Fric and Roshko (21) and Krausche et al. (25).

14

Fric and Roshko (21), have provided many detailed visualizations of the near-field and have identified four main vortical structures that comprise the flow, as it can be seen in Figure 2-2.
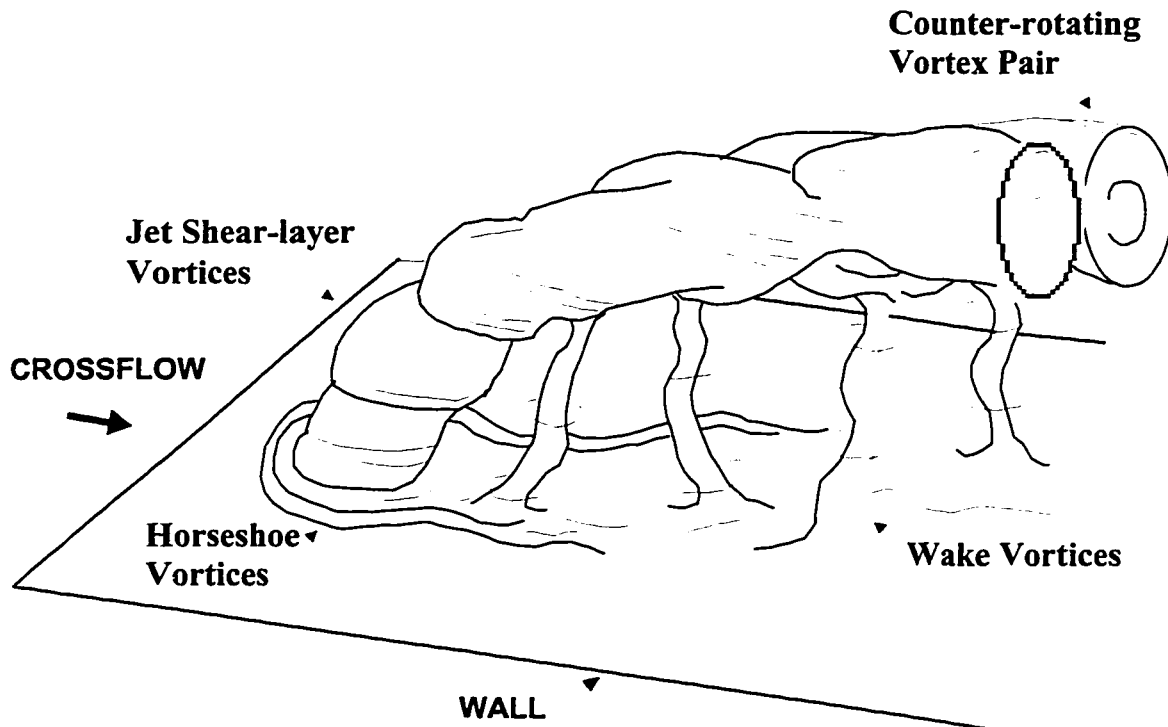
Figure 2-2. Picture depicting four types of vortical structure associated with the transverse-jet near-field (21).

These vortical structures can be described as follows: 1) the dominant rolled-up longitudinal vortex pair, that develops on either side of the jet as it spreads downstream; 2) the horseshoe vortex, that appears around the jet exit due to the wall boundary layer wraps around the jet column; 3) the unsteady wake vortex street shedding immediately downstream of the jet exit and connecting the jet to the wall; and finally, 4) the jet shear layer ring vortices which evolve on the jet column. These studies convincingly demonstrated that the wake vorticity originates in the flat plate boundary layer, and wake vortices are in no way related to vortex shedding from the jet column. On each side of the jet, the boundary layer separates due to the high adverse pressure gradient, and creates

an alternate vortex shedding. The mechanism by which a transverse jet's wake forms is different and distinct from the shedding of vorticity from a solid cylinder. In the case of large effective velocity ratio (R > 4), the wake vortices do not interact strongly with the jet. For small injection ratio (R < 4), such vortices impose a drastic change in the jet behavior. The conclusion has been made that the downstream momentum, which the jet acquires during interaction, must be at the expense of crossflow, and that the momentum exchange in this case is accomplished by dissipative jet-crossflow mixing.

The main characteristics of the jet in cross flow interaction are the well known counter rotating vortices. Fearn and Weston (18) investigated the behavior of these vortices for the momentum flux ratios R^2 varying from 9 to 100. Two vortex models were studied. The first was a simple vortex filament model where the strength and the location of the vortex were determined using the velocity measurements in the symmetry plane. The second model was a diffuse model where a Gaussian distribution of vorticity was assumed. For this later model, velocity measurements in the whole cross section of the jet are required to compute the strength, the location, and the diffuseness of the vortex. With the help of this model, Fearn and Weston (18) produced data for the core radius, the vortex strength, and the vortex trajectory as a function of the distance from the jet exit. It shows that the influence of the momentum ratio on the vortex strength is predominant whereas it is negligible on the vortex core size. The comparison of the two models shows that the simple filament model is in good agreement with the diffusive model predictions. This implies that one can expect a rather good prediction of the jet characteristics with only the velocity measurements in the symmetry plane, which reduces considerably the required amount of measurements.

2.3.4. Velocity and trajectory of JIFC

There are a great variety of empirical expressions obtained by researchers for the path of maximum velocity for 90° jet deflection angle and for variable velocity ratio. Smy and Ransom (26) compared these equations and found that the analytically derived equation by Wooler (27) fit best with the experimental data. For the purpose of comparison, a slightly modified version of this equation is shown next.

16

$$\frac{z}{d} = \left(\frac{x \cdot R^n}{A \cdot d}\right)^{1/m}$$

(2.3)

where x, z - Cartesian coordinates

A   - coefficient used in trajectory equation

m, n - exponents used in trajectory equation.

This equation was improved by taking the [z] origin at the end of the jet potential core. Comparisons of the coefficient [A] and exponents [n] and [m] used in the above equation by various investigators were reviewed in the work by Margason (28) and have been updated by the author for the present discussion. A summary of this comparison is presented in Table 2-3.

Table 2-3.   Summary of investigations on trajectory of jet in crossflow.

Author (ref.)	A	m	n
Wooler (27)	2.63	2.0	2.0
Patrick (29)	constant	0.85	2.86
Storms (30)	0.195	2.0	3.0
Kamotani & Greber (16)	1.21	1.64	1.58
Fearn (31)	1.07	3.18	2.99
Ivanov (32)	1.0	2.6	3.0
Shandorov (33)	1.0	2.0	2.55
Snel (34)	1.86	2.01	3.01
Jordinson (35)	2.3	3.0	3.0
Callaghan et al. (12)	$0.118 \rho_j / \rho_\infty$	2.0	3.0
Pratte & Baines (24)	0.077	3.57	2.57
Schetz & Billig (36)	ρ_j / ρ_∞	2.0	2.3

This table shows that the [A] term tends to be either a numerical constant or a variable involving density ratio. The [n] and [m] exponents tend to vary from 2 to 3 in value. As shown in reference (28), the most robust empirical expression seems to be that obtained by Ivanov (21).

Most of the experiments also show that, in the far-field, the jet penetration [y], the jet centerline distance from the jet exit plane, and the vortex spacing , [2r], vary with the downstream distance[x] raised to a power close to one-third. These experiments dealt

17

with flows at high Reynolds number where viscosity plays no global role and only serves to dissipate energy at the Kolmogorov microscale. Hence, the only global characteristic jet length [l] in the above-described limiting flow is (50):

$$l = \left(\frac{\dot{m}_j U_j}{\rho_\infty U_\infty^2} \right)^{0.5} = \left(\frac{1}{4} \pi \cdot \frac{\rho_j}{\rho_\infty} \right)^{0.5} R \cdot d \qquad (2.4)$$

where $\dot{m}_j$ - mass flow of jet, defined as $\rho_j U_j d^2 \frac{\pi}{4}$, kg/s.

In most experimental investigations it has been noted that the length scale of the JICF varies proportionally to the $R \cdot d$ value and that far-downstream penetration [z] and jet width [w] varies with downstream distance [$x^{1/3}$]. Pratte and Baines (24), for example, find that the expression:

$$\frac{z}{R \cdot d} = 2.05 \left(\frac{x}{R \cdot d} \right)^{0.28} \qquad (2.5)$$

describes the jet centerline location for injection ratio R ranging among 5 and 35. Pratte and Baines (24) also presented the jet width equations as a function of the distance downstream of the jet exit:

$$\frac{w_z}{R \cdot d} = 1.54 \left(\frac{x}{R \cdot d} \right)^{0.4} \qquad (2.6)$$

$$\frac{w_y}{R \cdot d} = 1.24 \left(\frac{x}{R \cdot d} \right)^{0.4} \qquad (2.7)$$

where w_z - jet width for the side view, mm

w_y - jet width for the plane view, mm.

Many previous studies have determined the path of the jet by flow visualization techniques or by velocity measurements. In the latter case, the jet centerline, which is defined as the locus of points of maximum velocity in the symmetry plane, was usually used to describe the jet path. The papers by Fearn and Weston (18), Kamotani and

18

Greber (16), and Thompson (15) are good examples of such methods of experimental investigation of the velocity field associated with a jet in crossflow.

Kamotani and Greber (16) made extensive velocity and temperature measurements for both heated and non-heated round jets, exhausting through a flat plate with a momentum flux ratio R^2 varying from 15 to 60. They derived correlations for the velocity and temperature trajectories, defined as the location of the maxima of velocity and temperature. The path of maximum temperature is compared with the path of maximum velocity in Figure 2-3.
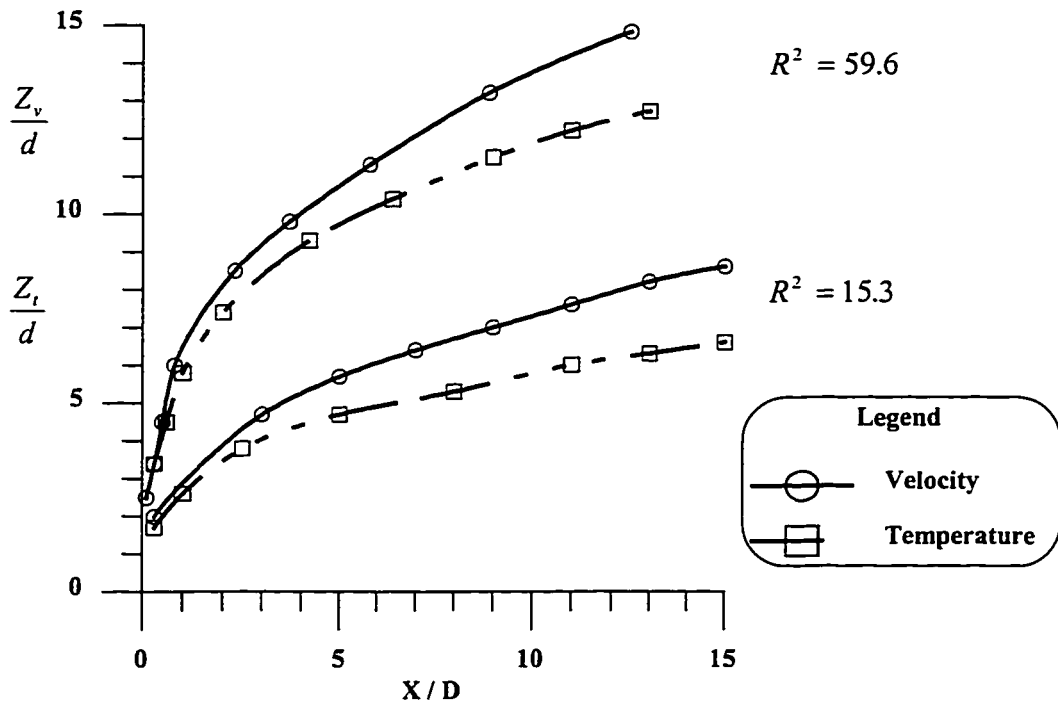
Figure 2-3.   Velocity and temperature centerline profiles of JICF for

different momentum ratio R^2 (16).

For a given momentum flux ratio, this maximum temperature path penetrates the free-stream less than the maximum velocity trajectory. It was found that when the jet temperature increased, the strength and size of the vortex motion also increased. Ricou and Spalding (37) have shown that increasing jet temperature causes more entrainment

and makes the vortex motion active. A similar effect is noted for the free jets where the increasing jet temperature causes more entrainment due to higher density ratio.

With a simple jet, entrainment occurs only by the spreading of the turbulent front. In the case of JICF, this is augmented considerably by the action of the vortices which cause an internal circulation and hence large scale mixing within the jet. In addition, some external fluid with small momentum is carried into the center of the wake by the lateral shearing action. The total mass flux across the outside jet boundary is, therefore, significantly greater than in the free jet.

Most theoretical attempts to explain the jet motion involve integral methods, and many simplifying assumptions, particularly with regard to entrainment. To predict the inner structure of the deflected jet more accurately, Adler and Baron (38) improved Wooler's (27) calculation method for jet induced effects. For that reason, they incorporated Chang's (39) method for determining jet cross section shape and a newly developed method to represent the velocity profile within the jet cross section. An entrainment model coupled with velocity decay, cross section shape change and area growth was developed. The ideas of Ricou and Spalding (37) and Keffer and Baines (13), where the entrainment is composed of straight jet entrainment and vortical entrainment, were used. It was shown that the computed jet cross section compared quite well with the experimental results of Kamotani and Greber (16).

Experimental work by Crabb et al. (23) has proven the general trends of previous investigations. The contour plots of mean velocity and concentration confirmed that the locus of maximum velocity does not correspond to fluid from the jet exit; indeed, the downstream regions of high velocity are shown to be composed mainly of free-stream fluid. Comparison of contour plots of mean velocity and concentration also shows large differences between the distributions of velocity and jet fluid concentration. In particular, the outer velocity maximum corresponds to a region of low jet fluid concentration and to free-stream fluid forced to accelerate around the obstruction caused by the jet. The origin of this outer velocity maximum seems to coincide with the beginning of the wake recirculation. The jet fluid is pulled into its wake by free-stream fluid which accelerates around the jet. The velocity deficit across the wake is balanced by the momentum of the spiraling vortex pair.

20

2.3.5. JICF in confined environment

Much of the published work on JICF has centered on the unconfined problem. For confined crossflow, the experimental data are much scarcer. Holdeman and Walker (40) investigated a geometry relevant to the combustor dilution jet problem, but only measured the temperature field. Catalano et al. (42) reported measurements on velocity characteristics of a confined coaxial jet and found that confinement has beneficial effects on the mixing rate of coaxial jets.

Theoretical work on the confined problem is restricted to the calculations of Tatchell (41), who was concerned with very low velocity ratios.

Some interesting results from computation of parameters of round turbulent jets in confined crossflow are discussed by Jones and McGirk (43). This paper presents a finite-difference scheme suitable for such complex flows and compares the calculated results with the measurements of Kamotani and Greber (16). Jones and McGirk (43) presented measured and predicted contours of the x-component of velocity on planes of constant (x), and measured and calculated trajectories of the jet for two values of momentum flux ratio, namely $R^2 = 18$ and 72. For the lower momentum flux ratio, the vortex motion in the plane of the jet cross section deformed the jet from its original circular shape to the well-known kidney shape. The higher momentum ratio was such that the jet impinged on the top wall and the kidney shape did not reappear after that. Downstream of the impingement point the jet flattened against the top wall and spread in the transverse direction with a velocity maximum on either side of the plane of symmetry.

If the velocity ratio is large enough for impingement on the confining wall, additional complexities arise in the flowfield of JICF. A recent review article by Ince and Leschzin (44) discussed the crossflow jet impingement problem. From a physical point of view an impinging jet can be viewed as a synthesis of diverse flow patterns, namely a mixing zone, a free turbulent jet, a stagnation region, a wall jet flow, and finally a vortex system. When, in addition to crossflow, jet impingement occurs, a strong radial wall jet forms at the impingement wall and its interaction with the crossflow causes an extensive horse-shoe-shaped wall vortex, interacting with the oncoming cross-stream, as shown schematically in Figure 2-4.
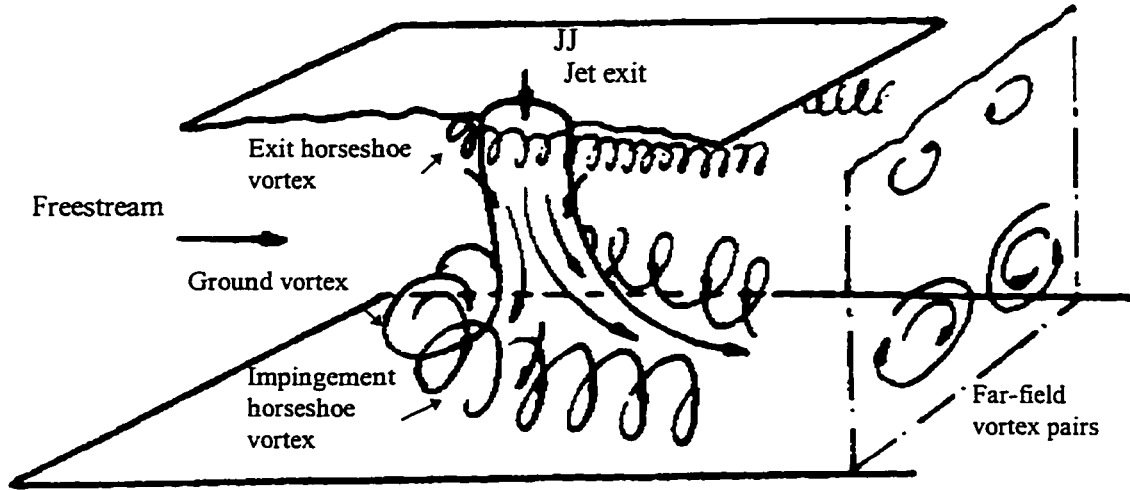
Figure 2-4. Sketch of jet-induced flow for impinging transverse jet on a wall (44).

The wall jet flow does not spread indefinitely; it will ultimately decay from viscous dissipation or be stopped by some intervening mechanism. In the crossflow environment, the upstream component of the wall jet will separate from the wall some distance forward of the impingement point. A large elliptical separation bubble is created which has been termed the "ground vortex" due to its rotational nature. It is not a vortex in the sense of increasing local velocities as the core is approached, but a turbulent separation bubble inside which the jet and free-stream flow mix. The forward penetration of the ground vortex increases with the jet to free-stream momentum ratio.

Colin and Olivari (62) developed a semi-empirical expression for the upstream penetration by assuming the kinetic energy in the cross flow at the separation point is equal to the kinetic energy of the wall jet. Assuming negligible decay of the gas jet, their parameter can be written in terms of the jet exit velocity as follows:

$$\frac{x_s - x_i}{d} = 1.03(U_j / U_\infty)^{0.9} = R^{0.9} \tag{2.8}$$

where x_s - upstream distance from jet centerline to ground vortex

        separation point, mm

   x_i - distance along ground from jet centerline to impingement point, mm.

22

To account for the height of the jet exit above the opposite wall (h), Stewart and Blake (63) postulates a modified form of Equation 5.1 which uses (h/d) as the correlating parameter:

$$\frac{x_s - x_i}{d} = R^{0.9}\left[1 + 0.1\frac{h/d}{R^{0.9}} - 0.3\left(\frac{h/d}{R^{0.9}}\right)^2\right] \qquad (2.9)$$

where h - the hight of the jet above opposite wall, mm.

In the case of the impinging jet, the growth of the jet on the wall decelerates rapidly and the jet tip penetration during the injection period of 11 ms is almost proportional to the half power of the time (64):

$$r_p = K_r\left(t_{ing} - t_i\right)^{1/2} \qquad (2.10)$$

$$h_p = K_h\left(t_{ing} - t_i\right)^{1/2} \qquad (2.11)$$

where r_p - jet spread after impingement, mm

h_p - jet height after impingement, mm

K_r - constant, 17.5 (64)

K_h - constant, 5.7 (64)

t_{ing} - time from injection start, ms

t_i - time difference between start of injection and impinging, ms.

In the case of the co-flowing jet, the penetration length (L) of the jet tip is almost in proportion to the half power of injection time (65):

$$L = Ft^{1/2} \qquad (2.12)$$

where F is a function of the injection pressure, $2.42d\left(\dfrac{U_j}{d}\right)^{1/2}$.

2.3.6. Density consideration in JICF

The literature on variable density jets has many discrepancies concerning the centerline decay rate, spreading behavior, attainment of asymptotic centerline

23

unmixedness value (the ratio of the r.m.s. to mean value of scalar), and self-preservation behavior. The fact that constant-density turbulent jets exhibit self-preserving behavior in the far-field has been generally accepted. Dowling and Demotakis (45) confirmed this behavior in a careful investigation of constant-density axisymmetric jets. Global density effects on the self-preservation behavior of free turbulent jets were investigated in the recent work of Richards and Pitts (46). Their findings from an experimental study of mixing in variable-density axisymmetric jets showed the similarity behavior of these flow fields in regions well beyond the potential core where the turbulent flow is fully developed. The goal was to test the hypothesis that axisymmetric turbulent jets become asymptotically independent of source conditions. Effects of initial conditions were investigated by varying the jet boundary conditions and the global density ratio of jet and ambient gases, $R_\rho = \rho_j / \rho_\infty$. Initial density differences were imposed by using three different jet gases: helium, methane, and propane injected into the air stream.

The results show, that regardless of the initial conditions, axisymmetric turbulent jets in cross-flow decay at the same rate and spread at the same angle. Both the mean and r.m.s. values collapse in a form consistent with full self-preservation. The means and fluctuations follow a law of full self-preservation provided that two virtual origins are specified. Memory of the early jet core is embodied in these virtual displacements. Richards and Pitts (46) demonstrated that if care is taken to ensure that the flows are uncontaminated by buoyancy and coflow effects then, the far-field mixing behavior of variable-density jets is indistinguishable from constant-density jets.

2.3.7. Concentration fields in JICF

The nature of concentration fields produced by turbulent free jets is well documented in the literature. Good examples for this are papers by Wilson and Dankwerts (47), Becker et al. (48), and Wygnanski and Fiedler (49). The mean and fluctuating concentration field in natural gas jets has been studied in some detail by Birch et al. (22). The distance taken for the mean concentration to decay to a given value in such flows is proportional to the diameter of the injector nozzle and inversely proportional to the square root of the density of the jet fluid, but it is independent of jet velocity. However, as the driving pressure and hence jet velocity increase, a point is

24

reached at the critical pressure ratio when the jet exit velocity reaches the speed of sound. At higher pressures, the exit velocity remains locally sonic, but the exit pressure rises above ambient pressure with the result that expansion down to ambient conditions takes place outside the nozzle. The resultant concentration field, therefore, behaves as if it were produced by a source larger than the actual nozzle diameter; this is referred to as the pseudo-diameter, which may be presumed to replace the actual diameter in equations describing the concentration field.

The mixture formation in the JICF has been examined mainly by means of flow visualization methods. These works have described the mixing process as being controlled by the turbulence and the growth of the vortex system. Structure and mixing analysis of a JICF in a confined environment was performed in works by Broadwell and Breidenthal (50), and Breindenthal et al. (51), resulting in development of models of mixing in turbulent jets in stationary reservoirs. In applying ideas of these models to the jet in crossflow, it should be noted first that the appropriate far-field Reynolds number is

$$\text{Re}_l = \frac{U_\infty l}{\nu} = \left(\frac{\pi}{4}\frac{\rho_j}{\rho_\infty}\right)^{0.5}\frac{U_j d}{\nu}. \tag{2.13}$$

where ν - kinematic viscosity of the jet fluid, m^2 / s

That means that the initial Reynolds number must be sufficiently high for the mixing process to end before the Reynolds number falls to a level at which flow becomes laminar. The mixing ends when every element of jet fluid is molecularly mixed with at least ϕ (the volume equivalence ratio of crossflow to injected fluid) parts of free-stream fluid. For a constant density jet, with $\rho_j = \rho_\infty$, a mixing of equivalence ratio ϕ ends when the ratio of the total flux of molecularly mixed fluid in the jet to the initial jet flux reaches value $(\phi + 1)$:

$$\frac{U_\infty r^2}{U_j A_0} \approx \phi + 1 \tag{2.14}$$

where the jet area is taken to scale with the square of vortex spacing, r^2,

and A_0 is the initial jet area, m^2.

The analysis and the comparison with experimental results by Broadwell and Breidenthal (50) concentrated on the far-field behavior of the transverse jets. Based on experimental facts and theoretical analysis, an expression to predict the mixing length [x_l] has been constructed:

$$x_l = B\left(\frac{U_\infty}{U_j}\right)^{0.5} (\phi+1)^{1.5} A_0^{0.5} \tag{2.15}$$

where B - constant.

In this equation the mixing length is independent of the Schmidt number, $Sc = \mu/\rho d$, and the Reynolds number, $Re_d = U d \rho/\mu$, of the jet. The measured mixing length of the transverse jets was in a good agreement with a simple description of the far-field behavior, suggesting the model can be useful in practical calculations.

2.3. Pulsed Turbulent Jets in Crossflow

While the structure, trajectory and mixing rate of continuous transverse jets have been investigated in numerous experiments a surprisingly small number of studies have addressed the problem of pulsed transverse jets in confined environments.

Several investigators have used deliberately introduced unsteadiness to improve the mixing rate of jets. In an investigation primarily aimed at the study of large-scale orderly structures in a free turbulent jet, Crow and Champagne (52) found that, even at amplitudes of excitation as low as 2%, the entrainment rate in the first six diameters from the jet exit plane increased by 20% over the unforced case. Favre-Marinet and Binder (53) used a spinning butterfly valve upstream of a nozzle to produce pulsation amplitudes up to 40% of the mean velocity. Both the decay of the centerline velocity and the spreading rate of the jet were strongly increased by the pulsations. Co-workers Curtet and Girard (54) conducted a visualization study of pulsed jets and provided smoke and Schlieren pictures of puff formation. Bremhorst et al. (55) studied pulsed jets, and attributed the increased entrainment of the pulsed jets to their inherently larger entrainment interface structure. This structure consists of an upper portion which looks like the front of a puff (mushroom-like shape) and a lower conical portion which looks

like a jet. The size of the front vortex is continually growing due to entrainment of mass from the jet that is pushing the vortex from behind. It is notable that the jet is spreading in the radial direction because the vorticity of the vortex in the upper position is smaller than that in the lower position. The diffusion and the mixing are very vigorous there and that is a very important feature of the pulsed jet.

Wu et al. (56) presented some experimental results from a study of unsteady jets created by pulsed gas jets in a crossflow environment. A qualitative representation of the plume trajectory from this investigation is shown in Figure 2-5.

Pulsating the jet flow at low frequencies, 1 - 4 Hz, resulted in formation of vortex rings and a jet that penetrated into the free-stream flow more deeply than a continuous jet. When the jet flow was pulsated at high frequencies, in the range 4 - 16 Hz, it behaved quite differently from the low frequency jets although no spin-off vortices could be produced. At higher pulsation frequencies, the flowfields were similar to those of the steady jets in crossflow, though with increased mixing present at the jet boundary.
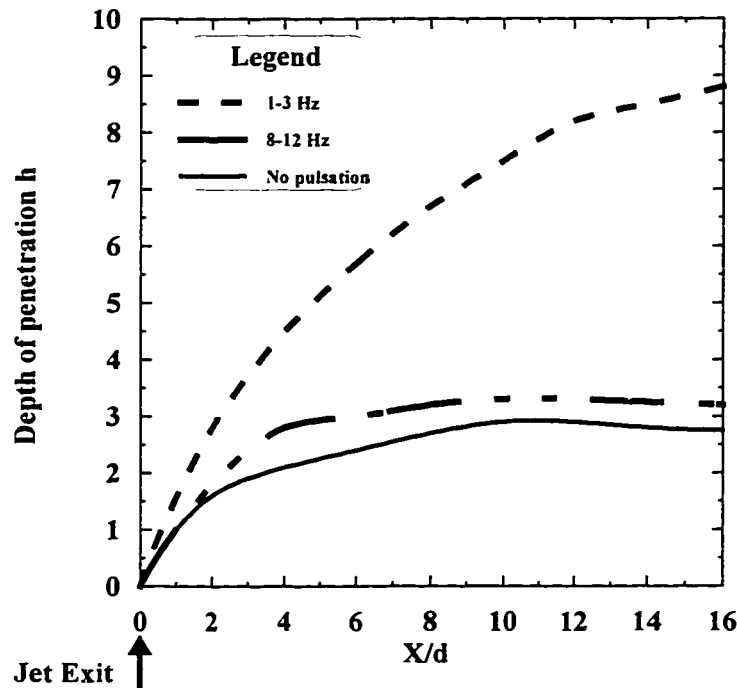
Figure 2-5. Jet plume trajectory with pulsating jet stream (56).

Wu's study also measured three velocity components of the circular JICF with pulsations. The measured time history of velocity components is plotted on Figure 2-6.
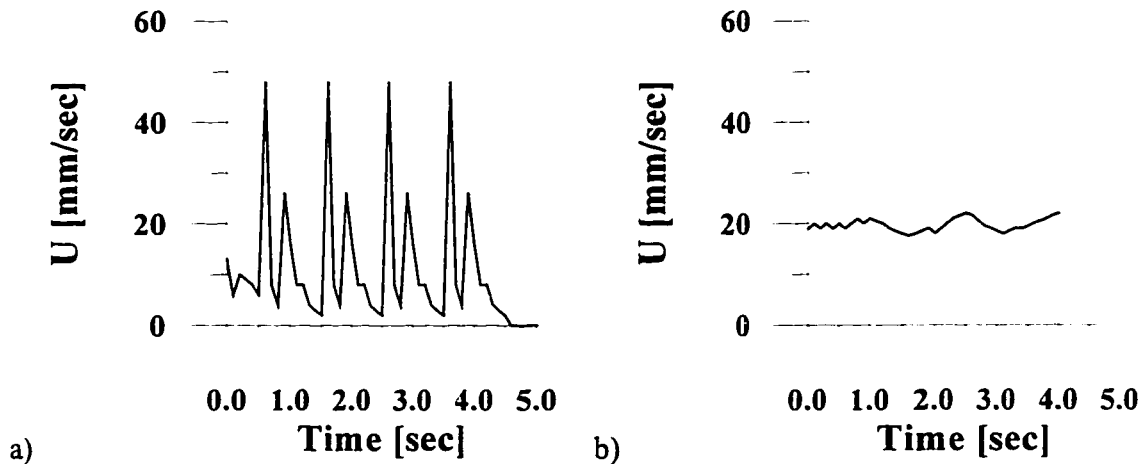
Figure 2-6. Pulsating jet velocity as a function of time measured with a hot film: a) 1 Hz pulse frequency, b) 16 Hz pulse frequency (56).

As can be seen in this Figure, the peak velocities exist on time histograms. These peaks are the major factors that cause the dramatic increase in depth of penetration. The peak of vertical components of velocity decreases almost to a mean value as the pulsation frequency increases.

Though these measurements were done for small velocity ratios, (R = 2 and R = 4.7), the results of this study can be useful for analysis of pulsed jets in cross-flow.

2.4. Summary

This review of research relevant to our study may be summarized by the following conclusions. The structure, trajectory and mixing rate of JICF have been investigated in numerous experiments. The researches carried out in this direction have generally focused on the problems related to V/STOL technology, gas turbine combustors and pollutant dispersion. Few studies have been done on concentration fields of interacting jets in crossflow and almost none of these studies considered the combined effects of compressible jet, density difference and confined environment. The jet trajectory in our case can be predicted using the theories of Pratte and Baines (24)

28

keeping in mind that the situation can be complicated by wall impingement with high momentum flux ratios. It is possible to neglect the effect of density difference in the far-field region, which is the most important zone for our research, based on results of work by Richards and Pitts (46). The jet/freestream interaction flowfield will be not easy to construct because of the complexity of the vortex system and wall effects. Nevertheless, the findings of Kamotani and Greber (16) would help to predict velocity profiles of this system. The concentration field of the mixture formation is the major aim in our research. The analytical formulation of Broadwell and Breidenthal (50) are useful for comparing with our experimental concentration measurements. It is hoped that assumptions made in the previously discussed studies will be helpful guidelines for the current research.

The jet crossflow interactions of gas injection in the simulated diesel engine air-intake manifold will be seen to have combined characteristics of the jets discussed above. Though the range of investigations on JICF problems is very wide, the specific conditions of JICF in a diesel air intake manifold environment have not yet been reported. Therefore, the proposed course of investigation on jet mixing phenomena seems reasonable to undertake. The results of this study will allow fuller understanding of mixture formation and provide a basis for improving the injection system for dual-fuel diesel engines.

3. Experimental Model and Instrumentation

3.1. Objectives for Experimental Research

In light of the literature survey reported in Chapter 2, there is an obvious need to study the mixing process of pulsed, high momentum gas jets in a confined cross-flow environment. Adequate information on this subject is not available from the literature.

At the outset, the basic goal of this study was to understand the flow mixing phenomena in dual-mode diesel engine air-intake manifolds. To avoid the added complexities of tests on a real diesel engine, an experimental model has been developed for the investigation. This model represents part of an air intake manifold with injection system hardware attached to it. The differences and similarities between the model and diesel engine air intake manifold presented in the Table 3.1.

Table 3-1. Characteristics of experimental model and air intake manifold.

Parameters	Experimental Model	Engine Manifold
Overall Geometry	Straight circular duct, $\varnothing$ 50 mm, L = 400 mm	Slightly curved duct with rounded rectangular cross section, L = 280 mm
Injector Tube Geometry	Stainless steel tube $\varnothing$ 4.8 mm, l = 190 mm	Flexible stainless steel tube, $\varnothing$ 4.8 mm, l = 190 mm
Air Flow	Steady pipe flow, $U_\infty = 14$ m/s	Unsteady flow with pressure waves from air intake valve, $U_\infty \approx 14$ m/s
Gas Flow	HSV SP 051 injector	HSV SP 051 injector

The choice of air flow velocity in the experiments on the model was dictated by calculated intake stroke velocity for an engine running at 1800 rpm mode ($\approx$14m/s).

Experiments on a laboratory model were performed to provide information on the nature of gas jet mixing processes, and to help understand future experiments on the diesel engine.

3.2. Experimental Layout

To model the engine air-intake manifold geometry, a 400 mm long straight duct, made from a high surface quality transparent plastic with 50 mm inside diameter was used. A working section length of 300 mm was employed for mixing studies, to match the size limitations of real diesel engine manifolds. The geometries of diesel engine air intake manifold and model manifold used in the experiments shown in Figure 1.1.
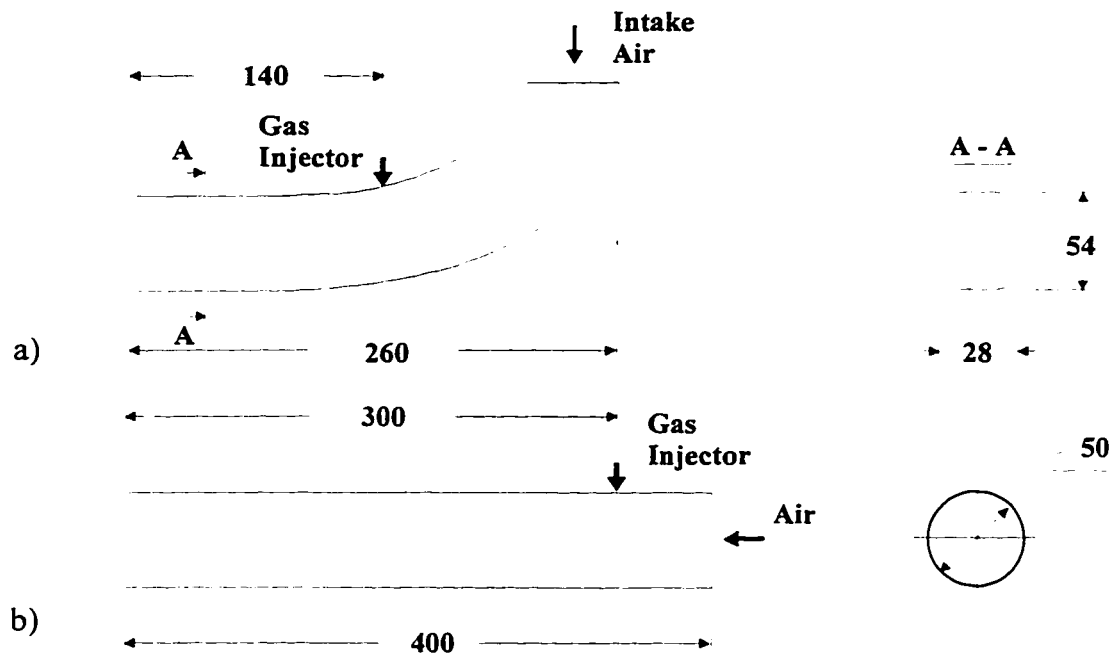
Figure 3-1. Schematic of a) diesel air intake manifold, b) model manifold. (Dimensions are given in mm).

The two ends of the model duct were equipped with flanges, so it was possible to add another module. The upstream end was connected to the orifice section of the model. This section contained two flow straighteners installed 8 diameters before and after an orifice plate according to the ASME recommendations. The downstream end of the test duct was attached to an instrument box, made of the same material as the tube. The instrument box served two purposes: to divert flow to the exhaust tube, and to support a probe positioning table.

Building compressed air, controlled by a pressure regulator, type WATTS-M, rated to 700 kPa, and a control flow valve, was used to supply the air flow in all tests.

To aid the process of concentration and velocity field measurement, a 3-D traverse mechanism was developed. It could position the probe at any space-point within the model test section, which was a specific requirement of the measurement procedure. The precision of this mechanism ± 0.5 mm in any dimension. The schematic of the sampling section with injector is shown in Figure 3-2.
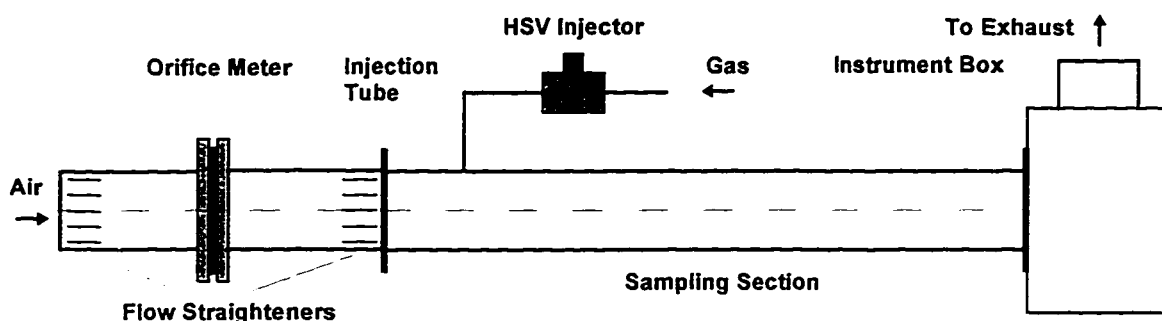
Figure 3-2. Schematic of sampling tube with injector.

The kind of gas jet having the greatest practical interest for this study is the single round axisymmetrical turbulent jet. In most experiments, the jet was discharged at right angles to the free-stream direction from a 190 mm long, 4.8 mm diameter stainless steel tube. The tip of the delivery tube was placed flush with the upper duct wall. The jet was supplied from a laboratory gas cylinder filled with a calibrated mixture of gases. This mixture consisted of 40% methane, 30% nitrogen and 30% helium by volume. The combined molecular weight of this gas mixture, $MW \approx 16$, was similar to that of natural gas, so that diffusion and buoyancy characteristics would be the similar to the natural gas. The composition was chosen so that the injected gas could be detected by an HC detector, but would not produce a flammable mixture with air.

An electrically operated High Speed Solenoid Valve (HSV), type SP-051, was used to control gas injection in the model. These valves are used in actual engine fuel systems. The HSV injectors have been designed so that choked flow occurs as the gas passes through them. With choked flow, the velocity of gas in the valve nozzle corresponds to the local speed of sound, $M = 1$, and by maintaining the exit pressure below the critical value, mass flow through the nozzle is unaffected by changes in the

outlet pressure. Capable of operating frequencies greater than 100 Hz, this type of injector is typically pulsed width modulated to meter the fuel quantity. The solenoid valve driver, type SD-1, and standard pulse generator was used to operate the HSV injectors in different modes.

3.3. Experimental Settings

Two types of JICF experiments were performed: steady gas flow injection and pulsed gas flow injection tests. For the steady gas flow experiments the solenoid valve was kept wide open, to allow continuous discharge of gas into the crossflow. In this case, the mass flow rate of injected gas was $m_{gas} = 0.327g/s$, based on the constant flow calibration curve for the HSV SP-051 at 20 psig gas supply pressure. The velocity of gas at the nozzle exit location was evaluated as $U_j = 30.5m/s$, according to:

$$U_j = \frac{\dot{m}_{gas}}{\rho_j A_{tube}} \qquad (3.1)$$

where $\rho_j = 0.604 kg/m^3$ at $P_{bar} = 700mmHg$ and $T_j = 298K$

$A_{tube} = 17.7 \cdot 10^{-6} m^2$ is area of the injector tube.

For the transient experiments, a 15 Hz injection rate was used to model the conditions of pulsed gas injection in a 4-stroke diesel engine running at 1800 rpm. The gas delivery for these experiments was calculated using the calibration curve for HSV SP 051 at 1034 kPa (150 psig) operating pressure and 11 ms solenoid energize time. Mass flow rate of gas delivered per one injection was $m_{inj} = 0.03g/inj$. At 15 injections per one second this gives 0.45 g/s of gas flow. The velocity at the exit of the gas delivery tube was estimated to be approximately $U_j = 260m/s$ based on the assumption that the gas flow is not choked at the exit.

The flow of air in the test duct was supplied from the laboratory's compressed air system and manually controlled by a medium-precision pressure regulator. Air mass flow rate for the steady gas flow conditions was $m_{air} = 12.9g/s$, and for transient experiments it was $m_{air} = 29.6g/s$, giving the typical dual-fuel engine mixture of 0.6 to

0.7 equivalence ratio. The average air velocity in steady gas flow tests was approximately $U_\infty = 6.0 m/s$, with Re = 2 * 10^4, based on 50-mm test section diameter and kinematic viscosity of air, $v = 15.5 \cdot 10^{-6} m^2/s$ at T = 24°C, and P_{bar} = 700 mm Hg.

For the transient gas flow tests the average air velocity was $U_\infty = 13.8 m/s$, with the corresponding Reynolds number of 4*10^4. The values of Reynolds number indicate a fully developed turbulent regime for the duct air flow in both situations. The momentum weighted jet velocity ratios were R = 4 for steady jet tests, and R = 14 for the transient jet tests. Correct ratios were achieved by adjusting the compressed air-line pressure regulator on the free-stream flow system while the keeping the gas supply pressure fixed at preset value.

3.4. Experimental Measurements

3.4.1. Selection of parameters

To make a complete picture of the jet mixing process, a full mapping of velocity, concentration and density parameters with their mean and fluctuating components would be required. As discussed above, there are two major regions of investigation of JICF: the near-field zone ($x/d < 20$) and the far-field zone ($x/d > 20$). This study is specifically devoted to the far-field region due to its emphasis on gas mixture formation for the engine. The parameters of the near-field region would be interesting to know, but due to the effects of jet impingement on the confining duct wall and high vorticity in this region, it was almost impossible to obtain reliable concentration measurements. Nevertheless, some assumptions, as discussed in Chapter 2, have been made about the nature of the flow in this zone and the effect it is having on the mixture development in the far-field region.

To ideally measure the mixing and distribution of jet mass in the duct flow, simultaneous measurements of gas concentration, density, and velocity would be required at many points across the duct. However, no probe exists to simultaneously measure all parameters at multiple points, therefore several simplifications were required. Guided by previous research in the field, the following measurement approach was used. Proof for the validity of this approach will be provided in Chapter 4.

Concentration was measured with a high frequency response detector which was moved sequentially to various points across the duct. For both continuous and pulsed jet experiments this requires steady operation of the duct flow. For the pulsed jet experiments, it provides ensemble averaged jet properties rather than multipoint measurements of a simple jet. Thus injection pulses are also required to be identical. Details of concentration measurement are provided in Section 3.4.2.

Density of the mixing gas and duct flows was calculated from ideal gas theory using averaged temperature and pressure values with the average gas composition at each point. In the far-field region, pressure fluctuations can easily be proven to be negligible and temperature fluctuations should be relatively small once the injected gas has been diluted to less than half its original concentration. Actual dilution levels were generally greater than two to one at the chosen measurement points. Details of gas density equation are provided in Section 3.4.3.

Velocity in the test duct was measured with a single Pitot-static probe which inherently measures the average velocity due to its low frequency response. This requires the same conditions of steady flow and repeatable injection pulses to give accurate multipoint measurements. In addition, the Pitot-static velocity measurement depends on knowledge of gas density. Different gas density assumptions were made for steady jet and for pulsating jet experiments. The details are presented in Section 3.4.4 and the results on velocity measurement are discussed in Chapter 4

3.4.2. FFID calibration and concentration measurement

To accurately measure the gas jet concentration field, a Fast Flame Ionization Detector (FFID) type CAMBUSTION HFR 400 was chosen as the major tool for this study. A detailed description of this detector may be found in recent papers on engine emission analysis (57, 58).

The FFID calibration includes numerous steps and it has some specifics for this kind of application. It is important to note that since an FFID produces an output which is proportional to the total mass flow of hydrocarbons, the instrument is sensitive to the volumetric sample flow rate and sample density as well as hydrocarbon concentration. Flow rate can be controlled by setting such parameters as FID chamber vacuum, constant

pressure (CP) chamber pressure, temperature, and sampling probe geometry. To observe mixing processes in the model, the CP chamber pressure was set well below atmospheric, and the pressure in the FID chamber was held at a lower level than the CP chamber. The pressure difference between the two chambers was held constant. It was necessary to determine operating pressures empirically to avoid flame out of the FFID and optimize instrument response. Table 3-2 provides a summary of instrument capabilities.

Table 3-2. Specifications for CAMBUSTION HFR 400.

Sensitivity	1 mV/ppm to 2μV/ppm in 9 ranges as C_3H_8 equivalent at an STP sample flow of 50 cc/min.
Precision	$\pm2\%$ ($\pm5\%$ for 200 V/μA, $\pm10\%$ for 500 V/μA).
Response time	90% of full scale in 1 ms with sample flow of 20 cc/min. and sample tube length of 50 mm (typically 3 ms with a standard constant pressure system fitted).
Ranges	500, 200, 100, 50, 20, 10, 5, 2, 1 V/μA. or respectively 2, 5, 10, 20, 50, 100, 200, 500, 1000 ppm lower limit.
Output Voltage	-10 V to +10 V
Fuel gas	Pure hydrogen at 75 - 100 psi gauge.
Air	Zero grade at 75 - 100 psi gauge.
Vacuum	4 psi absolute @ 1 liter/min. per channel used.
Sample	0 - 100 cc/min, determined by sample tube dimensions and vacuum level.
Ambient temperature	0 - 45°C.
Safety features	Flame out detection and automatic fuel shut off.

The techniques used to acquire data and determine sample system delay times are discussed in papers by Summers and Collings (59, 60). Differences between current experiments and the techniques described in these references consisted only of variation of sample line lengths and nominal FFID operating pressures. It should be noted that the probe geometry and the pressures must be selected according to the test conditions which are of interest. The "standard probe" supplied by the FFID manufacture could not reach all desired locations in the experimental setup. Therefore a different "long probe" was developed to meet the requirements of the tests. The longer transfer tube ("long probe") was ideal for sampling in the manifold model but required a higher mass flow rate and CP chamber vacuum to optimize instrument response. The values of selected pressures and probe geometries are shown in Table 3-3.

Table 3-3.   Set up of FFID for both geometries.

Parameters		Standard probe	Long probe
Transfer tube	length (mm)	323	585
	diameter (mm)	0.5	0.5
T-top	length (mm)	23	
	diameter (mm)	1.15	
FID tube	length (mm)	20	
	diameter (mm)	0.2	
CP chamber pressure (mm Hg)		-300	-335
FID chamber pressure (mm Hg)		-400	-435

The next step in the calibration procedure was to obtain a reliable calibration curve fit for the range of measured concentration. The static calibration was done first by using nine different concentration calibration gases. Calibration gas was injected continuously into a flowing air stream. The probe was placed in the gas jet and the output of the probe was digitized and recorded on a computer file. The HFR 400 gave a steady voltage output in the range 0 - 10 V during this procedure. Each sampling probe was calibrated in this way. The "long" probe was calibrated at the beginning of every experiment although it was not necessary to calibrate so often because of the high repeatability of the output characteristic of the instrument.

To calibrate the system at the same conditions as the test itself, the dynamic calibration technique was also used. In this calibration the special adapter was adopted to

reproduce both the pressure and temperature conditions present during the real test. This ensures that the calibration obtained is representative of the entire sampling system from sample tube tip to FID flame and indicates signal/pressure independence which is particularly important for fast measurements. It was necessary to adjust the span control to readjust the voltage output to a convenient value. After this final tuning, the FFID system was ready to use. The voltage output from the FFID instrument had a good linearity as is shown in Figure B-1, Appendix B.

To make sure that the "long probe" geometry could accurately measure gas concentration transient, more information on probe characteristics was needed. Since the time delay between the entrance of the sample in the probe and its arrival to the hydrogen flame is a function of the diameter, length, temperature and pressure settings for each tube, the transit time and time constant had to be evaluated for both transfer tubes.

The evaluation of time-constant parameter and transit time as characteristics of an FFID probe are important factors for data reliability. The time constant can be defined as the 10 - 90% response time of the FFID output for a step input at the source. The transit time is how long it takes a sample entering the probe tip to produce an electrical response.

In this investigation the "step" method was used to determined these parameters. The probe tip was placed in a jet of the span gas. By rapidly deflecting the probe out of the jet into adjacent air, it was possible to create a step change in FFID probe input. This procedure was repeated several times and the resulting data were analyzed to obtain measure probe characteristics. Figure 3-3 shows typical data for transient tests on the two probes and the real concentration measurement signal from pulsed jet test.

The time constant parameter (Tc) can be evaluated by applying Equation 3.2 or Equation 3.3 to experimental data from a step concentration change. Figure 3-3 shows the step change results plotted on a semi-logarithmic plot for ease in evaluating the time constant. It can be seen that:

$$1 - e^{T/T_c} = \frac{C_i - C_0}{C_f - C_0} \text{, or} \qquad (3.2)$$

38

$$T_c = \frac{-T}{\ln\left(\dfrac{C_f - C_i}{C_f - C_0}\right)} = \frac{1}{k} \tag{3.3}$$

where C_f - maximum value of measured concentration, %

C_0 - minimum value of measured concentration, %

C_i - measured point data concentration, %

T - time interval for $T_{90\%} - T_{10\%}$, and $T = X$ in fit equations in Figure 3-4

k - constant in fit equations in Figure 3-4.

Table 3-4 summarizes the estimate of response characteristics for the "standard" and "long" FFID probes and for the typical signal from the actual duct mixing pulsed jet test.

Table 3-4.   Results of evaluation of time-constant parameters.

Parameters	Standard probe	Long probe	Experimental Signal
Transit time (ms)	2.9	4.3	4.3
Time constant (ms)	1.02	1.57	2.37

From this Table it can be seen that the response characteristics of the "long probe" are quite close to the standard probe, and the time constant for the "experimental signal" (2.37 ms), is substantially higher than for the "long probe" (1.57 ms). These results imply that the "long probe" can be used in transient measurements with the same reliability as the standard probe.

The transit time parameter, shown in Table 3-4, was estimated for each tube by using a computer program known as "Sample Tube Flow Analysis Package" (SATFLAP3) which was supplied by the manufacturer of the FFID instrument (61). In this study the transit time was not important, since the distance between probe tip and FFID analyzing unit was quite short.
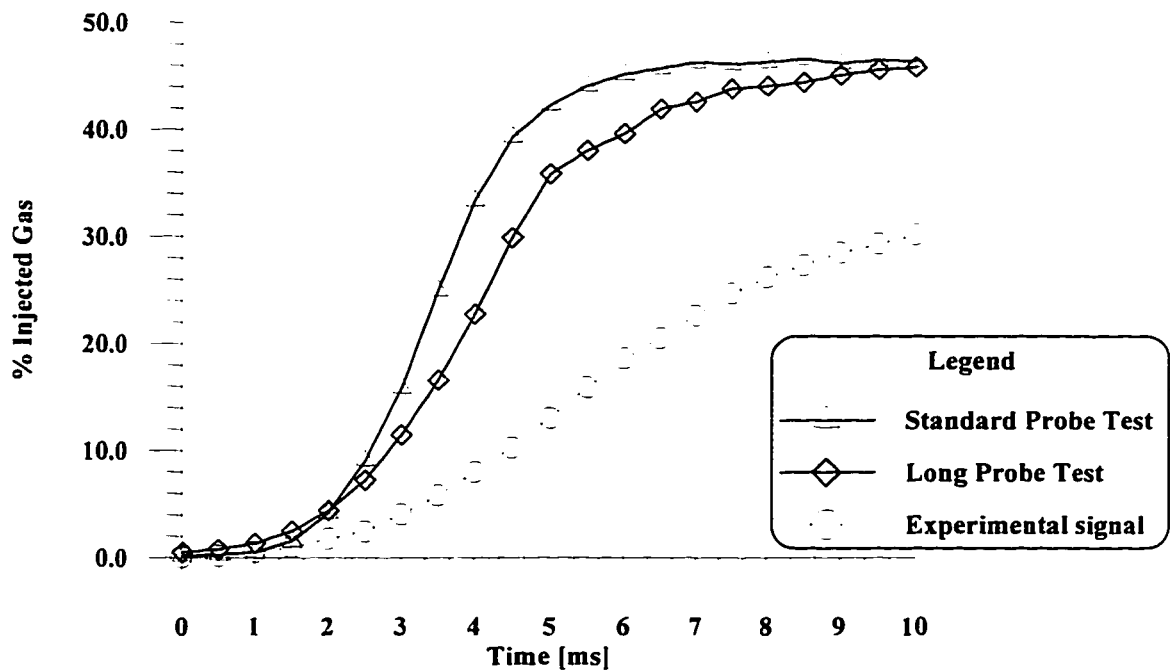
Figure 3-3. Experimental data for "step" method.
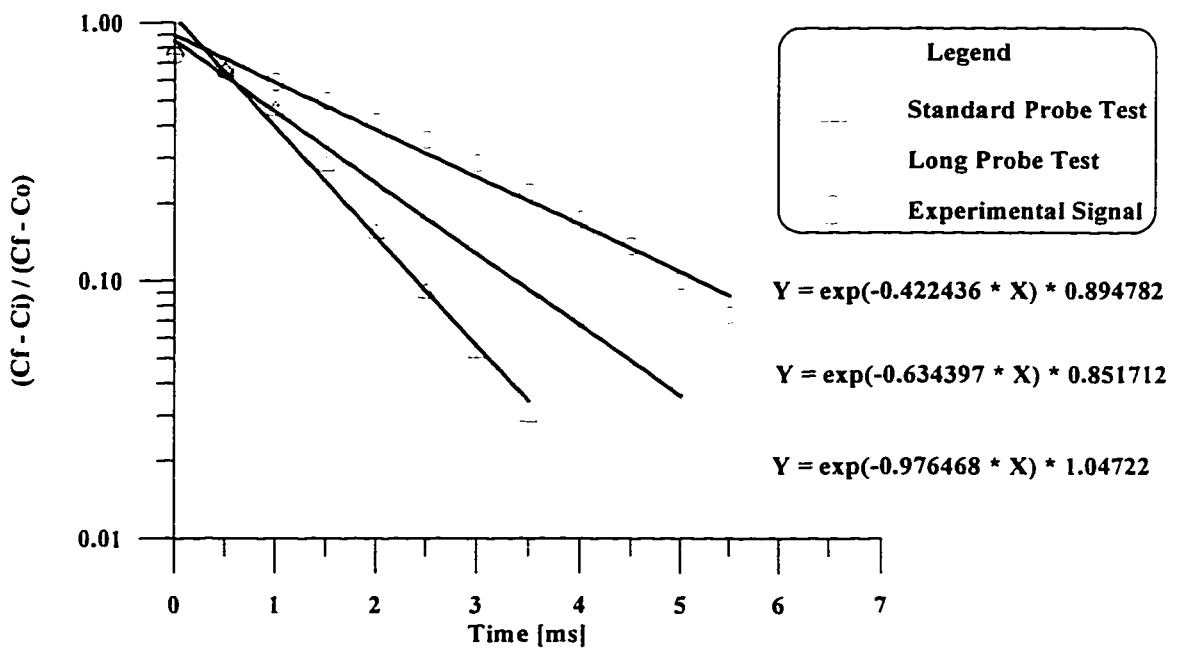
Figure 3-4. Semilogarithmic plot used for time constant (Tc) calculation.

40

3.4.3. Density evaluation

For the steady gas jet tests, the local density was first determined from the concentration field measurements. The mean value of velocity was then calculated directly from the dynamic head. Given concentration [X] (mole fraction), the density $[\rho_{mix}]$ of gas-air mixture in each measurement point is related by following equation:

$$\rho_{mix} = \rho_\infty(1 - X) + \rho_0 X \tag{3.4}$$

where ρ_o - the jet density at the jet exit, kg / m^3

ρ_∞ - the density of the duct flow, kg / m^3

X - mole fraction of jet gas in the mixture.

In the pulsed jet tests, the bulk density parameter of gas-air mixture for the far-field mixing region was calculated based on ideal gas law, and then used in velocity calculation. The density was obtained from the equation of state:

$$\rho_{mix} = \frac{P_{mix}}{RT_{mix}} \tag{3.5}$$

This approach can be explained by the following argument. In an axisymmetric jet with an initial density different from that of the ambient, density gradient decreases rapidly with downstream distance owing to the entrainment process. The flow approaches a state in which the density ratio between the local jet fluid and the ambient is near unity. Therefore, the assumption that density variations are unimportant, (except for buoyancy), can be applied to the far-field region of mixing.

3.4.4. Velocity measurement

A standard Pitot-static tube, with 3 mm outside diameter, was used to characterize the velocity field in the far-field region during the jet mixing experiments. The flow mean velocity $[\overline{U}]$ was sensed based on the Bernoulli principal:

$$\overline{U} = \sqrt{\frac{2\Delta P}{\rho_{mix}}} \tag{3.6}$$

41

The differential pressure measurement [ΔP] is proportional to fluid density and the square of the average velocity. All pressures were measured using a Validyne model CD 15, with type DP45-16 differential pressure transducer calibrated to 500 Pa. The calibration curve fit for that transducer is shown in Figure A-1, Appendix A.

In all the tests performed, the difference between stagnation temperatures of the two streams was insignificant, with maximum error of 1°C. Hence, the gas-air flow in the test section was considered to be isothermal. This assumption is important for the analysis of the mixing process, since it is excluding one of the important variables.

From the measurements of stagnation pressure, static pressure and stagnation temperature, the velocity was determined by applying standard gas dynamic procedure.

3.4.5. Mass flux evaluation

To characterize mixing in a duct flow, it was decided to use measurements of mass flux profiles across different duct cross section. Mass flux measurement combines individual measurements of concentration, density and velocity.

The total mass flux of gas across a given cross section of the duct can be calculated according to the formula:

$$\dot{m}_{gs} = \sum mf_{gs} \qquad (3.7)$$

where $\dot{m}_{gs}$ - total mass flux of gas in a given duct cross section, kg/s

mf_{gs} - mass flux of gas in a point of measurement, kg/s

Considering the measured values of concentration, density and velocity, the mass flux of gases in a given point of measurement in presented duct cross section can be evaluated by following equation:

$$mf_{gs} = \overline{U} \cdot \overline{C} \cdot \rho_{mix} \cdot A_p \cdot \gamma , \qquad (3.8)$$

$\overline{U}$ - mean velocity of gas-air mixture in a given measurement point, m/s

$\overline{C}$ - mean gas concentration in this point measurement, %

ρ_{mix} - density of mixture, kg / m^3

A_p - area of duct cross section represented by this point measurement, m^2

γ - density ratio, ρ_{gas} / ρ_{mix}

The density and velocity fluctuating components in these experiments were considered insignificant compared to the mean values of parameters since the time scale of the mixing process. Because of their small values they were ignored during the measurements. Consequently only mean values of density and velocity were used for mass flux analysis of the mixing process. The validity of this assumption was verified in each case by a continuity analysis. The continuity of gas mass was checked by comparing total mass flux at each duct cross section with the mass flow rate of injected gases.

3.4.6. Air flow control

To control the gas-air ratio in experiments, an orifice meter was installed in the upstream portion of the air duct. The parameters of the orifice were: 20.3 mm inside diameter, 50 mm pipe diameter. In conjunction with the orifice, a Valydine, type DP 15-20 with 14 kPa (2 psig) diaphragm, was employed for the air flow measurements. The orifice mass flow rate was calibrated against a standard laboratory orifice meter. The calibration curve fit used for the calculations is shown in Figure A-2, Appendix A.

To monitor the air-flow along with the fuel-air ratio, specially developed software, STEADY8.BAS, was used during the tests. As air mass flow rate depends on $[\rho_\infty]$ and thus on $[P_{bar}]$, the software had built in functions for ambient pressure and temperature adjustments. The functions of this software are described and listed in Appendix C.

3.4.7. Experimental set up

Data were recorded on a four-channel FM recorder, each channel having a bandwidth of 1 kHz which was found sufficient for this work. This assumption had been made on the basis that the FFID had a 300-500 Hz frequency response. The data were digitized and monitored with a Metrobyte DAS 16G analog-digital converter in a laboratory PC workstation. The processing and analyzing of recorded data used software

43

written specifically for these experiments. The names of these programs and their functions are described and listed in Appendix C.

Figure 3-5 gives an overall schematic of the experimental model and instrumentation.

1 - Sampling Tube 50 mm ID
2 - Injector
3 - HSV type Solenoid Valve
4 - Gas Flow Meter
5 - Gas Pressure Regulator
6 - Controller
7 - FFID Main Unit
8 - FFID Sampling Module
9 - FFID Probe

10 - Sampling Box
11 - 3-D Traverse Mechanism
12 - Flow Strainer
13 - Oriffice Meter
14 - Pressure Transducer
15 - PT Controller
16 - Manometer
17 - Air Pressure Regulator
18 - FFID Transfer Cable
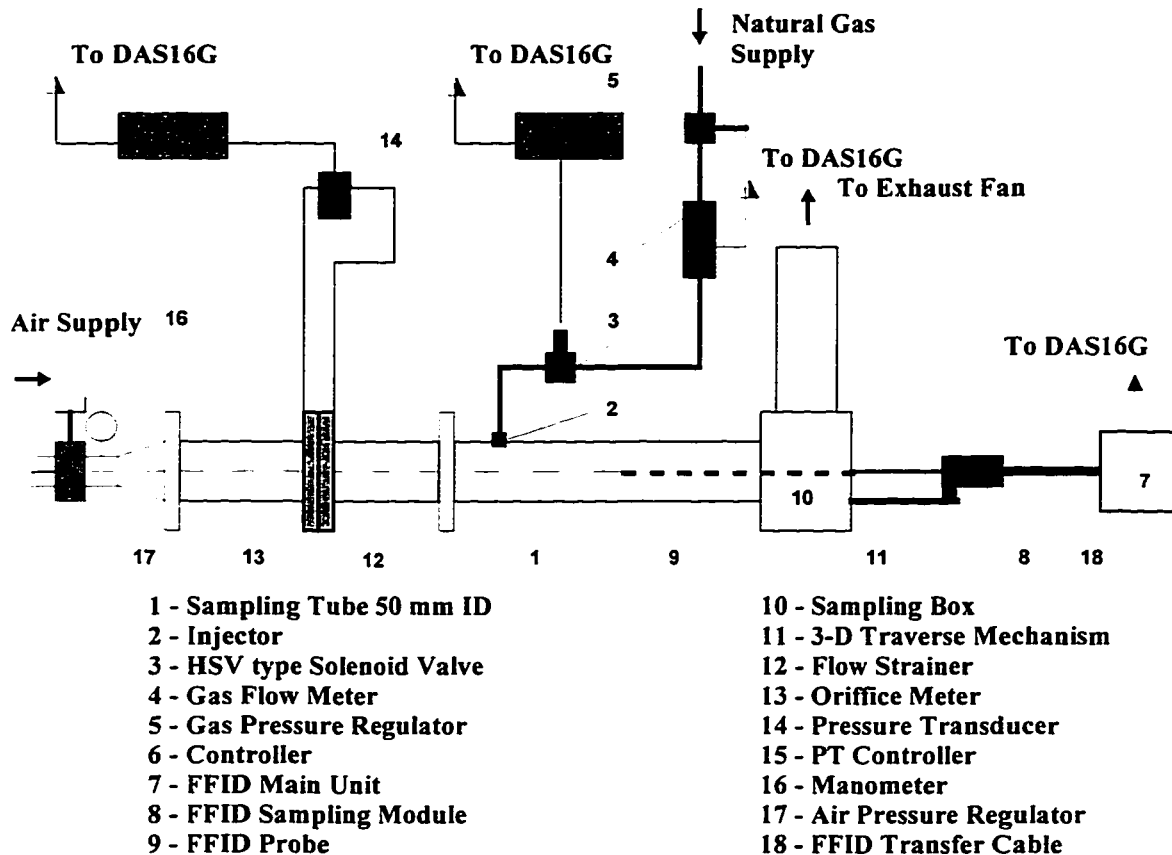
Figure 3-5. Schematic of experimental model.

3.5. Data Collection and Analysis

3.5.1. Experiments

Three sets of experiments were conducted for this study. An experimental investigation of steady continuous gas flow injection into the steady crossflow air-stream was performed first. With a gas supply pressure of 20 psig and velocity ratio R = 5, the injected gas produced a plume which was displaced by the cross-flow, and which slightly impinged on the duct wall. Measurements were taken in three cross sectional planes

downstream of the injection point, with nine points in each plane according to the measurement standard is shown in Figure 3-6a. The distances from the injection point were 145 mm, 215 mm and 285 mm, (respectively 30d, 45d, and 60d), as displayed in Figure 3-7. The purpose of this investigation was to test and refine the proposed measurement techniques for mixing processes in a ducted environment based on comparison with theoretical predictions of crossflow jet interaction. These experiments are described and the results analyzed in Chapter 4.

In the next series of experiments, the transient interaction of a pulsed gas jet with a crossflow air stream was studied under conditions similar to the real dual-fuel engine manifold. The gas injector geometry was chosen to be the same as in the engine manifold, with a nozzle exit flush with the wall. Two cross sectional planes, 30d and 60d from the injector, were used for data collection. The number and position of measurement points in each plane were set according to the AMCA 210-74 standard procedure for pipe flow measurements, which is shown in Figure 3-6b. During these tests the gas supply pressure was 1034 kPa, (150 psig), with velocity ratio R = 19, resulting in a strong gas jet impingement on the opposite wall. This investigation was planned to examine actual gas jet mixing as well as to establish proper measurement and data analysis methods for future experiments in dual fuel engine manifolds. The experiments are described and results analyzed in Chapter 5.

The last set of experiments dealt with pulsed gas jets in the same test conditions but using different gas injector tube geometries. The goal of this research was to find the impact of injector geometry on mixing in air-intake manifold conditions. The same method of data collection and analysis was applied to the results of this investigation. The tests and results are presented and analyzed in Chapter 6.

3.5.2. Data analysis

Steady Flow Gas Injection. The method of time averaging of concentration data has been used to analyze steady-state gas crossflow injection. The FFID output signal was recorded for 30 seconds and digitized at 2 kHz using the DAS 16G system. The resulting concentration-time data array was overall averaged using the Equation 3.9.

9 - Points Plane

0.021 D

0.45 D

D=50mm

a)

25 - Points Plane

0.021 D 0.117 D

0.184 D

0.345 D

D=50mm

b)   AMCA Standard 210-74
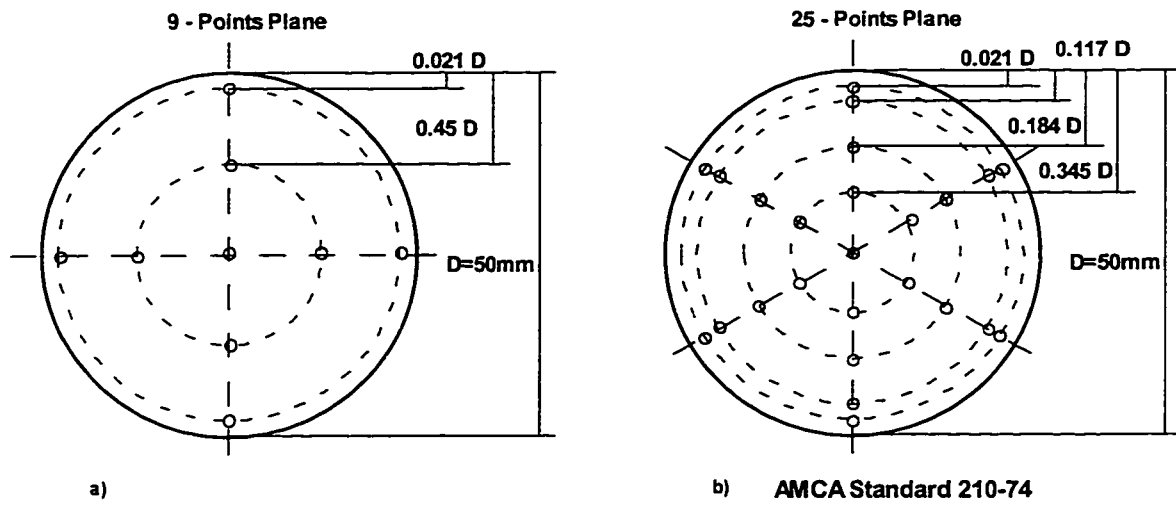
Figure 3-6. Measurement Locations used in experiments.

Natural Gas
Supply

Injectors

Plane 30d   Plane 45d   Plane 60d

Air
Supply

145 mm   70 mm   70 mm
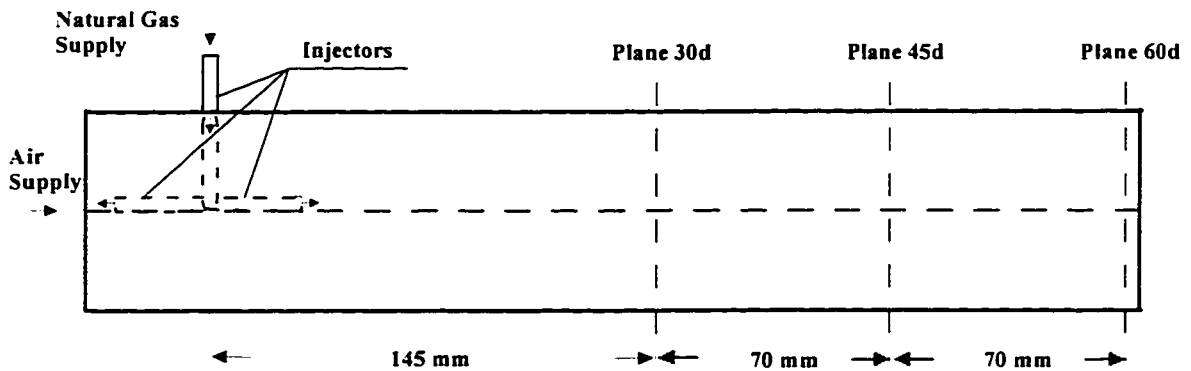
Figure 3-7. View of sampling tube with a Straight and L-type injectors

and cross sectional planes of measurements.

46

$$\overline{C} = \frac{\sum_{i=1}^{n} C_i}{n} \tag{3.9}$$

where $\overline{C}$ - the time averaged value (mean value) of local concentration, %

C_i - the instantaneous value of concentration, %

n   - the total number of data points taken during the time interval.

The mean concentration data were used to calculate mass flux distribution in gas-air mixture across each plane in the manifold duct to create a picture of jet interaction. Mass flux distribution of gas flow was evaluated according to Equation 3.8.

To check the accuracy of measurements, a continuity analysis was performed by comparing the value of combined mass flow rate of injected gas and air with results of calculation of total mass flux for gas-air mixture. That is, measured gas mass flux was evaluated using Equation 3.7 and compared with gas jet flow rate, $m_j = 0.327 g / s$.

Pulsed Flow Gas Injection. In transient experiments, an array of output signals from the FFID was obtained for every point measurement in duct cross section. Each pulse (the concentration-time curve) represented one gas injection. To proceed with analysis, ensemble averaging integration of area under this concentration-time curve was applied to measure gas mass flux distributions and rate of mixing. The formula used for calculation of gas mass contained in a given measurement point of duct cross section during one gas injection was as following:

$$mf_{gp} = \int_{i=1}^{T} C_i dt \cdot A_p \cdot \overline{U} \cdot \rho_{gas} \tag{3.9}$$

where mf_{gp} - gas mass flux per one gas injection in a given measurement point

of   duct cross section, kg/inj

T - the time period of injection, 67 ms

dt - the time step, 0.5 ms

ρ_{gas} - the mixture density, kg / m^3.

The continuity of gas mass was checked by comparing total gas mass flux at each cross section with the mass flow rate per one gas injection. The formula used in calculations of total gas mass flux per one injection [$\dot{m}_{gp}$] was as following:

$$\dot{m}_{gp} = \sum_{1}^{n} mf_{gp} \text{ , kg/inj} \tag{3.13}$$

The results of this calculation were employed to build the profile and contour maps of mixture formation in the manifold model.

3.5.3. Error analysis

The FFID output signal of 10 V was calibrated against 50% by volume or (500000 ppm) of methane. The FFID voltage resolution in concentration measurements was 0.01V, representing a methane concentration value of 0.0025% by volume or 25 ppm. This resolution was satisfactory for the measurements of mixing process in the model, since the FFID output voltage signal during the experiments was in a range of 0 - 3.2 V, making resolution approximately 0.03% of range.

The uncertainty in FFID voltage output is propagated in the calculation of mixture concentration. The calibration of FFID instrument confirmed that it had good linearity. Linear regression of the calibration data for the instrument had correlation coefficient greater than 0.999. Considering the calibration results, the uncertainty in the concentration measurements was estimated to be no greater than 260 ppm (0.05%).

The uncertainties in the FFID concentration measurements are also related to slight fluctuating of pressure in the sampling unit's constant pressure (CP) chamber due the rapidly started gas jet. It was felt that this pressure fluctuation could be ignored since the output from the FFID was stable and measurements were performed in the far-field from the injection point. The usual concern about repeatability of data was eliminated by routine calibration of instruments and careful examination of every data set.

The uncertainty in density calculation was affected by uncertainties in the ambient temperature measurements - 0.5°C (2%), in the ambient pressure measurements - 130 Pa (0.2%), and in concentration measurements - (0.05%). The uncertainty varies among the calculated values due to the different uncertainties involved and the different

conditions of the tests. The estimated uncertainty for the density calculation was no greater than 0.006 kg / m^3 (0.5%).

Physical errors in the measurements of dynamic pressures by using an orifice meter and Pitot-static tube were basically due to unsteadiness in both the pressure and velocities during the experiments. The mean velocity was measured with a calibrated five-hole pitotmeter. Spatial resolution of the Pitot meter was typically ± 1 mm. The uncertainty in measuring the velocity was estimated to be no greater than 5%. Measurement errors due to probe interference and the flow turbulence, and those due to velocity and pressure gradient in the flowfield were estimated to be within the range of the probe calibration errors and no attempt was made to correct for them. Flow perturbation due to these factors is difficult to quantify. However, as a check on the precision of the probe velocity measurements, the mass flow rate calculated by integrating across the measured axial velocity profile was compared with that measured directly by the orifice flowmeter: the discrepancy was always less than 5 %. For the given range of air flow 1 to 30 g/s the accuracy of the orifice meter was equal to 0.5 g/s which is 2% of the maximum flow rate.

The concentration, density and velocity values were used in calculation of mass flux distribution in the gas-air flow. Hence, the uncertainty in mass flux measurements is affected by uncertainties in these parameters. The estimated uncertainty in measuring the mass flux was no greater than 6%.

3.6. Chapter Summary

An experimental model was developed to investigate the mixing process of a natural gas jet in confined crossflow. To characterize mixing in a duct flow, measurements of mass flux profiles were made across different duct cross sections. Mass flux measurement combines individual measurements of concentration, density and velocity. The Cambustion HFR 400 FFID was chosen as a major tool to measure the mixture concentration fields. Density was calculated by ideal gas theory using average temperature and pressure values with the measured concentration. The velocity field profiles were achieved by using the Pitot meter technique. The measured data were collected using a computer data acquisition system during these experiments, and

analyzed using dedicated software to perform mass flow analysis. For the purpose of this study the rates of uncertainties in mass flow measurements were on acceptable level, less than 2%.

4. Testing the Measurement System: Steady Jet Flow

4.1. Test Method

To go on with experimental work, the reliability of the measurement system had to be tested. This was done by comparing measured results with analytic predictions for the best-characterized system: a steady, bent-over jet in cross flow.

To validate the measurement system for the future experiments with a pulsating gas jet, three parameters have been considered for measurements: concentration, density and velocity. The arrangement of these tests was discussed in Chapter 3 and the experimental conditions were as follows: the steady flow of gas at 138 kPa (20 psig) regulator pressure was injected into the test duct with mass flow rate of 0.327 g/s and exit velocity near 30 m/s. The crossflow air stream had mass flow rate of 12.9 g/s and average mean velocity 6 m/s, giving momentum weighted jet velocity ratio of R = 4. The experiments were carried on at the room temperature, 298 K.
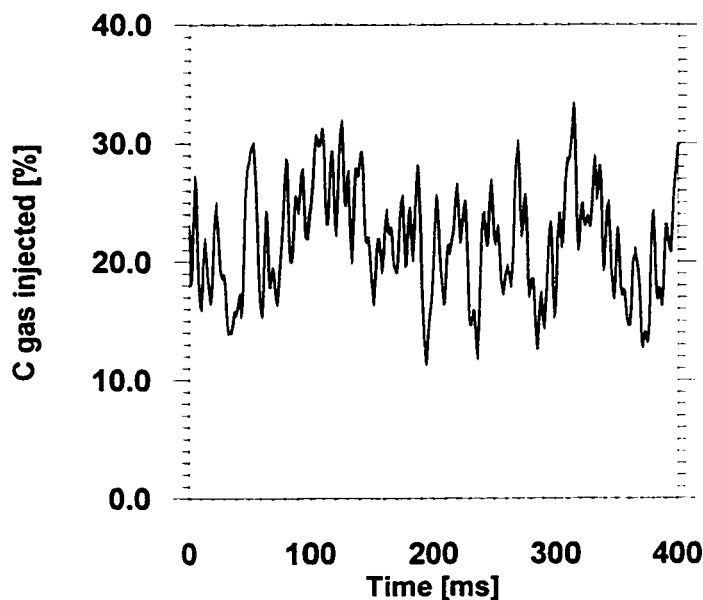
Figure 4-1. Typical profile of concentration data for steady gas flow tests (R = 4).

The gas mixture concentration field was measured at three cross-sectional planes using Cambustion HFR 400 FFID instrument with a 'long' sampling probe. For every

51

chosen probe position, the output signal from FFID was recorded during 30 seconds at 1 kHz sampling rate on one channel of Racal Store 4 FM tape recorder. The recorded signal was then digitized using Metrabyte DAS-16G data acquisition system for the signal data analysis. The typical digitized signal from FFID is shown in Figure 4-1.

4.2. Basic Test Results: Concentration, Density and Velocity

The concentration data for each position of the sampling probe at each cross-sectional plane was time averaged. The resulting values were processed with the 3-D mapping software SURFER 6 to obtain contour maps of mixture concentration as shown in Figure 4-2.

a) b) c)
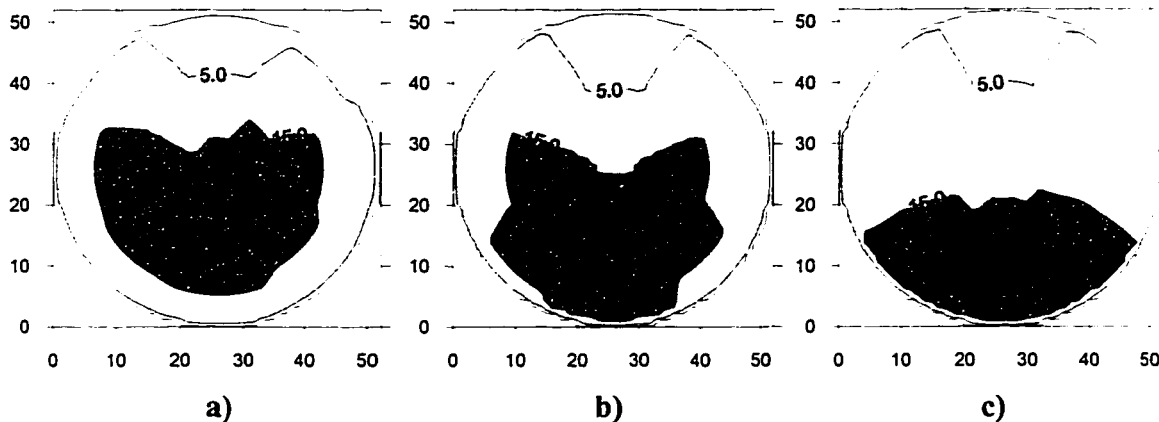
Figure 4-2. Contour maps of concentration data for steady gas jet injection
(R = 4): a) Plane 30d, b) Plane 45d, c) Plane 60d.
Contour values are jet gas concentration in %. Gas injector is at
the 12 o'clock (top) of the duct.

From these contour maps it can be seen that the injected gas has been diluted by air and distributed in different proportions at any given point of test tube. Based on the concentration data, the jet core is clearly located in the bottom half of the cross-section planes. This fact is in good agreement with theoretical projection of the jet's centerline path for the case of a jet in a crossflow environment.

The density distribution results are presented as contour maps on Figure 4-3. (To produce these maps, a triangulation grid technique was used in Surfer 6).
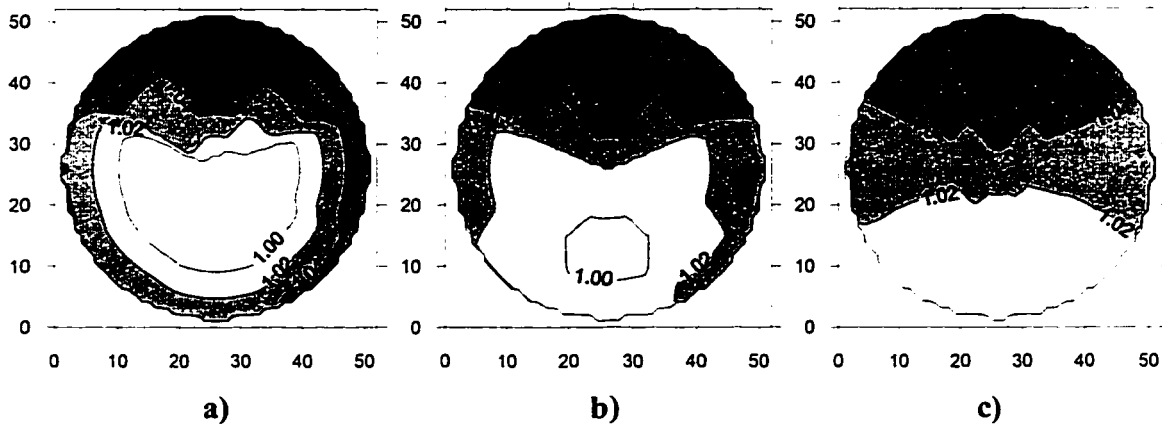
Figure 4-3. Contour maps of density variation [kg / m^3] for gas-air mixture (R = 4): a) Plane 30d, b) Plane 45d, c) Plane 60d.

To calculate density distribution for gas-air mixture, the measured values of mixture concentration were used in Equation 3.4 with values: $\rho_0 = 0.604kg / m^3$, $\rho_\infty = 1.093kg / m^3$.

To compute the velocity parameters, the measured values of dynamic pressure for injected gas and air were used in analysis. The flow velocity was sensed based on the Bernoulli principal, (Equation 3.6). The velocity pressure measurements (ΔP) were obtained for two conditions: pipe flow of air stream only and the combined flow of injected gas and air. In the former case, the value of ambient air density, $\rho = 1.091$ kg/m3, was used for computation. For the case of gas-air flow, the previously measured concentration values were used to give local density for each velocity calculation.

The velocity distribution of the two flows has been compared to see how different they are. There are two reasons for doing this. One is that application of a uniform velocity profile of air stream can simplify the mass flux analysis. The second reason is to use this assumption in the future data analysis of transient experiments.

53

The measured air velocities for the air stream flow (without gas injection), are shown in Figure 4-4, and velocity distributions for gas-air flow are shown in Figure 4-5. Again, the plotting was done in the form of contour maps.
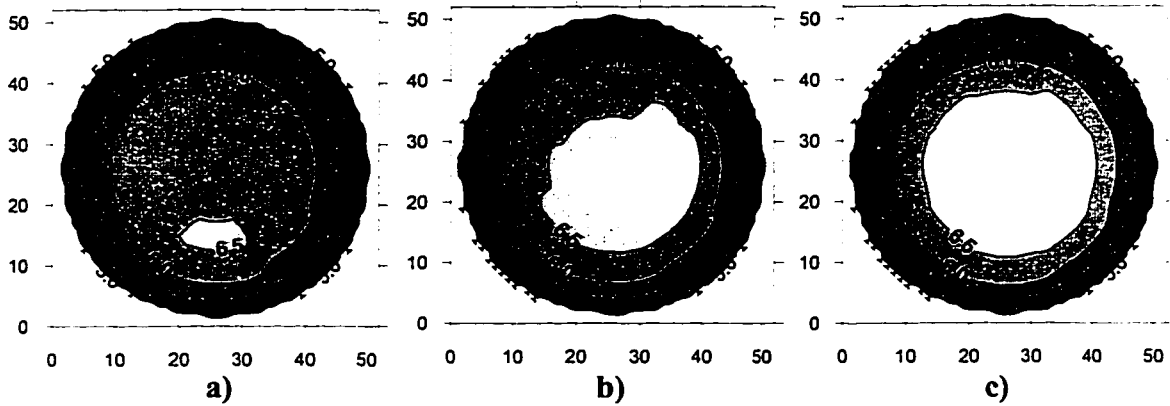
**Figure 4-4.   Contour maps of velocity data [m/s] for air stream flow only:
a) Plane 30d, b) Plane 45d, c) Plane 60d.**
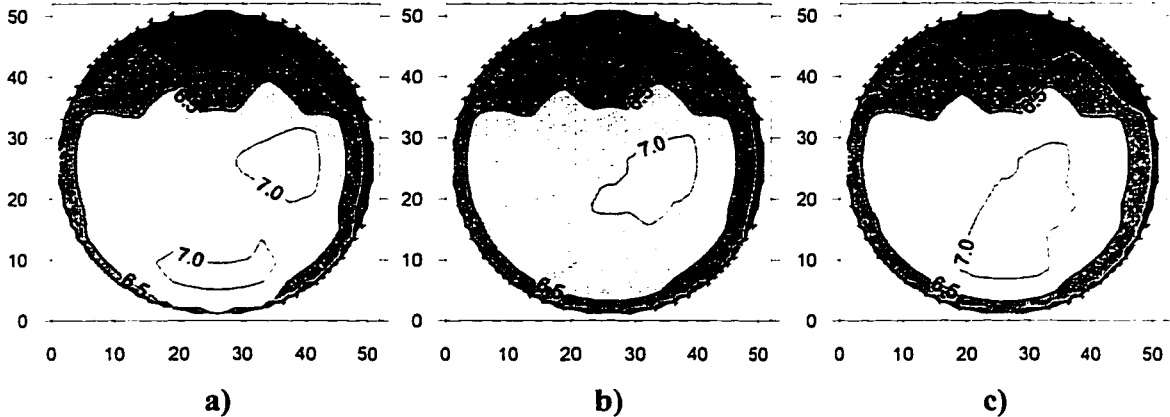
**Figure 4-5.   Contour maps of velocity data [m/s] for gas-air mixture flow
(R = 4): a) Plane 30d, b) Plane 45d, c) Plane 60d.**

By comparing these figures it can be concluded that mean density and velocity fields are about 10% different from the air-only flow when a steady gas flow is injected. This result supports the assumption that uniform velocity profile of air stream can be used only for the first rough estimation of gas-air mixture in current experimental analysis.

4.3. Comparison of Mass Flux Measurements

The mass flux distributions at three transverse cross sections downstream of injector, as calculated using Equation 3.8, are presented in the next two figures. Figure 4-6 displays the gas mass flux distribution calculated by using the air flow velocity profile. Figure 4-7 shows the gas mass flux distribution of the mixture computed using the gas-air velocity profile (with gas injected). Both mass fluxes are given in terms of the duct cross sectional area, (0.00197 m^2).
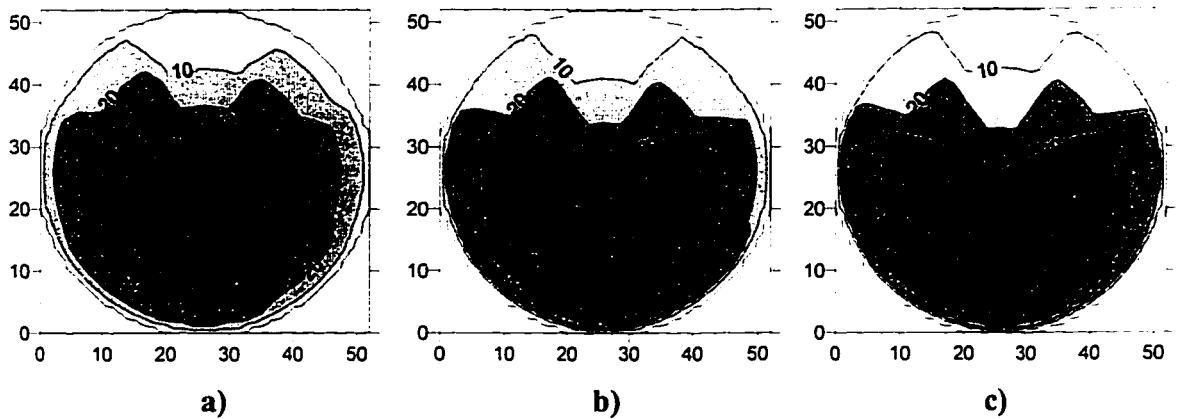
Figure 4-6. Gas mass flux distribution [mg/s/ 0.00197 m^2] using air velocity profile (R = 4): a) Plane 30d, b) Plan 45d, c) Plane 60d for gas-air mixture.
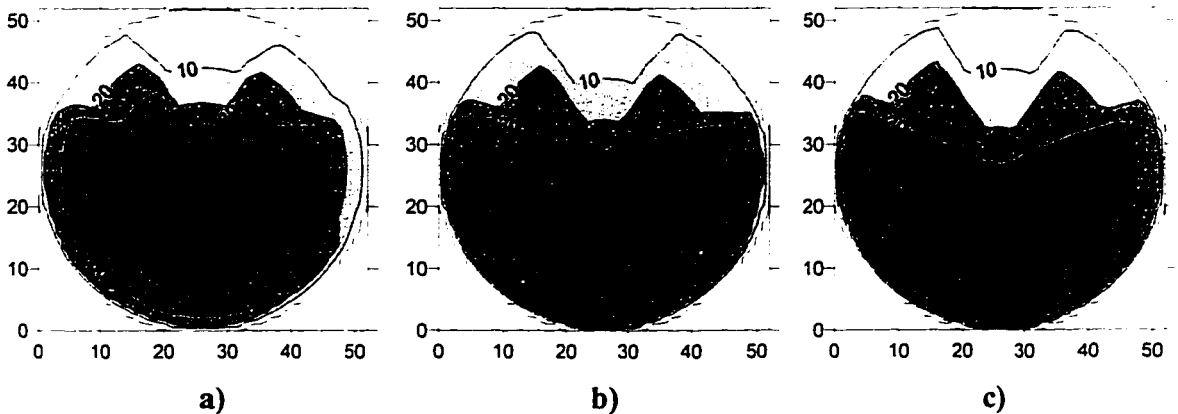
Figure 4-7. Gas mass flux distribution [mg/s/ 0.00197 m^2] using gas-air velocity profile (R = 4): a) Plane 30d, b) Plan 45d, c) Plane 60d for gas-air mixture.

The values of injected gas mass flux vary only slightly depending on which velocity profile is used. This observation partially justifies using the air velocity profile in calculating the mass flux distribution.

To better determine the optimum method of measuring gas mass flux, a continuity analysis was used. The measured gas injection flow rate was compared to the mass flow rate determined by integrating mass flux across the test duct. Either the air-only flow profile or the gas-air profile was used in calculating mass flux. The summary of results from these analyses is presented in Table 4-1. Table values are gas mass flow in [milligrams/second] and percentage difference from gas jet mass flow.

Table 4-1.   Summary of continuity analysis for steady flow experiments.

Method of analysis	Plane 30d [mg/s %error]	Plane 45d [mg/s %error]	Plane 60d [mg/s %error]	Average [mg/s %error]
Measured gas jet flow	327	327	327	327
With gas-air velocity profile	356 +8.8%	327 0%	314 -4.0%	332 +1.5%
With air velocity profile	323 -1.2%	299 -8.5%	289 -11.6%	304 -7.1%

The results from this continuity analysis on experimental data show that using the gas-air velocity profile to calculate gas mass flux provides more consistent agreement with measured gas flow values than using the air-only velocity profile.

The combined picture of interaction of jet with crossflow can be now drawn by using calculated mass flux data from experimental measurements for three cross sectional planes of test tube. This imaginary picture of crossflow jet interaction in steady flow environment is shown in Figure 4-8. As can be seen on this picture, in the near-field zone the gas jet is deflected by the cross-flow. The jet penetration and jet spread for R = 4 were calculated using Equation 2.5 and Equation 2.6. The results of this evaluation

$(z = 17mm, w_y = 7mm$ for $x = 1$ mm), agreed very well with experimental data and suggested that the jet was bent over by the crossflow without impingement on the opposite wall. Further downstream, the entrainment process of air is taken place and jet is spreading at high rate.
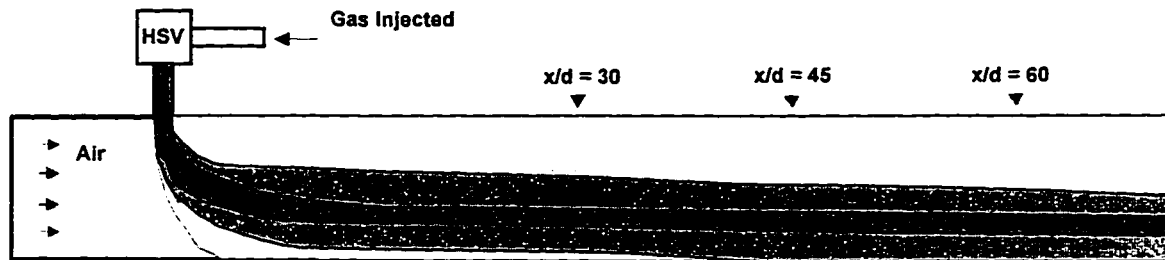
Figure 4-8. Experimentally predicted gas jet behavior for steady gas flow experiments (R = 4).

These near field features were confirmed by informal exploration with the FFID concentration probe. The observations are not presented in detail as this study concentrates on far-field mixedness. Finally, the mixing process is rapidly preceded in the far-field zone.

4.4 Assessment of the Measurement System

Considering analysis of the steady-state experiments, the following conclusions can be made. First, the FFID technique has proven useful and accurate in characterizing the mixture formation. Total mass flow rates across a test duct cross section agreed with gas injection flow rates to within 2%. While the air-only velocity profile can be used for rough estimation of mass flux distribution only, the combined gas-air flow must be used to achieve this accuracy. The observations from these experiments suggest that, in the far-field region, the jet path of injected gas can not be clearly detected due to the high degree of mixing and the effects the wall.

In view of this performance, the measurement system can be confidently applied to measure gas concentration. However, it is clearly critical to measure the density and velocity of the flow under actual conditions rather than rely on the air-only values.

5. Experimental Results for Pulsed Gas Injection

To interpret the mixing phenomena for pulsating gas injection into a cross-flowing air stream (freestream) it is essential to obtain information on concentration, density and velocity profiles of the combined gas-air flow. This was accomplished using the same measurement system that had been tested in steady gas flow experiments.

5.1 Experimental Details

The details of experimental arrangement and the nozzle assembly for these tests were given in the Chapter 3, hence they will not be repeated here. The experiments were conducted with a freestream mass flow rate of 29.6 g/s and average velocity of 13.8 m/s. The pulsed flow of gas at 1000 kPa (150 psig) regulator pressure and 15 Hz injection rate had mass flow rate per injection of $m_{inj} = 0.03 g / inj$ and the exit velocity near 260 m/s, which gave a momentum weighted velocity ratio of R = 14. The mean temperatures of the jet and the freestream were kept constant at T = 298 K. The measurements were undertaken in lateral planes at downstream locations x/d of 30 and 60. At each designated probe position, the output signal from FFID instrument was recorded for 10 seconds on one channel of the FM tape recorder.

In these tests the velocity field of freestream and combined gas-air flows was measured using the Pitot tube pressure probe, for comparative analysis of gas mass flux calculation. Preliminary trials showed that the optimum sampling time for each mean pressure measurement was 15 seconds. This large timing was essential to achieve repeatable average pressure readings.

5.2 Concentration Measurements

The concentration data were obtained for two downstream cross-section planes of test duct: Plane 30d and Plane 60d. The typical digitized signal from the FFID instrument at one probe position is shown in Figure 5-1.

As can be seen from this Figure, the typical concentration profile consisted of independent pulses, on average around 125 pulses in a 10 second period. To continue with further analysis of this information, ensemble averaging was used to create an

average pulse data file. A library of these ensemble averaged pulse data files was used in the following analysis on mixing.
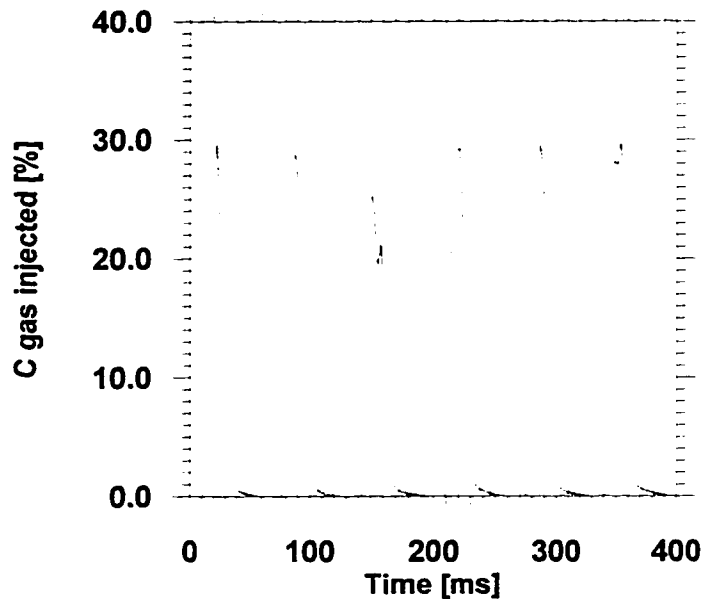
Figure 5-1 Sample of typical signal profile for concentration data in transient flow experiments, (Plane 30d, duct centerline, R = 14).

Initially, the peak concentration data points from average pulse data files were used to characterize the mixture formation in the far-field region. With the help of specially developed software and the SURFER6 plotting package, the results of this approach are visualized in Figure 5-2. Note that the labels on isocontours are shown in percentages of initial concentration of the injected gas.

From the distribution pattern of gas concentration shown on these pictures, the following can be concluded. In the lateral plane 30 jet diameters downstream from the nozzle, injected gas had been diluted unevenly by the freestream. The highest values of concentration appeared in the center of the top half of the test duct.

As the air-gas mixture travels further downstream, to the plane 60 jet diameters from the injection point, the structure of the peak concentration field becomes almost uniform, yet with higher concentration values in the top half of test duct. At this point, the injected gas has been diluted to one-fourth its initial concentration.
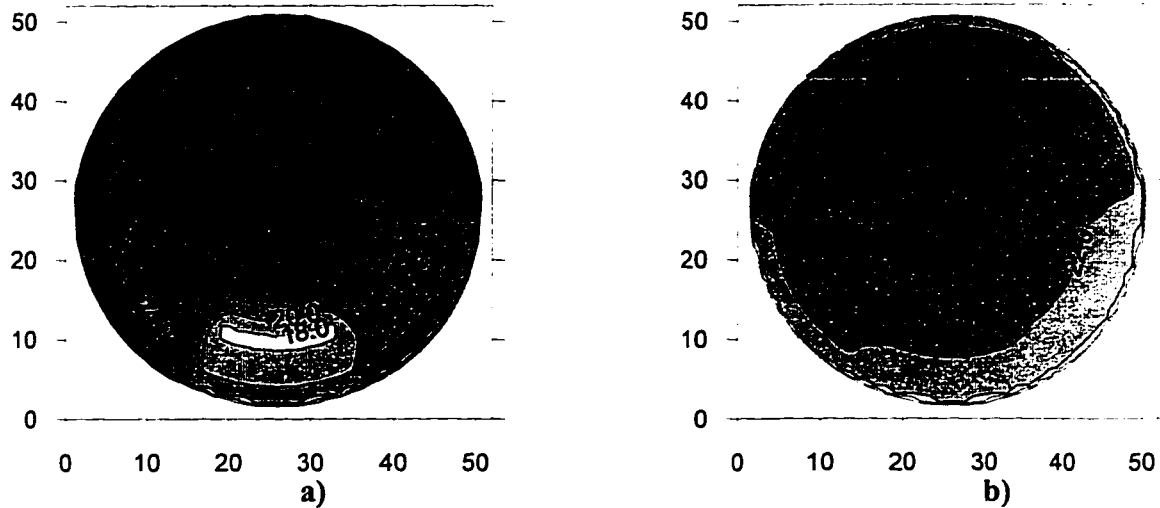
Figure 5-2. Contour maps of peak concentration data [% gas injected]
(R = 14) for: a) Plane 30d, b) Plane 60d.

These results are different from those obtained in steady gas injection experiments. The location of high concentration has been shifted to the top of the test duct. The only cause for this must be related to the higher velocity ratio along with pulsed gas flow, and likely associated with a different impingement outcome of the high speed gas jet on the opposite wall. To confirm these observations, further data analysis was needed.

5.3 Density Measurements

To calculate the air density, the ideal gas law was used for air-only flow, with resulting value of $\rho_\infty = 1.093 kg/m^3$, (Equation 3.5).

The bulk density parameter for the mixture in the far-field mixing region was calculated using mean values for temperature and pressure and local mean concentration for air-gas flow with gas injection, (Equation 3.6).

5.4 Velocity Measurements

The velocity profiles for the two planes have been calculated using the local density and velocity pressure measurements. For comparative analysis of the mass flux calculation method, the velocity profiles of both freestream air flow and combined gas-air

flow were measured. Contour maps of the velocity fields for both cases are presented on Figure 5-3 and Figure 5-4.
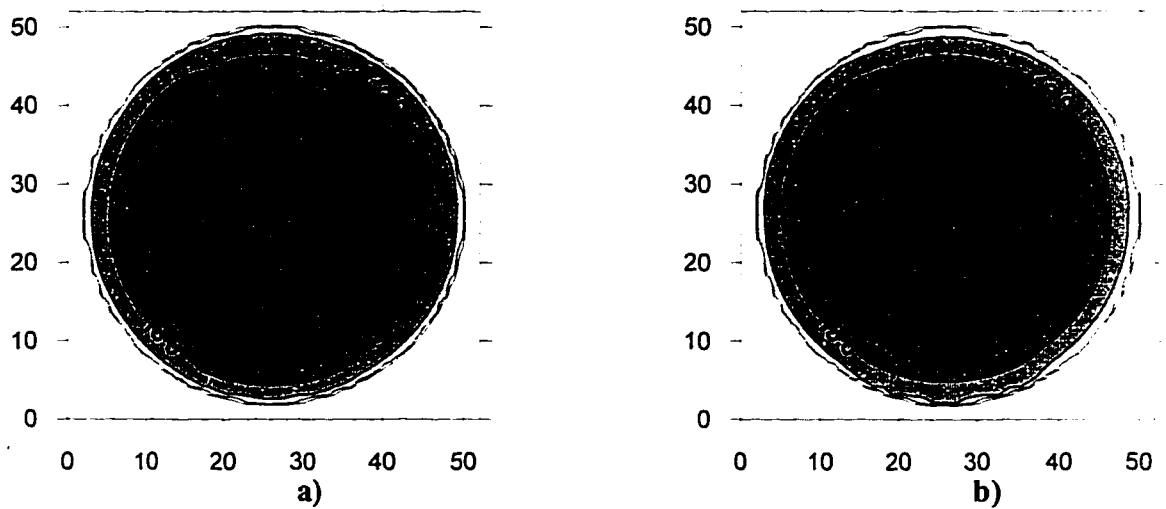
Figure 5-3. Contour maps for air-only velocity at: a) Plane 30d,
b) Plane 60d.
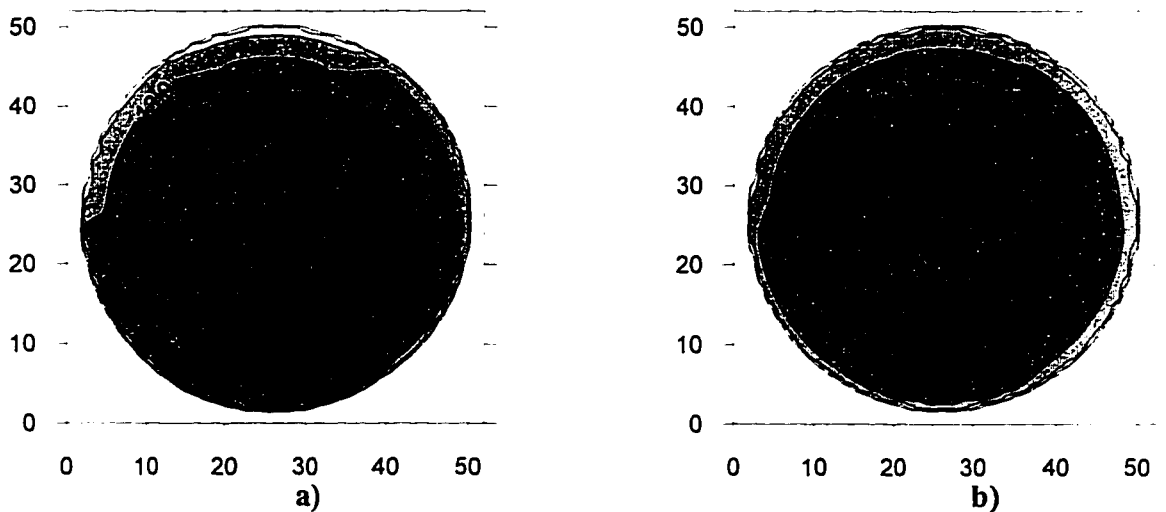
Figure 5-4. Contour maps for gas-air velocity (R = 14) at:
a) Plane 30d, b) Plane 60d.

According to these contour maps, the velocity fields for gas-air flow with pulsed injection are very similar to those of freestream flow. It appears that the effect of gas

61

injection is small over most of the flow profile but velocity changes from 12-13 m/s to 14-15 m/s in the lower central region. The increase (15%) in the velocity values at the bottom center of the test duct can be associated with a flow disturbance in this region.

There are a few possible interpretations of this fact. In the bottom center portion of the test duct the free-stream fluid was forced to accelerate around the obstruction caused by the jet which coincide with the wake recirculation. The contour plots of gas-air mean velocity and gas concentration confirm that the locus of the maximum velocity does not correspond to fluid from the jet exit; indeed, the downstream regions of high velocity are shown to be composed mainly of free-stream fluid.

The long time constant prevents detecting 11 millisecond bursts of velocity on the Pitot output. However, since the Pitot tube gives $\overline{E^2} \propto \overline{V^2}$, it is very sensitive to bursts and will be biased high in the region where bursts occur. This is another possible explanation for the increased velocity region in Figure 5-4a, bottom center.

The examination of Figure 5-3 and Figure 5-4 suggests that in the far-field region the aftereffect of gas jet injection on the velocity fields is notable and that the freestream velocity profile can be only used to make a rough estimation of mass flux distribution. The final proof whether the air-only velocity profile is adequate for pulsed gas injection measurements must come from the results of continuity analysis on the gas-air flow.

5.5 Continuity Analysis

The technique of integrating ensemble-averaged time-concentration pulses was applied to measure gas mass flux through each measurement plane. Application of this technique was discussed in Section 3.5.2 so it will be applied without further debate. As mentioned in Section 5.4, these calculations were made using either the air-only flow profile or the gas-air flow profile measured with gas injection. The cumulative results of these computations are presented in Table 5-1. and Table 5-2.

A few words must be said about structure of Table 5-1. The probe position column shows 25 positions of the sampling probe. These correspond to traverses on three axes. The vertical axis is represented by positions 10 → 17, and the two other axes, inclined at 60° to vertical, are denoted by positions 9 → 1 and 25 → 18 correspondingly.

Table 5-1. Results from calculation of mass flux [mg/inj] distribution for cross-flow gas injection.

Probe position	Plane 30d Gas mass flux		Plane 60d Gas mass flux	
	Air velocity profile	Gas-air velocity profile	Air velocity profile	Gas-air velocity profile
9	1.143	1.183	1.028	1.077
8	1.266	1.265	1.211	1.213
7	1.344	1.294	1.352	1.345
6	1.365	1.329	1.505	1.459
5 (center)	1.297	1.286	1.505	1.465
4	1.172	1.177	1.389	1.358
3	1.006	1.012	1.205	1.195
2	0.986	1.022	1.007	1.043
1	0.808	0.905	0.745	0.812
10 (top)	1.042	1.033	1.138	1.213
11	1.165	1.161	1.350	1.362
12	1.270	1.222	1.498	1.462
13	1.341	1.297	1.563	1.515
14	1.111	1.127	1.383	1.353
15	0.814	0.834	1.184	1.179
16	0.786	0.841	0.993	1.053
17 (bottom)	0.769	0.954	0.756	0.808
25	1.102	1.193	0.958	1.015
24	1.222	1.233	1.148	1.192
23	1.285	1.246	1.356	1.342
22	1.301	1.284	1.480	1.438
21	1.224	1.227	1.439	1.407
20	1.077	1.097	1.221	1.219
19	1.043	1.060	1.036	1.077
18	0.976	1.126	0.825	0.904

Table 5-2. Summary of mass flux [mg/inj] distribution statistics.

Actual mass injected is 29.9 mg/injection.

Parameters	Plane 30d Gas mass flux		Plane 60d Gas mass flux	
	Air velocity profile	Gas-air velocity profile	Air velocity profile	Gas-air velocity profile
Total mass flux	27.916	28.409	30.273	30.506
Error value	-6.7%	-3.0%	+1.2%	+2%
Average value	1.117	1.136	1.211	1.220
Standard Deviation	0.184	0.145	0.244	0.206
Minimum value	0.769	0.834	0.745	0.808
Maximum value	1.365	1.329	1.563	1.515

The locations of all probe positions, according to the AMCA Standard 210-74, are shown in Figure 5-5.
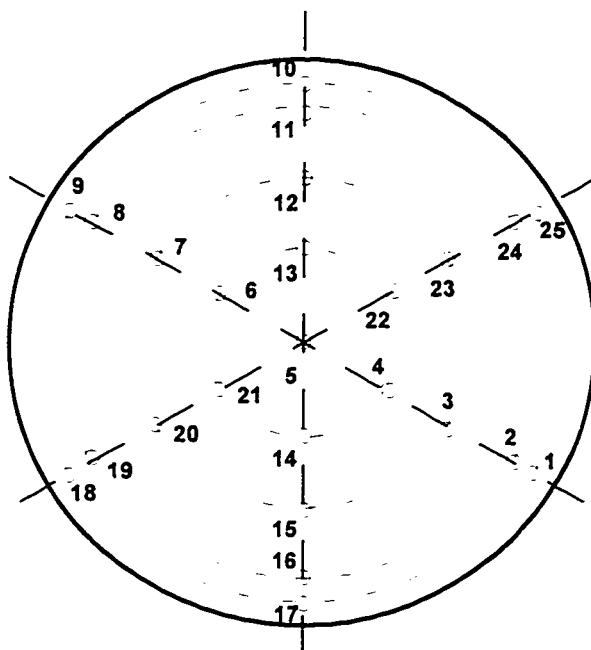
Figure 5-5. The layout of probe positions in lateral plane for transient tests.

Several useful observations can be made from Table 5-1 and Table 5-2. Comparing mass flux values in different cross-sectional planes for the two velocity profiles, slight differences can be noticed. These differences are concentrated at the probe positions in the lower part of the duct (1, 2, 16, 17, 18, 19). At other locations, the measured gas mass fluxes through each probe position generally fall within 1% of one another, whether using the air-only or the gas-air velocity profile in the mass flux calculation. The good agreement at these other locations gives confidence that the independently measured velocity profiles are accurate to ±1%.

The areas with significant differences in mass flux fall near the bottom of the tube where there is the strongest likelihood of both velocity and density pulses interfering with measurement accuracy. In these areas, using the gas-air density and velocity profiles always produces a significantly higher mass flux than was calculated using the air-only velocity profiles. The discrepancy is as high as 19% at the 30d plane and 9% at the 60d plane.

By integrating over the duct cross section area, a measure of total injected gas flow can be made. Comparison with the actual gas flow through the SP 051 injector is used to indicate the most accurate measurement method. For these conditions, the SP 051 would inject 29.9 mg of gas per injection. The integrated mass flux measurements fell quite close to this value, as shown in Table 5-2. At the plane 30 diameters downstream of the injection point, the measured mass flux was consistently lower than the amount of gas injected: by 3% if the gas-air velocity profile was used and by 6.7 % if the air-only velocity profile was used. The discrepancy indicates that there are significant combined effects of pulsating velocity, density and concentration which do not cancel out on average. However, the error is reduced to an acceptable level (3%) when using the measured gas-air velocity profile rather than the air-only profile.

At the second measurement plane, 60 diameters downstream of the injection point, the discrepancies between actual gas injection quantity and integrated gas mass flux were small, (less than 2%), regardless of which velocity profile was used. This agreement is taken to indicate that the errors due to pulsation were small when measurements were made 60 diameters downstream of the impinging jet.

The distribution of mass flux is shown graphically in Figures 5-6 and Figure 5-7. Figure 5-6 shows mass flux distribution as calculated using the air-only velocity profile, while Figure 5-7 shows the mass flux distribution calculated using the more appropriate gas-air velocity profile. Both approaches give a similar picture of the distribution of mass flux at the two cross sections. The distribution is asymmetric with the highest quantity of gas passing through the top part of the duct. Variation in mixedness is greater at the 30d cross section and decreases by 60d downstream.
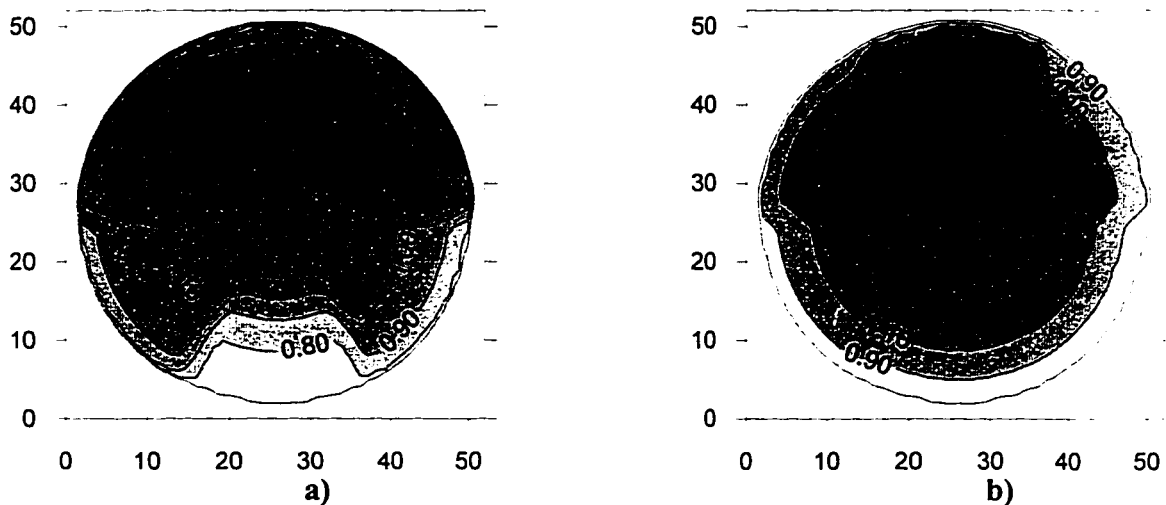
Figure 5-6. Mass flux distribution [mg/ing] (using air velocity profile, R = 14): a) Plane 30d, b) Plane 60d.
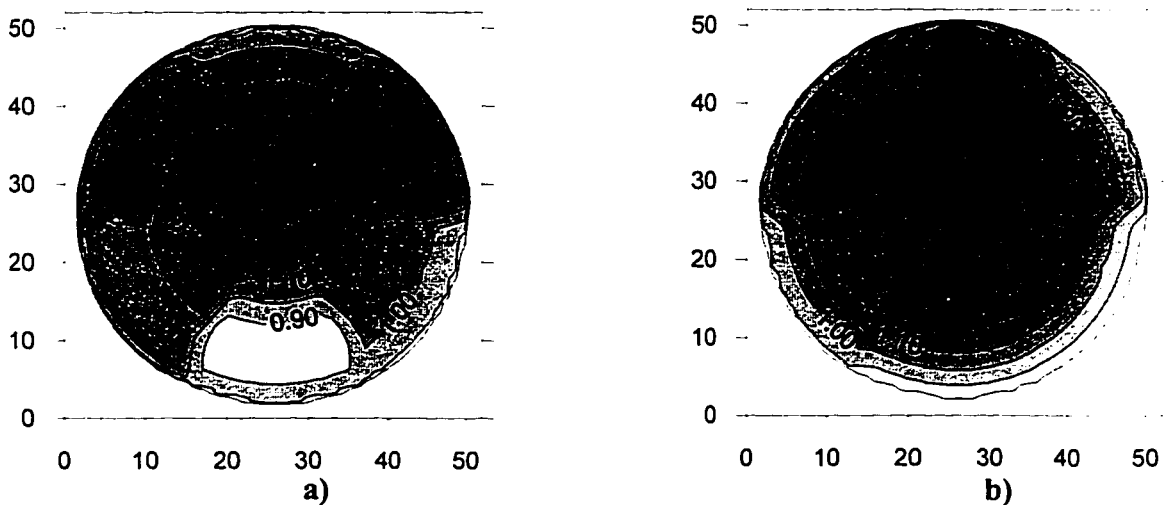
Figure 5-7. Mass flux distribution [mg/ing] (using gas-air velocity profile, R = 14): a) Plane 30d, b) Plane 60d.

When mass flux is calculated using the air-only velocity profile, the differences in mixedness are exaggerated compared with the calculation results using the gas-air velocity profile. The gradients in mixedness appear larger than is really the case due to ignoring the mean velocity changes associated with gas injection.

5.6 Analysis of Mixing Process

Statistical analyses on mass flux distribution through the test duct are useful for interpretation of the mixing process. Considering data presented in the Table 5-1 and in the graphical images of Figure 5-6 the mixing can be described as follows.

The pulsed gas injection into a cross-flow enclosed in a narrow duct creates an elaborate flow pattern due to the high velocity ratio $R = 14$ used in the transient experiments. A complex wall jet, that flows radially from the point of impingement along the surface, arises from impact of the high speed jet on the opposite wall of the duct. Cylindrical wall curvature of the manifold tube redistributes the injected gas in four major directions: upstream, downstream, and curving up the wall to the left and to the right from the impingement point, as is shown in Figure 5-8.
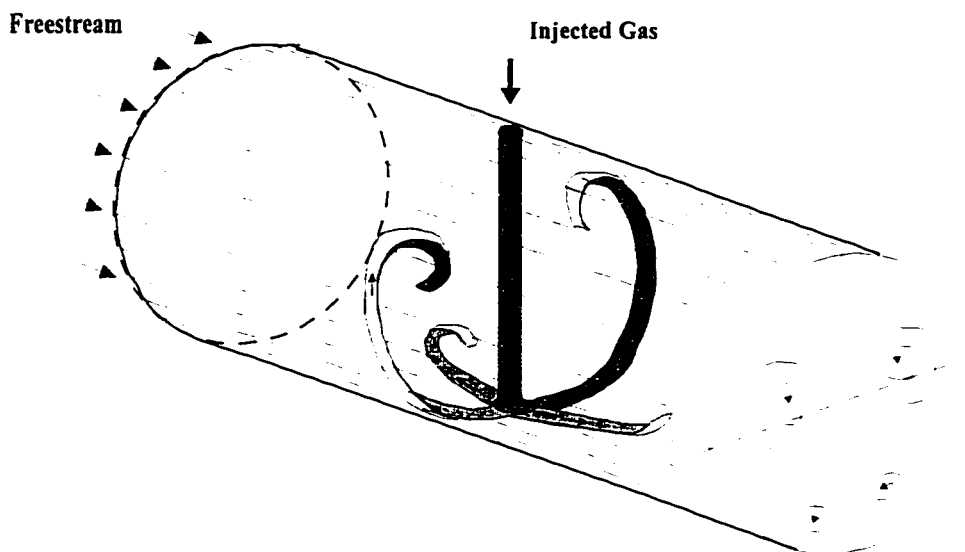
Figure 5-8. Redistribution of injected gas in a test duct.

The interaction of this wall jet with the free-stream results in the formation of a stagnation line and the creation of a separated flow area referred to as a ground vortex. Since the constant velocity cross-flow interacts with a radially distributed wall jet, this stagnation line is generally of the shape of the front half of an ellipse whose major axis is aligned with the free-stream flow, as shown in Figure 2-4. The locations of this stagnation line and of the center of the vortex region are dependent on jet to cross-flow velocity ratio, the height of the jet above the ground, and the injection angle of the jet into the free-stream.

The most prominent feature is the so-called upstream ground vortex. It is not a true vortex, but a turbulent separation bubble inside which the jet and cross-flow mix. The maximum penetration of the wall jet into the direction of the oncoming flow can be estimated using Equation 2.9: $(x_s - x_i) = 42mm(9d)$. The cross-flow was assumed to be inviscid.

For given R = 14 and 50 mm transit distance, the jet downstream displacement and jet width before impingement can be evaluated using Equation 2.5 and Equation 2.7 accordingly: x = 1.8 mm (0.37d), w_z = 24.3 mm (5d).

The final values of r_p and h_p can be estimated by adding the cross-flow factor in Equations 2.10 and 2.11 accordingly: r_p = 209 mm (43.5d), h_p = 18.7 mm (3.9d). The combined penetration distance ($x_s + r_p$) is equal to 251 mm (52d) which gives theoretical pulse width of $t_{pulse} = \dfrac{x_s + r_p}{U} \approx 18$ ms. That is almost 2 times less than the observed pulse width coming past the measurement plane in experiments. This result suggests that the theoretical approach in predicting the shape and the path of the impinging jet in crossflow underestimates these parameters.

The downstream portion of the wall jet acts to extend the forward penetration of gas into the cross-flow of air, whilst enhancing the process of mixing. The wall jet is also interacting with the cylindrical wall curvature and as a result creating a strong pair of side vortices. The appearance of these vortices led to a significant redistribution of gas flow and overall increase in the spreading rate of the jet. That also explains the presence of higher mass fluxes at the top half of the test duct.

The question of "how complete is the mixing at the end of sampling tube, just before gas-air mixture enters the air intake valve port", can be answered by comparing the measured mass flux distribution with the combustible limits of air-methane mixtures. Figure 5-9 shows the sample of gas mass flux redistribution according to combustible limits used in analysis. The results of this analysis are shown in Table 5-3 and Table 5-4.

The evident outcome from these analyses is that the fraction of the gas mass fluxes that is above or below the combustible limits changes only slightly for both planes of investigation, (though for the Plane 60d the variation between minimum and maximum values is smaller in each partition). Across the plane at 30d downstream, an average of 5.4% (± 0.8%) of the mass flux is "over-mixed" to below the flammable limit. Another 25.8% (± 16%) of the mass flux is within the flammable range. By the time the gas pulse crosses the Plane 60d, these numbers have only shifted to 6.0% (± 1.9%) and 25.4% (±5.8%) accordingly. This implies that almost all the mixing occurs in the near-field where the injected gas jet crosses the freestream flow and impinges on the wall, inducing vigorous turbulent mixing.
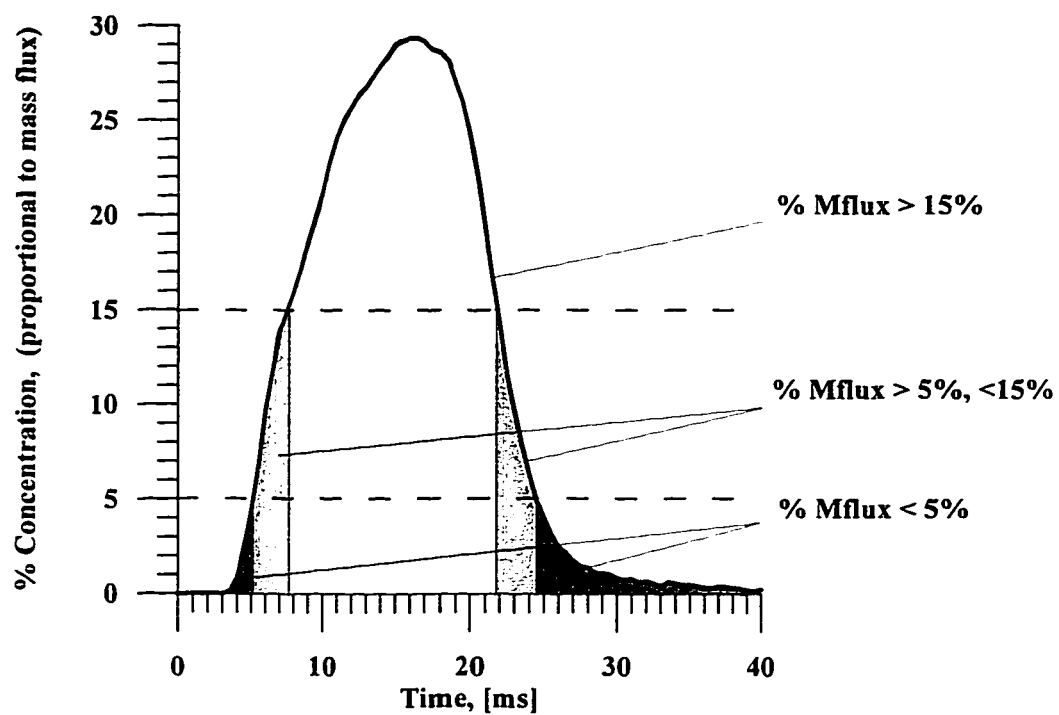
Figure 5-9. Sample of gas distribution on a mass flux pulse.
(Plane 30d, center of the duct).

Table 5-3. Gas mass flux distribution [% of total mass flux] in accordance with values of combustible limits for cross-flow injection.

	% Mass Flux Lean mixture (< 5%)		% Mass Flux Flammable mixture (5% - 15%)		% Mass Flux Rich mixture (> 15%)	
Probe position	Plane 30d	Plane 60d	Plane 30d	Plane 60d	Plane 30d	Plane 60d
9	5.08	8.40	15.01	27.64	80.15	63.96
8	4.36	7.24	16.41	25.47	79.23	67.56
7	4.68	5.41	15.84	23.97	79.48	70.88
6	4.60	4.31	15.60	18.90	79.80	76.79
5 (center)	4.56	4.53	24.13	15.04	71.31	80.43
4	5.39	4.68	31.44	17.66	63.17	77.66
3	5.26	5.09	38.95	24.85	55.79	70.36
2	5.88	6.75	28.03	30.55	66.09	63.02
1	5.61	9.82	26.48	36.00	67.91	54.18
10 (top)	5.88	6.47	14.17	28.06	80.21	65.23
11	5.45	5.21	12.81	28.67	81.74	66.11
12	5.72	4.19	13.35	25.35	80.93	70.23
13	5.21	4.14	17.45	20.00	77.34	75.86
14	5.68	4.19	33.44	17.02	60.88	78.80
15	7.42	4.89	79.48	22.63	13.54	72.48
16	7.39	5.90	67.39	26.89	25.22	67.54
17 (bottom)	6.50	9.77	40.07	33.83	53.43	56.39
25	4.79	8.55	16.88	32.48	78.34	58.69
24	5.11	6.72	16.67	33.61	78.23	59.66
23	4.89	4.45	16.85	31.41	78.26	64.14
21	4.86	4.01	30.00	19.30	65.43	76.69
22	4.80	4.13	14.40	19.42	80.80	76.46
20	5.56	5.85	16.99	22.51	77.78	71.93
19	4.70	6.58	22.88	26.96	72.41	66.46
18	5.08	9.70	20.62	27.42	74.29	62.54

Table 5-4. Summary of statistical analysis on gas mass flux distribution [% of total mass flux] for cross-flow injection.

Parameters	% Mass Flux (< 5%)		% Mass Flux (5% - 15%)		% Mass Flux (> 15%)	
Plane position	Plane 30d	Plane 60d	Plane 30d	Plane 60d	Plane 30d	Plane 60d
Average value	5.35	6.02	25.81	25.42	68.84	68.56
Standard Deviation	0.79	1.91	16.49	5.76	17.09	7.30
Minimum value	4.36	4.01	12.81	15.04	13.54	54.18
Maximum value	7.42	9.82	79.48	36.00	81.74	80.43

It is worthwhile to notice that the gas will mix further as it passes through the engine intake valve. Therefore, it is important to minimize the "over-mixed" (<5%) fraction of gas-air mixture while reducing C_{max} and conforming gas distribution across the duct. The gas-air mixture entering the cylinder becomes reasonably uniform with methane concentration within the combustible limits.

Another way to characterize mixture formation is to consider the time the injected gas takes to flow past a given point (probe position). This relates to the length of time the intake valve must be open (and exhaust valve closed) to capture all the injected gas mixture.

The information on pulse width can be viewed in Tables 5-5 and 5-6. At a point 30 diameters downstream from the injection point, the gas pulse duration has increased from 11 ms to 34.7 ms, a three-fold increase. The analytically calculated value of pulse width is about 20 ms. This widening of the gas injection pulse in experiments is primarily due to the high entrainment and jet spreading caused by cross-flow and impingement in the near-field region.

As the gas pulse progresses downstream to the 60d plane, the pulse continues to widen but at a much lower rate. The total pulse width increases from 34.7 ms to 37.6 ms, an 8% increase over a 10 ms ($x / \overline{U}$) transit period. This reduced rate of spread shows that the turbulent mixing continues in the intake duct but at a much lower rate than in the near-field.

Note however, that the pulse width is already excessive. A 4-stroke engine running at 1800 rpm has about 17 ms (one half revolution) for its intake stroke. Hence, the near-field mixing caused when the jet impinges on the wall has already made the pulse of gas too wide to be drawn in during a single intake stroke.

Table 5-5. Data on signal pulse duration for cross-flow injection mode. (Gas Injection Pulse = 11 ms).

Probe position	Signal Pulse Duration (milliseconds)	
	Plane 30d	Plane 60d
9	36.3	41.7
8	35.2	39.7
7	35.3	38.4
6	36.0	37.3
5 (center)	35.3	36.7
4	33.9	35.8
3	32.1	34.6
2	32.4	35.0
1	34.1	38.0
10 (top)	42.0	44.3
11	40.4	42.7
12	36.8	40.4
13	36.2	38.2
14	33.6	35.4
15	30.8	33.6
16	30.5	33.4
17 (bottom)	33.4	36.4
25	35.3	40.8
24	34.0	38.9
23	34.1	37.6
22	35.0	37.3
21	34.3	36.1
20	32.5	34.4
19	32.8	35.1
18	34.6	37.8

Table 5-6. Statistical analysis of signal pulse duration for cross-flow injection mode. (Gas Injection Pulse = 11 ms).

Parameters	Signal Pulse Duration (milliseconds)	
Plane position	Plane 30d	Plane 60d
Average value	34.670	37.591
Standard Deviation	2.546	2.827
Minimum value	30.470	33.370
Maximum value	41.960	44.330

5.7 Summary

The results of this investigation show that these techniques can be used to characterize mixture formation for pulsed gas injection. While the freestream velocity profile can be used for rough estimation, it appears more accurate to measure the actual profile. Results of this research illustrate that the high velocity ratio JICF in a narrow conduit creates a complex flow pattern with intense near-field mixing. Considering results of steady gas injection and pulse injection experiments, the location of maximum concentration highly depends on velocity ratio parameter and distance from the opposite wall of the enclosure. The shape of the manifold is also an important factor when impingement of jet occurs.

The data analysis has shown that by examining mass flux redistribution it is possible to characterize the mixing process in the far-field region. The analysis of mass flux distribution and data on pulse duration can be used in future work to characterize the mixture formation of JICF in closed environment.

6. Experimental Results for Different Methods of Injection

At this stage of the experimental work, the utility and capability of the system for mixture characterization had been proven. It was applied to measure concentration data for three different nozzle geometries injecting gas into a cross-flow. The idea of these experiments was to find out which injector geometry produced the best mixing results within a given length of manifold tube. That is an important issue for designers of gas injection systems used in dual-mode engines.

6.1. Test Procedure

The arrangements of these tests were the same as for the preceding set of experiments; hence the general descriptions can be found in Chapter 3. Reference to the experimental conditions of these tests can be found in Section 5.3. The three nozzle geometries tested and the lateral planes where measurements have been taken are shown in Figure 6-1. The injection tube was smoothly bent at 90° and extended to the center of the test duct. Two cross-sectional planes downstream from the injector nozzle tip were investigated: Plane 30d and Plane 60d. The layout of probe positions in lateral planes was adapted from the cross-flow experiments (Figure 5-5).

6.2. Analysis of Co-flow and Counterflow Jet Mixing

By applying mass flux analysis to the data collected, and using gas-air velocity profile in calculations, the data for examination of mixture formation were gathered. The summaries of this information are presented in Table 6-1 to Table 6-8. The data on cross-flow injection have shown a good repeatability, and consequently the Table 5-3 to Table 5-6 and Figure 5-7 can be used for reference. The contour maps of mass flux distribution in two lateral planes for co-flow, and counterflow injections were obtained as the results from these experiments. They are displayed in Figure 6-2. To better visualize mass flux redistribution in three modes of injection, 3-D plots were created using SURFER6 software. These surface maps, for Plane 30d and Plane 60d, are presented in Figure 6-3 and Figure 6-4 accordingly.

6.2.1. Co-flow (parallel flow) injection

The pulsed gas injection into co-flowing duct flow generates turbulent shear flow with possible occurrence of circulation zones. The nonuniformity of the velocity profile at the initial cross-section of the jet affects the shape of the edge of the boundary layer and the initial part of the jet. The nonuniformity of flow is caused by a two-dimensional wake, which forms behind the edge of the injector nozzle. This wake consists of two boundary layers and a circulating region which arises as a result of the separation of the flow by a nozzle wall (7). As the distance from the nozzle increases, the turbulence generated at the interface of two flows invades into the jet stream and the potential core of the jet is completely consumed. Considering the freestream, it loses a portion of its flow to the gas jet flow due to the entrainment process. If the velocity ratio is large, R = 14, an adverse pressure gradient is set up in the axial direction and the freestream is retarded. If the length of the duct is sufficiently large, the air flow can be completely consumed in this region. Beyond the end of this region, the flow decays gradually to fully developed pipe flow, if the duct is long enough. It is not the case in the current tests.

According to the conditions of this experiment, the calculated value of jet tip penetration is equal to 249 mm (52d), according to Equation 2.12. This result suggests that mixing is still in progress past beyond Plane 30d downstream of injection point. The observations from Tables 6-1 and 6-2 also support this fact.

The mixing analysis of the co-flow injection can be made using tabulated results from mass flux distribution in accordance with combustible limits. In the Plane 30d there is still a strong unevenness in mass flux values. The standard deviation numbers extend from 12.27% for Mflux (<5%) to 37.88% for Mflux (<15%) region of gas-air mixture. It can be seen that the largest concentration value is located in the central part of the test duct. Figures 6-2c and 6-3b display this observation very well.

At the second plane of measurement, Plane 60d, the deviation is much smaller. Hence, the mixing process is proceeding. The big percentage of Mflux (>15%) portion, 66.4% on average value, certainly confirms this fact. This can be seen on Figure 6-2d and Figure 6-4b.

6.2.2. Counterflow (opposite flow) injection

If a gas jet is directed upstream against a uniform flow, the jet will penetrate some distance into the oncoming flow and then be turned back upon itself and carried downstream. The degree of penetration could be expected to depend upon the diameter of the jet and the velocity ratio R. As the velocity ratio grows large, the flow becomes unstable, with significant fluctuations along both the downstream and radial directions.

The jet can be divided into two main regions: the near-field zone, where the jet or forward flow is dominant, and the far-field region, where the counter-flow dominates. In the far-field, the jet will be decelerated and deflected by the freestream, and, after reaching a stagnation point, the jet will reverse and gradually approach the velocity of the counterflow. The downstream distance (x_p) from the nozzle tip to the stagnation point is called the penetration depth. The mean penetration depth is directly proportional to the ratio between the jet and counterflow velocities. The maximum radial extent (y_p) or half-width of the jet flow is about 40% of the mean penetration depth (9):

$$\frac{x_p}{d} = 2.8R \qquad (6.2)$$

$$y_p = 0.4x_p \qquad (6.3)$$

The calculation shows that for given R = 14 and d = 4.8 mm, the mean penetration depth (x_p) is equal to 188 mm (39d) and maximum radial extent is equal to 75 mm (16d). These numbers suggest that the jet flow expands to the wall of the test duct and enhances the mixing process. In addition, the total distance traveled by the jet before it reached the Plane 30d was 521 mm (108d), which is also improved mixedness.

The information from Tables 6-3 and 6-4 validates this assumption. The data show evenly distributed mass flux with small standard deviation between values. The redistribution of mass flux among the three combustible limits regions presents clear evidence of continuation of mixing process between two cross-sectional planes. The values were shifted on average by 14% from high concentration region to the lower

concentration region, from Plane 30d to Plane 60d. The visual proof for that is in contour plots in Figure 6-2e,f and surface maps in Figures 6-3c and 6-4c.

6.3. Analysis of Mixing

Considering the data in Table 6-5 and Table 6-6, certain practical observations can be made. Comparison of experimental values of total gas mass flux with the actual gas flow through the SP 051 solenoid injector has shown the following.

The distribution of the mass flux among different points of the test duct is almost uniform using counterflow injection mode and most uneven using co-flow injection mode. The contour maps shown in Figure 6-2 confirmed the assumption that counterflow injection created an almost uniform concentration field in the test duct.

The integrated mass flux measurements fell quite close to the value of actual injected mass of gas for counterflow and cross-flow injection modes, (3.5% error on average). For the case of co-flow injection the error in mass flux calculation is large (25.3%) in Plane 30d and merely acceptable (8.4%) in Plane 60d downstream of injection point. These discrepancies can be explain by the following argument. The gas-air velocity profile used in calculation of gas mass flux was probably inappropriate due to lack of measurement accuracy in the co-flow injection mode. The end of the Pitot tube was exposed to the sudden big pressure changes caused by the direct exposure to the jet flow. These dynamic pressure bursts definitely affected the output signal from the probe since output is proportional to mean square of velocity.

The large error in the co-flow injection case illustrates the limitation of using the slow-response Pitot tube for these measurements. The correlated high gas concentration and high velocity pulse is not adequately measured due to the slow response of the velocity measurement system.

This is not a problem for measurements with cross-flow or counterflow injection modes since the velocity change during pulses is negligible. This fact should be accounted for in the future experiments. Aside from that, the measurement system proved to be reliable for analysis.

78

CROSS-FLOW INJECTION

GAS ↓

30d   45d   60d

d = 4.8 mm

AIR →

D = 50 mm

0   145 mm   215 mm   285 mm

PARALLEL FLOW INJECTION

GAS ↓

0d   30d   60d

AIR →

d

10d

OPPOSITE FLOW INJECTION

GAS ↓

0d   30d   60d

AIR →

d

10d
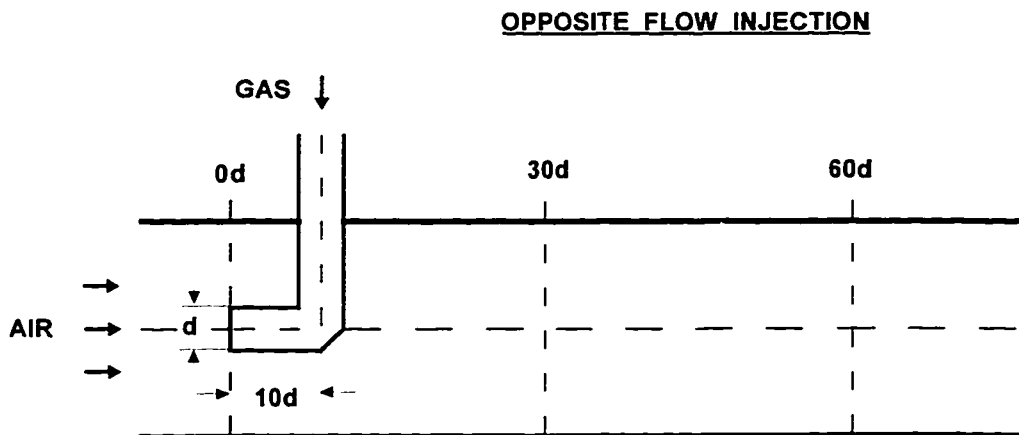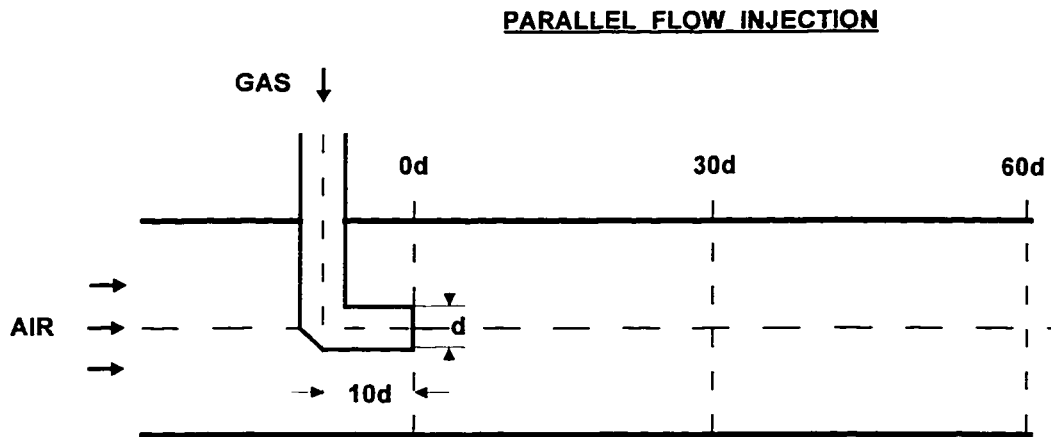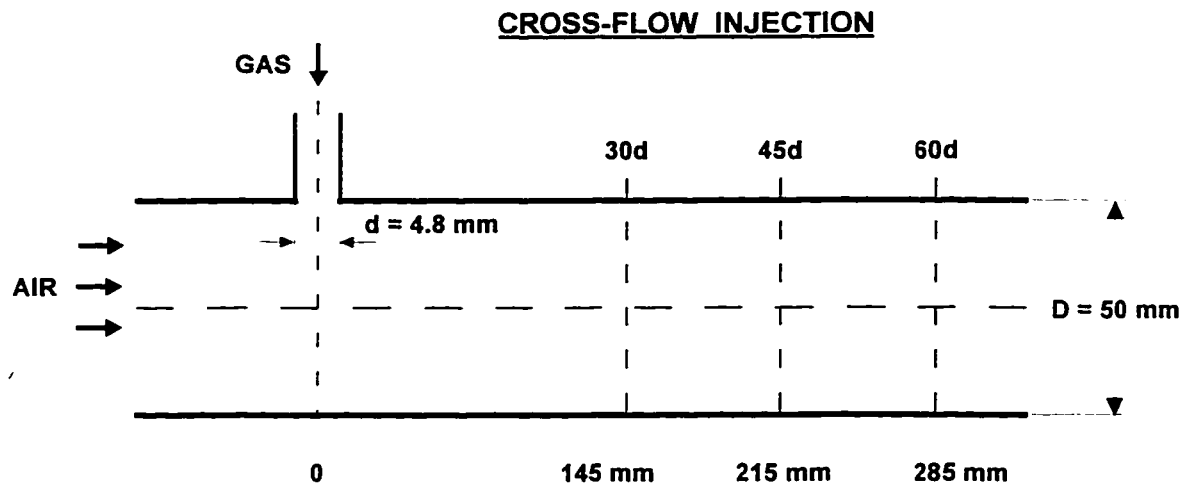
Figure 6-1. Schematic of three nozzle geometries for different injection modes.

79
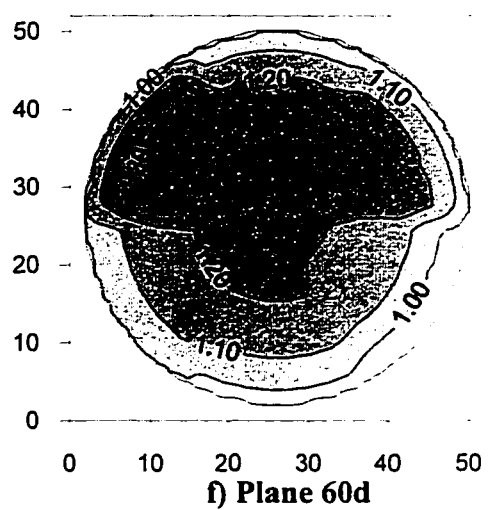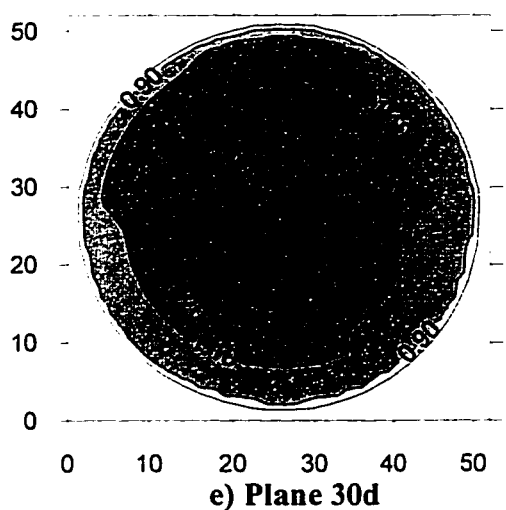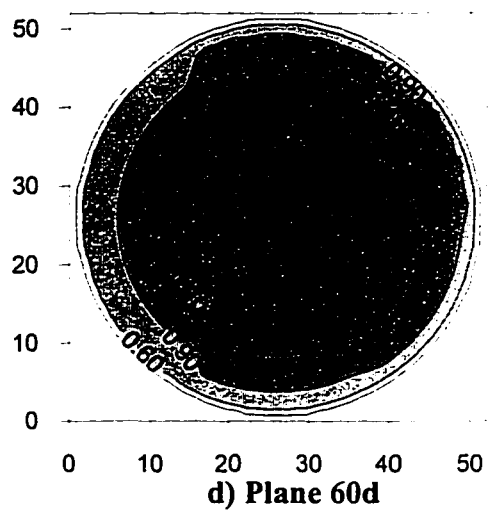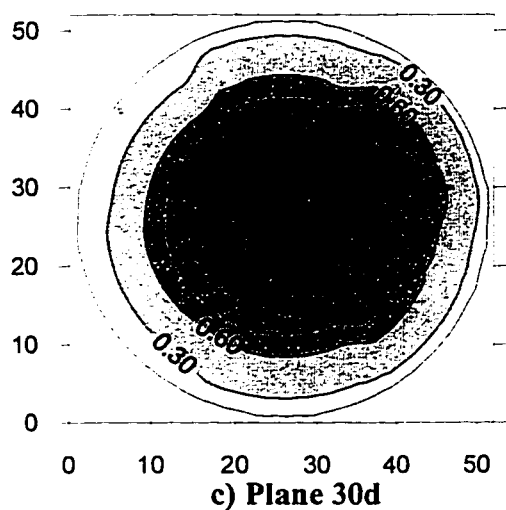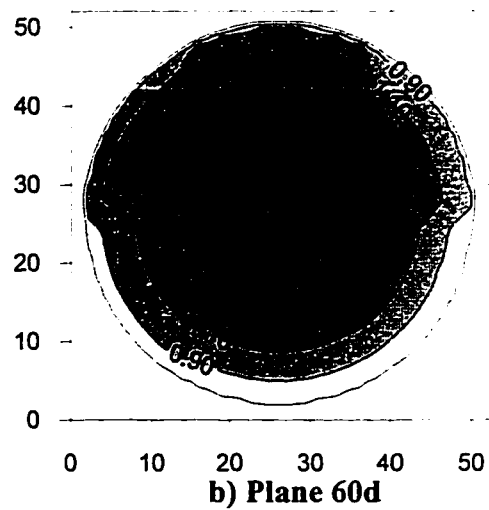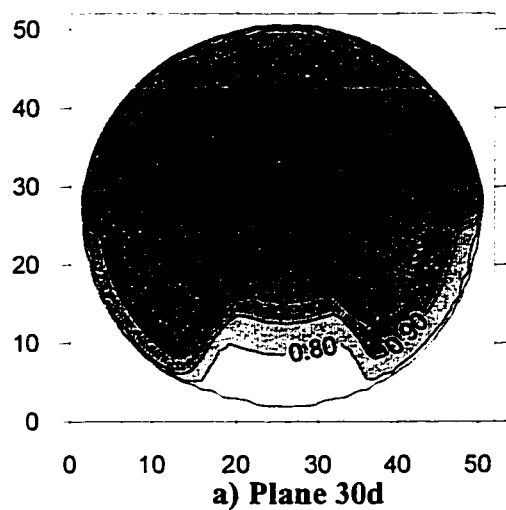
Figure 6-2. Contour maps of gas mass flux distribution (R = 14) for: (a, b) cross-flow, (c, d) co-flow, (e, f) counterflow injection.
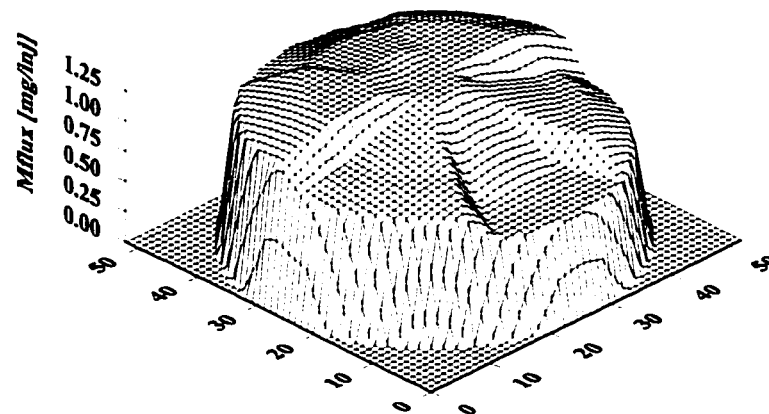
a)
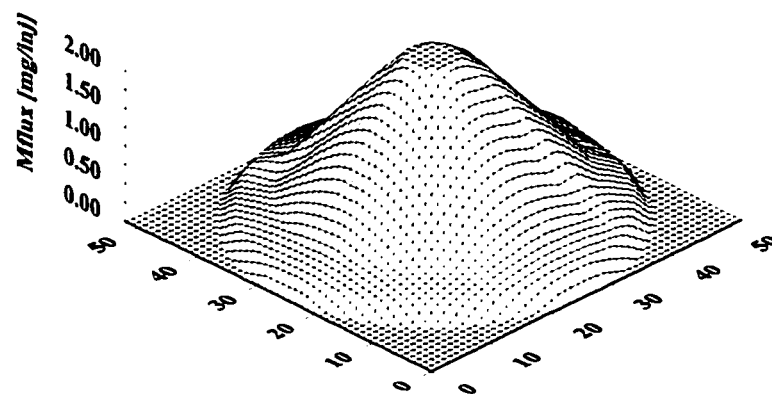
b)
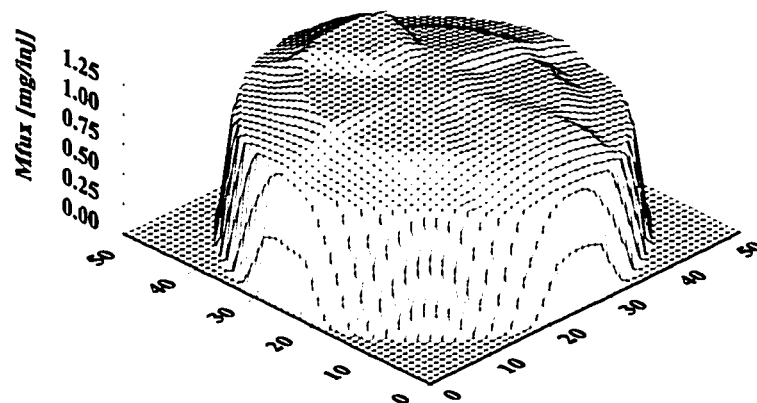
c)

Figure 6-3. Surface maps of gas mass flux distribution in Plane 30d (R = 14) for: a) cross-flow, b) co-flow, c) counterflow mode.
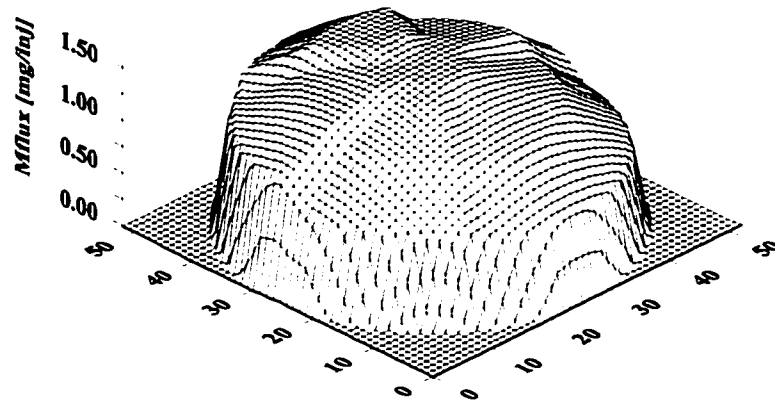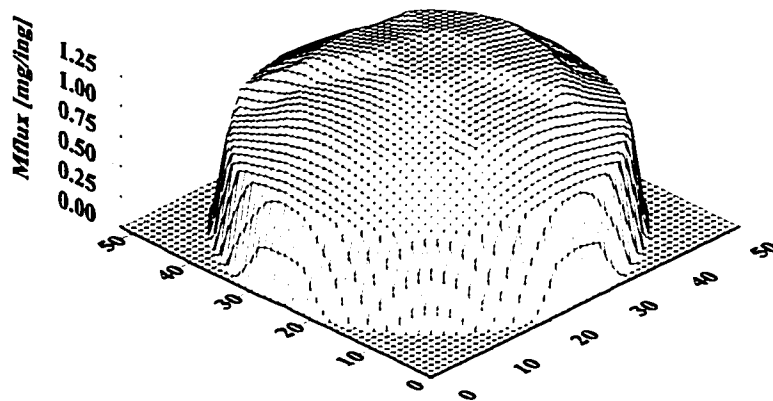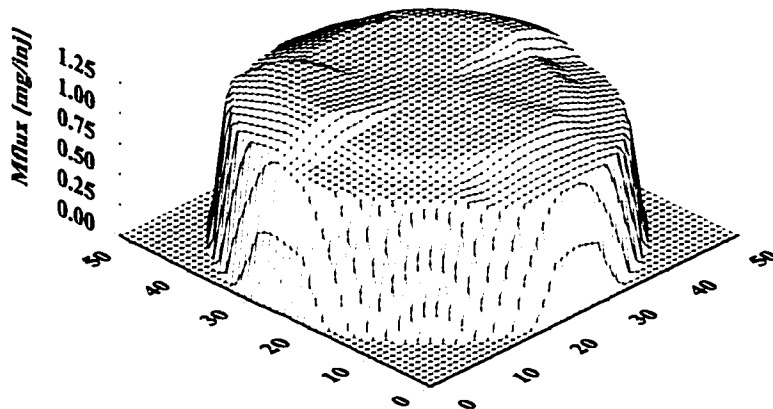
Figure 6-4. Surface maps of gas mass flux distribution in Plane 60d

(R = 14) for: a) cross-flow, b) co-flow, c) counterflow mode.

Table 6-1. Gas mass flux distribution [% of total mass flux] in accordance with values of combustible limits for co-flow injection.

	% Mass Flux Lean mixture (< 5%)		% Mass Flux Flammable mixture (5% - 15%)		% Mass Flux Rich mixture (> 15%)	
Probe position	Plane 30d	Plane 60d	Plane 30d	Plane 60d	Plane 30d	Plane 60d
1	20.59	8.49	79.41	25.79	0.00	66.04
2	11.54	7.38	88.46	25.85	0.00	66.77
3	6.18	6.98	21.09	24.42	72.73	68.60
4	3.97	6.42	9.07	21.66	86.96	71.93
5	3.32	6.12	9.00	22.61	87.84	71.28
6	4.60	7.49	14.85	25.65	80.54	66.86
7	12.76	7.40	60.20	30.23	27.04	62.70
8	22.73	8.74	77.27	32.87	0.00	58.74
9	48.65	9.85	51.35	37.23	0.00	52.92
10	33.67	7.76	67.35	27.33	0.00	64.91
11	15.24	7.42	85.37	22.85	0.00	69.73
12	9.96	7.51	31.95	22.54	58.09	69.94
13	4.55	6.70	12.87	23.86	82.57	69.44
14	4.07	6.16	9.98	21.29	85.95	72.55
15	9.43	6.42	37.26	23.85	53.30	69.42
16	16.18	6.71	83.82	25.24	0.00	67.73
17	30.43	7.85	68.48	30.38	0.00	61.77
18	41.77	8.15	58.23	38.15	0.00	53.70
19	18.97	7.32	80.17	30.66	0.00	62.37
20	9.95	7.64	42.79	28.24	46.77	64.12
21	4.53	6.88	11.64	24.36	83.84	68.77
22	4.15	5.74	11.01	22.19	84.66	72.06
23	7.62	6.69	19.87	23.12	72.52	70.19
24	11.11	6.92	41.55	21.90	47.34	70.89
25	16.67	7.58	83.33	26.67	0.00	65.45

Table 6-2. Summary of statistical analysis on gas mass flux distribution [% of total mass flux] for co-flow injection.

Parameters	% Mass Flux (< 5%)		% Mass Flux (5% - 15%)		% Mass Flux (> 15%)	
Plane position	Plane 30d	Plane 60d	Plane 30d	Plane 60d	Plane 30d	Plane 60d
Average value	14.91	7.29	46.28	26.35	38.81	66.36
Standard Deviation	12.27	0.91	29.50	4.62	37.88	5.30
Minimum value	3.32	5.74	9.00	21.29	0.00	52.92
Maximum value	48.65	9.85	88.46	38.15	87.84	72.55

Table 6-3. Gas mass flux distribution [% of total mass flux] in accordance with values of combustible limits for counterflow injection.

Probe position	% Mass Flux Lean mixture (< 5%)		% Mass Flux Flammable mixture (5% - 15%)		% Mass Flux Rich mixture (> 15%)	
	Plane 30d	Plane 60d	Plane 30d	Plane 60d	Plane 30d	Plane 60d
1	8.13	9.94	32.53	39.77	59.34	50.29
2	8.05	8.83	36.58	37.85	55.03	53.63
3	6.94	8.86	35.96	39.24	57.10	51.58
4	6.41	7.29	31.20	33.74	62.39	58.97
5	6.17	7.60	26.27	31.29	67.83	61.11
6	6.78	9.71	25.75	31.14	67.48	59.14
7	6.50	9.04	23.31	32.04	70.46	58.91
8	7.84	8.44	26.61	32.75	65.55	58.81
9	7.33	7.75	25.92	31.96	66.75	60.29
10	7.20	8.24	25.96	30.59	66.58	61.17
11	7.29	8.97	25.26	30.98	67.45	60.05
12	7.34	8.54	21.52	31.13	71.14	60.61
13	7.09	8.36	22.03	31.99	71.14	59.65
14	6.53	7.76	26.42	34.03	67.05	58.51
15	7.32	8.62	30.49	35.08	62.50	56.31
16	8.98	9.23	33.75	34.46	57.59	56.31
17	8.56	9.14	33.03	38.05	58.41	52.80
18	8.40	8.33	30.25	35.68	61.34	56.25
19	7.46	9.12	26.87	32.35	65.37	58.53
20	7.54	9.15	25.51	33.23	66.67	57.62
21	6.34	8.01	25.90	30.27	67.77	61.42
22	6.47	8.96	25.07	31.21	68.19	59.54
23	7.62	9.22	31.38	35.75	60.70	54.75
24	8.11	9.52	28.53	34.13	63.36	56.35
25	7.95	8.59	29.86	34.90	61.92	56.51

Table 6-4. Summary of statistical analysis on gas mass flux distribution [% of total mass flux] for counterflow injection.

Parameters	% Mass Flux (< 5%)		% Mass Flux (5% - 15%)		% Mass Flux (> 15%)	
Plane position	Plane 30d	Plane 60d	Plane 30d	Plane 60d	Plane 30d	Plane 60d
Average value	7.37	8.69	28.24	33.74	64.36	57.56
Standard Deviation	0.75	0.67	4.08	2.75	4.54	3.05
Minimum value	6.17	7.29	21.52	30.27	55.03	50.29
Maximum value	8.98	9.94	36.58	39.77	71.14	61.42

Table 6-5. Comparison of gas mass flux data [mg/inj] for different injection modes.

Probe position	Plane 30d			Plane 60d		
	Cross-flow	Opposite	Parallel	Cross-flow	Opposite	Parallel
1	0.808	0.916	0.281	0.745	0.927	0.862
2	0.986	0.979	0.598	1.007	1.027	1.053
3	1.006	1.123	0.974	1.205	1.140	1.241
4	1.172	1.200	1.851	1.389	1.187	1.349
5	1.297	1.294	2.196	1.505	1.229	1.351
6	1.365	1.288	1.669	1.505	1.260	1.249
7	1.344	1.288	0.684	1.352	1.348	1.083
8	1.266	1.159	0.357	1.211	1.308	0.928
9	1.143	1.057	0.205	1.028	1.151	0.763
10	1.042	1.084	0.273	1.138	1.026	0.879
11	1.165	1.219	0.521	1.350	1.177	1.078
12	1.270	1.367	0.834	1.498	1.265	1.205
13	1.341	1.379	1.763	1.563	1.247	1.340
14	1.111	1.234	1.721	1.383	1.213	1.293
15	0.814	1.167	0.754	1.184	1.177	1.184
16	0.786	1.103	0.465	0.993	1.058	1.019
17	0.769	0.908	0.255	0.756	0.963	0.832
18	0.976	0.985	0.218	0.825	1.059	0.745
19	1.043	1.096	0.379	1.036	1.104	0.932
20	1.077	1.214	0.708	1.221	1.171	1.075
21	1.224	1.270	1.623	1.439	1.216	1.259
22	1.301	1.287	1.922	1.480	1.243	1.376
23	1.285	1.190	1.054	1.356	1.271	1.274
24	1.222	1.094	0.680	1.148	1.215	1.115
25	1.102	1.013	0.366	0.958	1.048	0.901

Table 6-6. Summary of statistical analysis on gas mass flux data [mg/inj] for different injection modes.
Actual mass injected is 29.9 mg/injection.

Plane position	Plane 30d			Plane 60d		
Parameters	Cross-flow	Opposite	Parallel	Cross-flow	Opposite	Parallel
Total mass flux	27.916	28.914	22.351	30.273	29.028	27.386
Error value	-6.7%	-3.3%	-25.3%	1.2%	-2.9%	-8.4%
Average value	1.117	1.157	0.894	1.211	1.161	1.095
Standard Deviation	0.184	0.133	0.638	0.244	0.109	0.197
Min. value	0.769	0.908	0.205	0.745	0.927	0.745
Max. value	1.365	1.379	2.196	1.563	1.348	1.376

Table 6-7. Comparison of gas pulse duration [ms/inj] for different injection modes.

Probe position	Plane 30d			Plane 60d		
	Cross-flow	Opposite	Parallel	Cross-flow	Opposite	Parallel
1	34.06	38.6	23.95	38	43.2	36.71
2	32.36	36.36	28.38	35.03	39.56	35.61
3	32.06	36.6	30.64	34.65	39.27	35.87
4	33.87	37.15	36.34	35.82	39.59	36.61
5	35.25	39.86	38.6	36.69	40.76	36.87
6	36.04	38.5	36.54	37.34	41.83	36.55
7	35.32	37.91	30.75	38.36	44.47	35.86
8	35.19	38.16	26.69	39.67	45.03	35.23
9	36.32	40.44	24.9	41.7	45.29	35.13
10	41.96	41.34	26.25	44.33	43.05	36.31
11	40.35	40.73	28.98	42.72	42.82	36.38
12	36.79	42.4	31.56	40.41	42.53	36.3
13	36.2	43.11	37.03	38.18	41.65	36.94
14	33.64	38.7	35.59	35.44	39.19	35.63
15	30.82	37.67	28.17	33.56	39.31	34.3
16	30.47	38.68	25.1	33.37	39.58	33.85
17	33.41	38.86	24.43	36.42	42.11	34.21
18	34.55	40.11	23.08	37.79	43.8	34.3
19	32.82	38.39	24.86	35.14	40.81	33.89
20	32.54	37.74	28.33	34.4	39.71	34.2
21	34.27	38.39	35.11	36.13	39.4	35.65
22	35.03	39.45	37.17	37.28	41.61	36.75
23	34.1	38.39	32.64	37.63	43.61	36.3
24	34.04	38.61	29.69	38.89	44.73	36.07
25	35.3	41.03	26.86	40.82	44.99	36.13

Table 6-8. Summary of statistical analysis on gas pulse duration [ms/inj] for different injection modes.

Plane position	Plane 30d			Plane 60d		
Parameters	Cross-flow	Opposite	Parallel	Cross-flow	Opposite	Parallel
Average value	34.67	39.09	30.07	37.59	41.92	35.67
Standard Deviation	2.55	1.69	4.84	2.83	2.11	1.00
Min. value	30.47	36.36	23.08	33.37	39.19	33.85
Max. value	41.96	43.11	38.60	44.33	45.29	36.94

6.4. Summary

The statistical analyses on mass flux distribution according to combustible limits, and continuity analysis for each nozzle configuration, have enabled us to make the following observations. Among tested nozzle geometries, the counterflow injection method has shown the smallest standard deviation in values of mass flux for Plane 30d, as well as for Plane 60d. This fact indicates that achieved mixing is much closer to completion in the case of counterflow injection than in the co-flow or cross-flow injection modes. The percentage of mass flux values, in accordance with combustible limit Mflux (>15%), for co-flow injection is definitely higher than in the others modes.

The final conclusion is that results from comparison of mass flux data for different modes of gas injection have shown that counterflow injection is the most advantageous to obtain evenly mixed combustible mixture. The biggest unevenness in mass flux distribution was observed in co-flow injection mode.

7. Conclusions and Recommendations

The major objectives of this study were to understand and predict the outcome of mixing process in the air-intake manifold of dual-fuel diesel engine.

The results from the literature survey have shown that mixing phenomena of pulsed turbulent variable density jets in a cross-flow, confined environment have not been studied fully. Several assumptions made from theoretical and empirical investigations of relevant problems were employed in the current research.

The focus of this study was shifted toward the development of a reliable measurement system to characterize parameters of gas-air mixture for engine applications.

The experimental setup was developed to model and study mixture formation in the diesel engine air-intake manifold. The FFID technique, used in the model to measure concentration fields of methane, provides a wealth of quantitative information about the mixing process of jets.

Based on conclusions from the work of Richards and Pitts (46), and results of measurements of mean velocity profiles, it was assumed that velocity and density parameters of the jet far from injection point depend only on the rate of momentum addition. Therefore, the centerline decay rate and spreading rate of the gas jet are independent of initial density ratio and velocity profile.

The adequate results of continuity analysis for steady jet flow experiments confirmed the validity of assuming a uniform velocity profile and of using the bulk density values for gas-air mixture.

Steady-state experiments have proved the ability of the measurement system to accurately measure the jet mixing and mass flux distribution in the manifold.

Mass flux distribution with pulsed (15 Hz) jet flow was studied to model the real situation of the gas injection into the diesel engine air-intake manifold.

The method of calculating area under time-response curves of the FFID output signal has been proven useful for analysis of mixture formation in pulsed gas flow environment.

The density and velocity fluctuations due to pulsating gas flow and the entrainment process were thought to be responsible for small discrepancies in calculated values of mass flow rate for injected gas in pulsed gas injection experiments.

A uniform gas-air velocity profile was assumed in continuity analysis for two experimental planes in the far-field region in the steady injection and pulsed injection tests. It worked very well.

An example of using the newly developed measurement system to study jet mixing was shown by investigating the effect of different injector nozzle geometries. The results showed that pulsed counter-flow injection enhanced the mixing process compared with pulsed co-flow or cross-flow injection. (However, whether this enhancement is good for the diesel engine can only be confirmed by testing this method of injection on the engine.)

On the basis of the current findings, it is concluded that the newly developed measurement system can be employed in actual diesel engine manifold studies with slight modification. The LDV technique can be used for fast velocity measurements.

References

1. **Johnston, S. C., and Green, R. M.,** "Engine hydrocarbon concentration measurements: a comparison between sampling probe and Raman spectroscopy," SAE Paper No. 20439, 1982.

2. **Ekchian, A., Heywood, J. B., and Rife, J. M.,** "Time resolved measurements of the exhaust from a jet ignition prechamber stratified charge engine," SAE Paper No. 770043, SAE Transitions, Vol. 86, 1977.

3. **Tabaczynski, R. J., Heywood, J. B., and Keck, S. C.,** "Time resolved measurements of hydrocarbon mass flow rate in the exhaust of spark ignition engine," SAE Paper No. 720112, SAE Transitions, Vol. 81, 1972.

4. **Weaver, C. S.,** "Natural gas vehicles - a review of the state of the art," SAE Paper No. 892133, 1989.

5. **Klimstra, J.,** "Carburetors for gaseous fuels - on air-to-fuel ratio, homogeneity and flow restriction," SAE Paper No. 892141, 1989.

6. **Karim, G. A.,** "An examination of some measures for improving the performance of gas fueled diesel engines at light load," SAE Paper No. 912366, 1991.

7. **Abramovich, G. N.,** "The theory of turbulent jets," MIT Press, Cambridge, Mass., 1963.

8. **Brodkey, R. S.,** "Fluid motion and mixing," Mixing, Theory and Practice, Academic Press, New York, 1966.

9. **Rajaratnam, M.,** "Turbulent jets," Vol. 5, Developments in Water Science, Elsevier Science Publishing Co., Amsterdam, 1976.

10. **Bradshaw, P.,** "Review - Complex turbulent flows," Journal of Fluids Engineering, June 1975.

11. **Pai, S.I.,** "Fluid dynamics of jets," D. Van Nostrand, New York, 1954.

12. **Callaghan, E. E., Ruggeri, R.S., and Bowden, D. T.,** "Penetration of air jets issuing from circular, square and elliptical orifices directly perpendicularly to an air stream," NACA TN 2019, Feb. 1950.

13. **Keffer, J. F. and Baines, W. D.,** "The round turbulent jet in a cross-wind," Journal of Fluid Mechanics, Vol. 15, Pt. 4, 1963, pp. 481- 496.

14. **Platten, J. L. and Keffer, J. F.,** "Deflected turbulent jet flows," Journal of Applied Mechanics, 1971, pp. 756 - 758.

15. **Thompson, A. M.,** "The flow induced by jets exhausting normally from a plane into an air stream," Ph. D. thesis, Univ. of London, 1971.

16. **Kamotani, Y. and Greber, I.,** "Experiments on a turbulent jet in a cross flow," AIAA Journal, Vol. 10, 1972, pp. 1425 - 1429.

17. **Chassaing, P., George, J., Glaria, A., and Sananes, F.,** "Physical characteristics of subsonic jets in a cross-stream," Journal of Fluid Mechanics, Vol. 12, 1974, p. 41.

18. **Fearn, R., and Weston, R. P.,** "Vorticity associated with a jet in a crossflow," AIAA Journal, Vol. 12, 1974, pp. 1666 - 1671.

19. **Moussa, Z. M., Trischka, J. W., and Eskinazi, S.,** "The near field in the mixing of a round jet with a cross-stream," Journal of Fluid Mechanics, Vol. 80, 1977.

20. **Campbell, J. F. and Schetz, J. A.,** "Flow properties of submerged heated effluents in a waterway," AIAA Journal, Vol. 11, No. 2, 1973.

21. **Fric, T. F. and Roshko, A.,** "Vortical structure in the wake of a transverse jet," Journal of Fluid Mechanics, Vol. 279, 1994, pp. 1 - 47.

22. **Birch, A. D., Brown, D. R., Dodson, M. G., and Swaffield, F.,** "The structure and concentration decay of high pressure jets of natural gas," Combustion Science and Technology, Vol. 36, 1984, pp. 249 - 261.

23. **Crabb, D., Durao, D. F. G., and Whitelaw, J. H.,** "A round jet normal to a crossflow," Transactions of the ASME, Vol. 103, 1981, pp. 142 - 152.

24. **Pratte, B. D. and Baines, W. D.**, "Profiles of the round turbulent jet in a cross flow," Journal of the Hydraulics Division, Proceedings of the ASCE, Vol. 92, No HY6, 1967.

25. **Krausche, D., Fearn, R. L., and Weston, R. P.**, "Round jet in a cross flow: influence of injection angle on vortex properties," AIAA Journal, Vol. 16, No. 6, 1978.

26. **Smy, J. R. and Ransom, E. C. P.**, "The structure of single jets at large angle to a cross- flow," HSA-KAD-R-GEN-2288, June 1976.

27. **Wooler, P. T.**, Flow of a circular jet into a cross flow," Journal of Aircraft, May-June 1969, pp. 283 - 284.

28. **Margason, Ri. J.**, "The path of a jet directed at large angles to a subsonic free stream," NASA TN D-4919, 1968.

29. **Patrick, M. A.**, "Experimental investigations of the mixing and penetration of a round turbulent jet injected perpendicularly into a transverse stream," Transaction of Institute of Chemical Engineers, Vol. 45, 1967.

30. **Storms, K. R.**, "Low-speed wind tunnel investigation of a jet directed normal to the wind," Rep. 885, Aeronaut. Lab., Univ. of Washington, Nov. 1965.

31. **Fearn, R. L. and Weston, R. P.**, "Induced velocity field of a jet in a crossflow," NASA TP-1087, May 1978.

32. **Ivanov, Y. V.**, "Shape of the centerline of an axisymmetric fan type jet in a cross flow," Izv. VUZ Aviotsionnaya Teknika, No. 4, Apr. 1963.

33. **Shandorov, G. S.**, "Calculation of a jet axis in a drifting flow," Soviet Aeronautics, Vol. 9, No. 2, 1959.

34. **Snel, H.**, "A model for the calculation of the properties of a jet in a crossflow," NLR TR 74080 U, June 1974.

35. **Jordison, R.**, "Flow in a jet directed normal to the wind," R. & M., No. 3074, British A. R. C., Oct. 1956.

36. **Schetz, J. A. and Billig, F. S.**, "Penetration of gaseous jets injected into a supersonic stream," Journal of Spacecraft and Rockets, Vol. 11, pt. 1, Aug. 1961.

37. **Ricou, F. P. and Spaulding, D. B.**, "Measurements of entrainment by axisymmetrical turbulent jets," Journal of Fluid Mechanics, Vol. 11, 1961, pp. 21 - 32.

38. **Adler, D. and Baron, A.,"** Prediction of a three-dimensional circular turbulent jet in crossflow," AIAA Journal, Vol. 17, No. 2, Feb. 1979.

39. **Chang, H.-C.**, " The roll-up of a cylindrical jet in across flow," USAF- ARL-73-0131, Sept. 1973.

40. **Holdeman, J. D., Walker, R. E.**, "Mixing of a row of jets with a confined cross-flow," AIAA Journal, Vol. 15, 1977.

41. **Tatchell, D. G.**, "Convection processes in confined, three-dimensional boundary layers," Ph. D. Thesis, Univ. of London, 1975.

42. **Catalano, G. D., Chang, K. S., and Mathis, J. A.**, "Investigation of turbulent jet impingement in a confined crossflow," AIAA Journal, Vol. 27, No. 11, Nov. 1989, pp. 1530 - 1535.

43. **Jones, W. P. and McGuirk, J. J.**, "Computation of a round turbulent jet discharging into a confined cross-flow," in: Turbulent Shear Flows 2, Springer, 1980, pp. 233 - 245.

44. **Ince, N. Z., Leschziner, M. A.**, "Caclulation of single and multiple jets in cross-flow with and without impingement using Reynolds-stress-trnsport closure," AGARD Conference Proceedings 534, Reference 23, 1993.

45. **Dowling, D. R., and Dimotakis, P. E.**, "Similarity of the concentration field of gas-phase turbulent jets," Journal of Fluid Mechanics, Vol. 218, 1990.

46. **Richards, C. D. and Pitts, W. M.**, "Global density effects on the self-preservation behaviour of turbulent free jets," Journal of Fluid Mechanics, Vol. 254, 1993.

47. **Wilson, R. A. M., and Danckwerts, P. V.**, "Studies in turbulent mixing - 11 a hot jet. Chem. Engineering Science, Vol. 19, pp. 885 - 895.

48. **Becker, H. A., Hottel, H. C., and Williams, G. C.,** "The nozzle-fluid concentration field of the round, turbulent, free jet," Journal of Fluid Mechanics, Vol. 30, 1967.

49. **Wygnanski, I. and Fiedler, H.,** "Some measurements in the self-preserving jet," Journal of Fluid Mechanics, Vol. 72, 1975.

50. **Broadwell, J. E. and Breindethal, R. E.,** "Structure and mixing of a transverse jet in incompressible flow," Journal of Fluid Mechanics, Vol. 148, 1984, pp. 405 - 412.

51. **Breidenthal, R. E., Buonadonna, V. R., and Weisbach, M. F.,** "Molecular mixing via jet in confined volumes," Journal of Fluid Mechanics, Vol. 219, 1990, pp. 531 - 544.

52. **Crow, S. C. and Champagne, F. H.,** "Orderly structures in jet turbulence," Journal of Fluid Mechanics, Vol. 48, Part 3, 1971.

53. **Binder, G. and Favre-Marinet, M.,** "Mixing improvement in pulsating turbulent jets," ASME Symposium on Fluid Mechanics of Mixing, June 1973.

54. **Curtet, R. M. and Girard, J. P.,** "Visualization of a pulsating jet," ASME Symposium on Fluid Mechanics of Mixing, June 1973.

55. **Bremhorst, K. and Harch, W. H.,** "Near-field velocity measurements in a fully pulsed subsonic air jet," Turbulent Shear Flows - 1, Springer-Verlag, 1979.

56. **Wu, J. M., Vakili, A. D., and Yu, F. M.,** "Investigation of the interacting flow of nonsymmetric jets in crossflow," AIAA Journal, Vol. 26, No. 8, 1988.

57. **Collings, N. and Eade, D.,** "An improved technique for measuring cyclic variations in the hydrocarbon concentration in an engine exhaust," SAE Paper No. 880316, 1988.

58. **Henein, A. N., Tagomori, M. K., Yassine, M. K., Henein, A. H., Hartman, P., Asmus, T.,** "In-situ phase-shift measurement of the time-resolved UBHC emissions," SAE Paper No. 950161, 1995.

59. **Summers, T. and Collings, N.,** "Modelling the transit time of a Fast Response Flame Ionisation Detector during in-cylinder sampling," SAE Paper No. 950160, 1995.

60. **Summers, T. and Collings, N.,** "Signal reconstruction applied to a Fast Response Flame Ionisation Detector," SAE Paper No. 952541, 1995.

61. *Cambustion Ltd.,* "The HFR 400 High Frequency FID User Manual," Cambridge, England, 1994.

62. **Colin, P. E., and Olivari, D.,** "The impingement of a circular jet normal to a flat surface with and without a cross flow," von Karman Institute Final Technical Report, DTIC TR AD688953, January 1969.

63. **Stewart, V. R., Blake, W. B.,** "A study of the effect of a moving ground belt on the vortex created by a jet impinging on the ground in a crossflow," AIAA Paper 92-4250, August 1992.

64. **Norimasa Iida, Kou Hirawo, G. Takeshi Sato,** "Experimental study of transient jet impinging on a wall," SAE Paper No. 900479, 1990.

65. **Tanabe, H., Ohnishi, M., Fujimoto, H., and Sato, G., T.,** "Experimental study of the transient hydrogen jet using a fast response probe," Int. Journal Hydrogen Energy, vol. 7, No. 12, 1982.
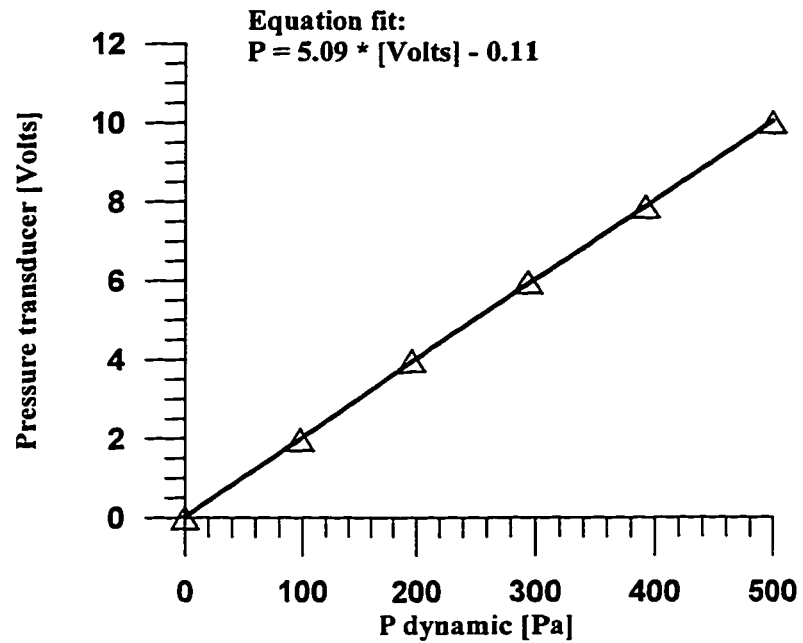
Appendix A. Pressure Transducers Calibration

Equation fit:
$P = 5.09 * [Volts] - 0.11$

Figure A-1. Calibration curve for Pitot tube pressure transducer.
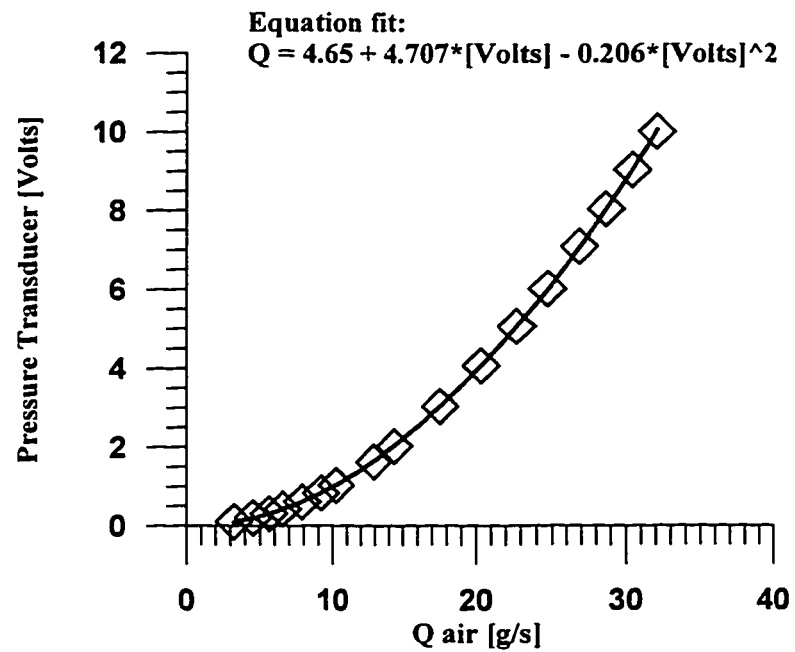
Equation fit:
$Q = 4.65 + 4.707*[Volts] - 0.206*[Volts]^2$

Figure A-2. Calibration curve for Orifice Meter.

Appendix B. Calibration of FFID HFR 400 with a "Long" probe

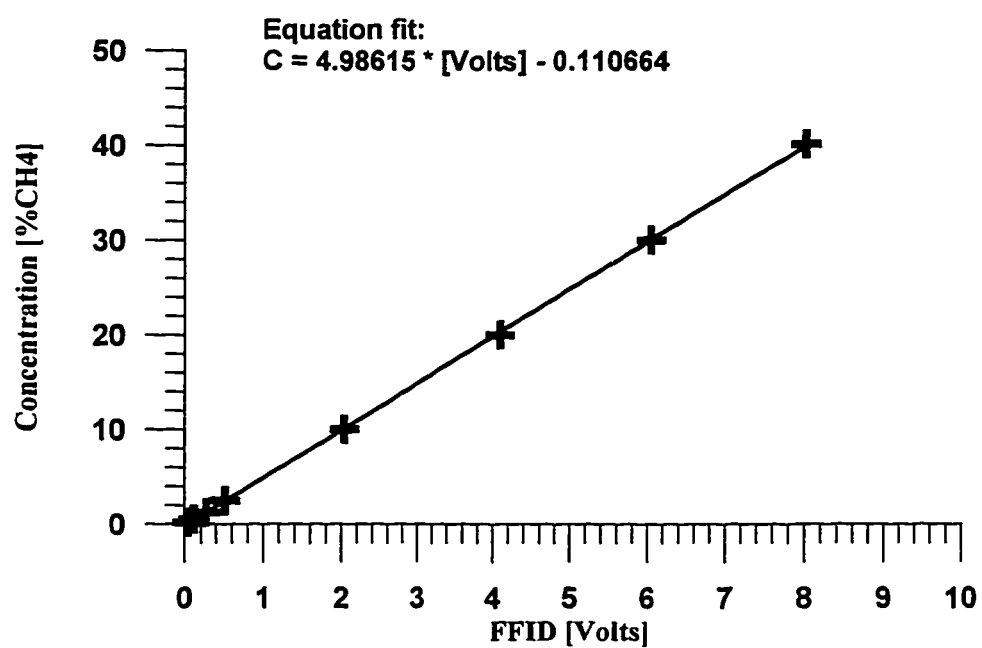**Equation fit:**
$$C = 4.98615 * [Volts] - 0.110664$$

Figure B-1. Calibration curve for FFID voltage with methane.

Appendix C. Software Used in Experiments

FFID output signal was recorded on one channel of a four-channel FM recorder (RACAL) using bandwidth of 1 kHz. The recorded data files were than digitized with the data acquisition system (Metrobyte DAS 16G) in a laboratory PC workstation. The processing and analyzing of digitized data used software written in a QuickBASIC. The STEADY8.BAS software for steady gas injection and PULSE8.BAS software for pulsed gas injection were used during the tests to monitor the calibrated output signal on computer display. The source data files for both types of experiments created using ZDATAREC.BAS program.

The source data files from steady gas injection experiments were analyzed with ZSTATIST.BAS program. The output files from this program contained time averaged values of concentration together with its statistic information during 20 ms sampling period. These files were used than in SURFER6 plotting software to create visual contour maps of mass flux distribution in cross-sectional planes of the test duct.

The source data files from pulsed gas injection experiments were analyzed with a set of programs. The description list of these programs is following:

AVEPULSE.BAS   produce ensemble-averaged values of concentration and create the calibrated average injection pulse of FFID output signal for one probe position.

AREASTAT.BAS   originate statistic information on gas mass flux redistribution for one probe position.

AVEAREA.BAS   combine the information from AVEPULSE.BAS and AREASTAT.BAS into one table for 25 positions of probe.

AVEPEAKC.BAS   produce ensemble-averaged value of peak concentration in average injection pulse for 25 probe positions.

The information created with the help of listed above programs was used in SURFER6 plotting software to develop the contour and 3-D maps of mass flux redistribution of injected gas in test duct.